UNIVERSIDADE FEDERAL DE SÃO CARLOS
CENTRO DE CIÊNCIAS EXATAS E DE TECNOLOGIA
DEPARTAMENTO DE QUÍMICA
PROGRAMA DE PÓS-GRADUAÇÃO EM QUÍMICA

HETEROSTRUCTURE FORMATION OF $BiVO_4$ WITH DIFFERENT Bi COMPOUNDS: ROLE OF THE HETEROJUNCTION ON PHOTOCATALYTIC PROPERTIES

Osmando Ferreira Lopes*

Thesis presented as part of the requirements to obtain the title of DOCTOR IN SCIENCES, concentration area: PHYSICAL-CHEMISTRY.

Advisor: Caue Ribeiro de Oliveira

***scholarship: FAPESP**

São Carlos - SP
2016

Ficha catalográfica elaborada pelo DePT da Biblioteca Comunitária UFSCar
Processamento Técnico
com os dados fornecidos pelo(a) autor(a)

Lopes, Osmando Ferreira
L864h Heterostructure formation of BiVO4 with different Bi compounds : role of the heterojunction on photocatalytic properties / Osmando Ferreira Lopes. -- São Carlos : UFSCar, 2017.
115 p.

Tese (Doutorado) -- Universidade Federal de São Carlos, 2016.

1. Fotocatálise heterogênea. 2. Vanadato de Bismuto. 3. Heteroestrutura. 4. Tratamento de água. 5. Radiação visível. I. Título.

UNIVERSIDADE FEDERAL DE SÃO CARLOS

Centro de Ciências Exatas e de Tecnologia
Programa de Pós-Graduação em Química

Folha de Aprovação

Assinaturas dos membros da comissão examinadora que avaliou e aprovou a Defesa de Tese de Doutorado do candidato Osmando Ferreira Lopes, realizada em 29/08/2016:

Prof. Dr. Cauê Ribeiro de Oliveira
Embrapa

Raquel F. Pupo Nogueira

Profa. Dra. Raquel Fernandes Pupo Nogueira
UNESP

Profa. Dra. Marcia Tsuyama Escote
UFABC

Prof. Dr. Jean Marcel Ribeiro Gallo
UFSCar

Prof. Dr. Elton Fabiano Sitta
UFSCar

Quando considero a duração mínima da minha vida, absorvida pela eternidade precedente e seguinte, o espaço diminuto que ocupo, e mesmo o que vejo, abismado na infinita imensidade dos espaços que ignoro e me ignoram, assusto-me e assombro-me de me ver aqui e não lá. Quem me pôs aqui? Por ordem de quem me foram destinados este lugar e este espaço?

Blaise Pascal

Dedico este trabalho a minha família, em especial aos meus pais, pelo apoio, amor e confiança.

Agradecimentos

A Deus pela sua infinita bondade e misericórdia.

Ao Dr. Caue Ribeiro, pela orientação, confiança e especialmente pela amizade.

Aos doutores Waldir Avansi Jr, Kele Carvalho, Luís Fernando da Silva, Henrique Mourão e Vagner Mendonça pelo suporte, parceria frutífera e amizade.

À Dra. Elaine Paris, e aos Professores Renato Lajarim, Manoel Homem e Emerson Camargo pelas contribuições e conselhos durante o meu doutorado (Exame de Qualificação e Seminário). Aos professores Elton Sitta, Jean Gallo, Raquel Nogueira e Márcia Escote pelas contribuições e questionamentos durante a minha Defesa.

À Embrapa Instrumentação pela excelente estrutura fornecida para realização deste trabalho. Um agradecimento especial ao pessoal de suporte à pesquisa, Viviane, Adriana, Silviane, Mattêo, Paulinho, Joana, Edilson Gabriel e Suzane.

Ao Programa de Pós-Graduação em Química da Universidade Federal de São Carlos (PPGQ-UFSCar), pela oportunidade que me foi dada para realizar o doutorado.

À FAPESP (Projeto N° 13/13888-0) pela bolsa concedida, pela excelência em todos os quesitos, e por todas as oportunidades que foram possíveis graças ao suporte financeiro.

Ao Laboratório de Caracterização Estrutural LCE/DEMa pelas análises de HRTEM. Ao Laboratório Interdisciplinar de Eletroquímica e Cerâmica LIEC/UFSCar em especial ao meu amigo Pablo S. Lemos, pelo auxílio em diversas análises. Ao Laboratório Nacional de Nanotecnologia (LNNano/LNLS) pela realização das medidas de XPS (Projeto N° XPS-18304).

À Dra. Débora Milori (Lab. Ótica e Fotônica, Embrapa Instrumentação) por disponibilizar a infraestrutura para medidas de fotoluminescência resolvida no tempo.

A todos do meu grupo de pesquisa, em especial ao Fernando, Amanda, Gelson, André, Elaine, Gabriela e Jéssica por tornar o ambiente de trabalho sempre agradável e produtível, acima de tudo pelo companheirismo e amizade. Um agradecimento especial ao Gabriel Kossaka, bolsista de IC, que me auxiliou na realização de diversos experimentos durante 2 anos do meu doutorado.

Ao meu grande amigo Diego Guedes e toda sua família pela companhia, conselhos, cobranças e discussões durante toda minha vida acadêmica que me fizeram crescer.

Aos meus pais, Orlando e Terezinha que sempre me serviram de exemplo e me mostraram a importância do trabalho duro; meus irmãos Osvando e Olândia; meus cunhados Daniela e Murilo; minhas sobrinhas Eduarda e Estela; e a minha vozinha Anatália, pelo amor, apoio e incentivo. Sem vocês nada disso seria possível.

A todos os outros amigos e familiares que me apoiaram durante toda esta caminhada.

Tables List

Figures List

Resumo

OBTENÇÃO DE HETEROESTRUTURAS DE $BiVO_4$ COM DIFERENTES COMPOSTOS DE Bi: PAPEL DAS HETEROJUNÇÕES NAS PROPRIEDADES FOTOCATALÍTICAS. Semicondutores que podem ser ativados sob radiação visível são de grande interesse para processos fotocatalíticos. O $BiVO_4$ é um semicondutor com valor de *band-gap* de 2,4 eV, no entanto, este apresenta uma baixa atividade fotocatalítica, devido principalmente à rápida recombinação do par elétron/buraco. Uma estratégia eficiente para superar este desafio é pela formação de heteroestruturas do tipo-II. Diante deste panorama, este trabalho teve por objetivo: (i) desenvolver métodos para obter heteroestruturas de $BiVO_4$ com diferentes compostos de bismuto (*t*-$BiVO_4$, Bi_2O_3 e $Bi_2O_2CO_3$), (ii) avaliar o efeito das heterojunções nas propriedades fotocatalíticas, e (iii) estudar os mecanismos de transferência de carga e de degradação de poluentes orgânicos. Inicialmente, este trabalho lidou com a síntese do $BiVO_4$ pelo método de oxidação por peróxido e observou-se que a principal razão para baixa atividade fotocatalítica do $BiVO_4$ é sua incapacidade de reduzir o O_2 em $O_2^{\bullet-}$. Com o objetivo de superar este desafio, buscou-se a obtenção de heterostruturas de $BiVO_4$ nas fases monoclínica e tetragonal (*m*-$BiVO_4$/*t*-$BiVO_4$), pelo método de oxidação por peróxido. Foi verificado que a heteroestrutura *m*-$BiVO_4$/*t*-$BiVO_4$ exibiu uma melhor performance fotocatalítica na degradação do corante azul de metileno (AM) do que as suas fases isoladas, sob radiação visível. As imagens de microscopia eletrônica de transmissão de alta resolução (HRTEM) revelaram que a amostra heteroestruturada é composta de nanopartículas com tamanho médio de 10 nm, a interface *m*-$BiVO_4$/*t*-$BiVO_4$ também foi evidenciada. Foram propostos mecanismos de transferência de cargas entre as fases e de oxidação do poluente orgânico de acordo com os resultado obtidos pelas técnicas de XPS, espectrometria de massas e análise de TOC. Os buracos (h^+), radicais superóxidos ($O_2^{-\bullet}$) e hidroxila ($^{\bullet}OH$) foram as principais espécies ativas responsáveis na fotodegradação do AM. O aumento da fotoatividade da heteroestrutura *m*-$BiVO_4$/*t*-$BiVO_4$ ocorreu devido a formação de uma heterojunção adequada, que promove a separação efetiva das cargas foto-geradas. No entanto, este método apresentou dificuldade no controle morfológico e da composição da heteroestruturas por ser um processo de cristalização simultânea das fases, portanto, foi desenvolvido uma nova estratégia para a produção de heteroestruturas dirigido pela diferença de solubilidade entre dois semicondutores que possuem ao menos um metal em comum. Para tal, a formação de heterojunções pelo crescimento do $BiVO_4$ na superfície

de sacrifício do Bi_2O_3 ou $Bi_2O_2CO_3$ pré-formados foi avaliada. Para a heteroestrutura $Bi_2O_3/BiVO_4$ foi observado que a quantidade de junções formadas foi dependente da solubilidade do precursor que foi variado pelo tamanho de partícula do Bi_2O_3. As heterojunções foram evidenciadas por imagens de HRTEM, onde foi observado a formação de nanopartículas do $BiVO_4$ na superfície das fases de Bi_2O_3 e $Bi_2O_2CO_3$. Os espectros de fotoluminescência e de XPS confirmaram que a formação da heteroestrutura do tipo-II conduziu ao aumento do tempo de vida dos portadores de carga. Esta estratégia de síntese proposta mostrou-se eficiente, já que foi possível obter heteroestruturas de $Bi_2O_3/BiVO_4$ e $Bi_2O_2CO_3/BiVO_4$ com controle de morfologia e composição, que resultou no aumento da fotoatividade quando comparado as fases isoladas.

Palavras-chave: Fotocatálise heterogênea. Vanadato de Bismuto. Heteroestrutura. Tratamento de água. Radiação visível. Mecanismo de fotodegradação.

Abstract

HETEROSTRUCTURE FORMATION OF $BiVO_4$ WITH DIFFERENT Bi COMPOUNDS: ROLE OF THE HETEROJUNCTION ON PHOTOCATALYTIC PROPERTIES. Semiconductors employed as photocatalysts that can be activated by visible irradiation have attracted intense scientific interest due to their applications in heterogeneous photocatalysis. $BiVO_4$ is a semiconductor with band gap value of 2.4 eV; however, this material exhibits poor photocatalytic activity mainly due to the rapid recombination of electron/hole pair. An efficient strategy to overcome this challenge is through the formation of type-II heterostructures. Based on this overview, this work aimed at: (i) developing methods to obtain heterostructures composed of $BiVO_4$ and different bismuth compounds (*t*-$BiVO_4$, Bi_2O_3 e $Bi_2O_2CO_3$), (ii) to evaluate the effect of heterojunction formation on photocatalytic properties, and (iii) to study the mechanisms of charge transfer and organic pollutants degradation. Initially, this work investigated the synthesis of $BiVO_4$ by oxidant peroxide method, and it was observed that the main reason for the poor photoactivity of $BiVO_4$ is its inability to reduce O_2 to $O_2^{\bullet-}$. In order to overcome this challenge, we attempted to obtain heterostructures between monoclinic $BiVO_4$ and tetragonal $BiVO_4$ phases (*m*-$BiVO_4$/*t*-$BiVO_4$) by oxidant peroxide method. It was verified that *m*-$BiVO_4$/*t*-$BiVO_4$ heterostructures exhibited better photocatalytic performance in the degradation of methylene blue (MB) dye than their isolated phases, under visible irradiation. HRTEM images revealed that the heterostructured sample was composed of nanoparticles with average size of 10 nm, the *m*-$BiVO_4$/*t*-$BiVO_4$ interface was also evidenced. The mechanisms of charge transfer between the phases and organic pollutant oxidation were proposed in agreement with the obtained results by XPS, mass spectroscopy and TOC analysis. Holes (h^+), superoxide anion ($O_2^{-\bullet}$) and hydroxyl radicals ($^\bullet OH$) were the primary active species responsible for MB photodegradation. The increase of *m*-$BiVO_4$/*t*-$BiVO_4$ heterostructure photoactivity occurred due to the formation of a suitable heterojunction, promoting the effective separation of photogenerated charges. However, this method presented difficulties in the control of heterostructure morphology and composition, because it is based on a simultaneous two-phase crystallization process. Therefore, we developed a novel strategy for heterostructure tailoring driven by solubility difference of two semiconductors that possess at least one metal in common. For this, the formation of heterojunctions by $BiVO_4$ growth on Bi_2O_3 or $Bi_2O_2CO_3$ self-sacrificial surface was evaluated. For the Bi_2O_3/$BiVO_4$ heterostructures, the amount of

heterojunctions formed between Bi_2O_3 and $BiVO_4$ was tuned by synthesis process variables (temperature and V concentration) and the particle size of preformed Bi_2O_3 (*i.e.* solubility difference). The heterojunctions were evidenced by HRTEM images, where the growth of $BiVO_4$ nanoparticles on Bi_2O_3 or $Bi_2O_2CO_3$ surface was observed. Time resolved photoluminescence and XPS results confirmed that the formation of type-II heterostructure led to increase of charge carriers lifetime. The proposed synthesis strategy showed efficiency in obtaining $Bi_2O_3/BiVO_4$ and $Bi_2O_2CO_3/BiVO_4$ heterostructures with controlled morphology and composition that improved photoactivity when compared to their isolated phases.

Keywords: Heterogeneous Photocatalysis. Bismuth Vanadate. Heterostructure. Water treatment. Visible radiation. Photodegradation mechanism.

Summary

1. - Introduction

1.1 - Background

Environmental and energy issues are among the biggest challenges faced by countries in modern society. The growth of worldwide industry has caused severe environmental contaminations, such as contamination of drinking water by organic pollutants from industrial (e.g. drugs and dyes) and agricultural effluents (e.g. pesticide).[1,2] Therefore, the tailoring of high efficiency eco-friendly methods for environmental remediation has become an urgent task. Among the wide variety of methods recently studied for these purposes, heterogeneous photocatalysis has aroused as one of the most promising methods because it represents an easy way to utilize the energy of natural sunlight.[3] The potential applications of photocatalysis are found mainly in the following fields: (i) photodegradation of organic pollutants (water treatment);[4] (ii) hydrogen generation (water splitting);[5] (iii) CO_2 reduction (artificial photosynthesis).[6] In water treatment, this process is based on the formation of radicals, such as, $^{\bullet}OH$, $HO_2^{\bullet}$ and $^{\bullet}O_2^{-}$, which are highly reactive and they has high oxidizing power, which can promote the degradation of a wide variety of organic pollutants.[4,7]

Titanium dioxide (TiO_2)[8–13] and zinc oxide (ZnO)[14–17] are the main semiconductors applied in heterogeneous photocatalysis process such as organic pollutants degradation and water splitting.[18,19] These materials possess specific characteristics that are regarded as crucial for a good photocatalytic performance under ultraviolet (UV) irradiation when compared with other materials, such as band gap values of ca. 3.2 eV and 3.4 eV, respectively, suitable textural properties, and slow recombination rate of photogenerated electron/hole pair.[17,20] However, these materials can only be activated by UV radiation (wavelength below of 385 nm), which represents less than 5% of all solar energy that reaches the Earth's surface, thereby disabling their application under natural conditions.[2,4,21–24]

In this sense, semiconductors that can be activated by visible radiation have arose much scientific interest. Bismuth vanadate ($BiVO_4$) is a *n*-type semiconductor with band gap value ranging in 2.4 eV – 2.8 eV, depending on its crystalline phase.[25,26] $BiVO_4$ exists in three different crystalline phases: two tetragonal structures (zircon type and scheelite type, *t*-$BiVO_4$), and one monoclinic structure (scheelite type, *m*-$BiVO_4$). Among them, the monoclinic phase shows better photocatalytic performance under

visible irradiation, probably due to the lower and suitable band gap of around 2.4 eV.[25,27–30] The monoclinic $BiVO_4$ phase has been well studied as a photocatalyst, despite its role on the mechanism involved in the photocatalysis process is still open.

However, the photoactivity of pure $BiVO_4$ is limited because of its low absorption of photons and fast electron/hole pair recombination, which significantly decrease the efficiency of photocatalytic reaction.[31–34]Tthe formation of heterostructure is an important strategy to increase the lifetime of photogenerated electron/hole pair by suppressing recombination,[35,36] allowing the migration of the charges to the semiconductor surface, increasing, therefore, the occurrence of redox reactions interest over heterostructure surface.[37–43]

To the best of our knowledge, the synthesis of heterostructures, such as $BiVO_4/Bi_2O_3$ and $BiVO_4/Bi_2O_2CO_3$, has been so far little explored. Thus, the main purpose of studying these architectures is to overcome two major challenges in heterogeneous photocatalysis: (i) the activation of the semiconductor under visible irradiation and (ii) increasing the lifetime of electron/hole pair by the creation of interfaces between different semiconductors.

1.2 - Heterogeneous Photocatalysis – Fundamental Principles

Since the 1970s, the water photolysis has been extensively investigated. However, water is transparent in visible region and can be directly decomposed only by irradiation with wavelengths lower than 190 nm. While, for electrochemical decomposition of water, a potential difference higher than 1.23 V is necessary between two electrodes, the cathode and the anode, in which occur the reduction and oxidation processes, respectively. This potential difference is equivalent to the energy of radiation with a wavelength of approximately 1000 nm. In 1972, Fujishima and Honda developed an electrochemical system containing TiO_2 as the anode (photoactivated) called photoelectrochemical cell that was able to decompose water in hydrogen and oxygen under visible irradiation.[44]

They constructed an electrochemical cell in which a TiO_2 electrode (working electrode) was connected with a platinum electrode (counter electrode) through an external load. When the surface of the TiO_2 electrode was irradiated, current flowed from the platinum electrode to the TiO_2 electrode through the external circuit (FIGURE 1.1). The direction of the current reveals that the oxygen evolution occurs at the TiO_2 electrode and hydrogen evolution at the platinum electrode. It was suggested

that water can be decomposed by visible radiation into oxygen and hydrogen, without the application of any external voltage, according to the following reactions:

$TiO_2 + 2\,hv \rightarrow 2\,e^- + 2\,h^+$ (TiO_2 exciting by UV irradiation)

$2\,h^+ + H_2O \rightarrow ½\,O_2 + 2\,H^+$ (At TiO_2 electrode)

$2\,e^- + 2\,H^+ \rightarrow H_2$ (At Pt electrode)

$H_2O + 2\,hv \rightarrow ½\,O_2 + H_2$ (Overall reaction)

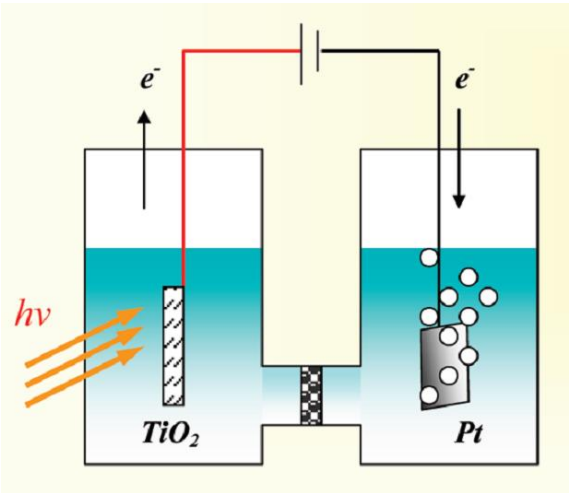

FIGURE 1.1 - Schematic diagram of the photoelectrochemical system to water splitting using a TiO_2 as the photoanode (Available at Teoh et. al.[45]).

A semiconductor is characterized by valence band (VB) and conduction band (CB) and the region between them called band gap, as shown in FIGURE 1.2. The semiconductor photocatalytic cycle can be divided in four steps: (i) when a photon with an energy of *hv* matches or exceeds the band gap energy, specific to each semiconductor, an electron, e_{cb}^-, is promoted from the VB to the CB, leaving an equal number of vacant sites (holes);[3,46] (ii) the excited electrons and holes migrate to the surface; (iii) they react with adsorbed electron acceptor and electron donors, respectively; (iv) a large proportion of electron hole pairs recombine, dissipating the input energy in the form of heat or emitted light.[20] Therefore, the main drawback of the photocatalytic process is the recombination, because this process occurs within of few nanoseconds, preventing the charges migration to semiconductor surface, so different approach has been developed to overcome this.[45] Generally, the CB electrons have a chemical potential of +0.5 to –1.5 V versus the normal hydrogen electrode (NHE), hence they can act as reductants. The VB holes (h_{vb}^+) exhibit a strong oxidative potential of +1.0 to +3.5 V versus NHE.[47] In this sense, the holes can oxidize the –OH groups or adsorbed water to $^{\bullet}OH$ radical on

semiconductor surface, which can subsequently oxidize the organic pollutants. From the point of view of semiconductor photochemistry, the role of photocatalysis is to initiate or accelerate specific reduction and oxidation (redox) reactions in the presence of irradiated semiconductors.

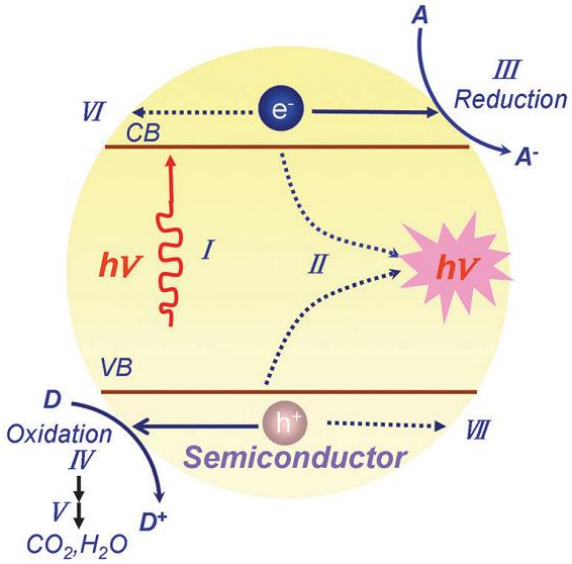

FIGURE 1.2 - Schematic illustration of the principle of semiconductor photocatalysis: (I) the formation of charge carriers by a photon; (II) the charge carrier recombination to liberate heat; (III) the initiation of a reductive pathway by a conduction-band electron; (IV) the initiation of an oxidative pathway by a valence-band hole (Available at Wang et. al.[48])

Early studies on photocatalysis mainly focused on TiO_2 due to its low cost, high efficiency, and photostability.[4,20] However, TiO_2 band gap is around 3.2 eV , i.e., it responds only to UV irradiation, which takes up only ca. 5% of the sunlight energy while visible-light accounts for ca. 43%.[4,20] Therefore, semiconductors employed as photocatalysts that can be activated by visible-light radiation have attracted intense scientific interest due to their applications in heterogeneous photocatalysis, especially for the degradation of organic contaminants as well as for water splitting and artificial photosynthesis.[25,49–55] Among the various photocatalysts, bismuth vanadate ($BiVO_4$) is a promising *n*-type semiconductor candidate for these applications due to its narrow band gap of approximately 2.4-2.8 eV, nontoxicity, high chemical stability and photo stability, and its ability to absorb sunlight.[25,27,56–58] $BiVO_4$ exists in three different crystalline phases,[29,59] among them, the monoclinic (*m*-$BiVO_4$) phase has been extensively studied

due to its better photocatalytic performance under visible irradiation, which is primarily due to the lower and more suitable band gap (i.e., approximately 2.4 eV).[60,61]

Although, several works have shown the $BiVO_4$ application potential on organic pollutant photodegradation when activated by visible radiation,[21,62,63] the pure *m*-$BiVO_4$ showed poor photocatalytic performance, mainly due to its low photon absorption and its fast charge recombination.[36] Besides, the photogenerated holes in the valence band (E_{VB} = 2.4 V vs. NHE) of *m*-$BiVO_4$ are energetically favorable to forming $^{\bullet}OH$ radical from adsorbed OH (E = 1,6 V vs NHE), but the photogenerated electrons in conduction band (E_{CB} = 0 V vs. NHE) have not enough reduction potential to O_2 reduction (E = -0,33 V vs NHE). Therefore, as the photogenerated electrons are not trap by O_2, recombination of charge takes place rapidly.[64]

Several strategies have been proposed to overcome this problem and therefore increase the photocatalytic performance of $BiVO_4$, such as: co-catalysts loading and heterostructures formation.[22] $BiVO_4$ composites with metals such as: Ag (Ag^+/Ag 0,799 V vs NHE), Au (Au^{3+}/Au 1,5 V vs NHE) e Pt (Pt^{2+}/Pt 1,2 V vs NHE), increase the lifetime of electron/hole pair because these metals can be scavenger the electron photogenerated.[31] Composites of $BiVO_4$ associated with other semiconductors (named as heterostructures) as $BiVO_4/WO_3$ has also been studied to improve their photocatalytic performance.[65]

1.3 - Heterostructures Application

In the last years, the combination of compounds with different properties in a unique material has attracted much attention due to the possibility of improving the photocatalytic performance compared to the isolated compounds. This type of architecture was the research issue of H. Kroemer and of Z. I. Alferov, awarded with de Nobel Prize in Physics in 2000.[66]

Heterostructure is a system in which materials of different composition or structure sharing the same interface, named heterojunction. This system allows the control of several fundamental parameters in technology involving semiconductors, such as, band gap, effective mass and charge carriers mobility, refraction index, and others.[48,49] A more modern definition of heterojunction is the interface between any two solid-state materials, including crystalline and amorphous structures of metallic, insulating, fast ion conductor and semiconducting materials.[67–69] The behaviour of a heterostructure depending on the band gaps and the electronic affinity of semiconductors.

Heterostructured semiconductors can be divided into three different cases: type-I, type-II and type-III band alignment as shown in FIGURE 1.3.

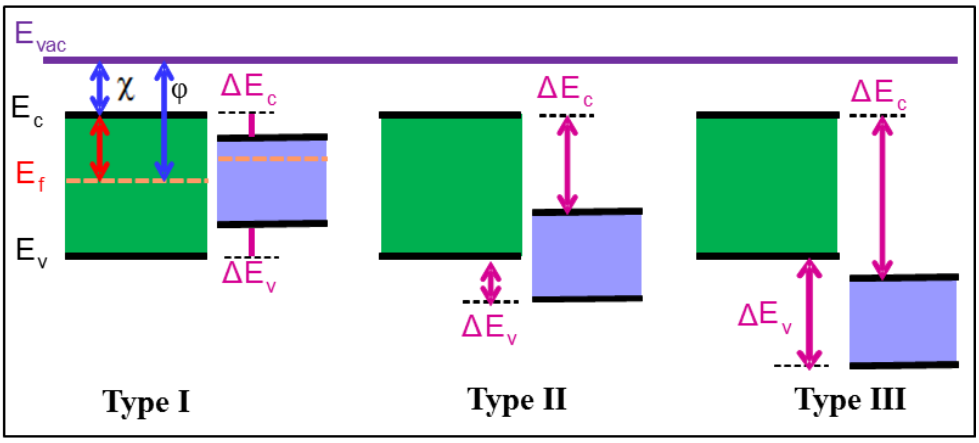

FIGURE 1.3 – The three different type of heterostructure between semiconductors. E_{vac} showed the energy reference point (vacuum); E_c is the CB energy; E_v is the VB energy; E_F is the Fermi energy; φ is the work function and χ is the electronic affinity.

Each type of heterostructure is more suitable to specific applications, depending on the electronic properties resulting from creation of the interface between the materials. The suitability of a determined heterostructure for a process is directly related with the charges migration that occurs in the interface due to the difference of the chemical potentials of the photogenerated the holes and electrons, represented by Fermi energy.[70] The charges movement toward is governed by work function of each material and it will occur until establishing the thermodynamic equilibrium. For photocatalytic purposes, the type-II heterostructure is the most suitable because the difference of chemical potential between the semiconductors causes band bending at the interface of junction.[70] The band bending induces a built-in field, which drives the photogenerated electrons and holes in opposite directions, leading to a spatial separation of these charges on different sides of heterojunction. Therefore, the formation of type-II heterostructures is an effective approach for enhancing charge carrier separation to improve photocatalytic efficiency in the environmental remediation and energy production.[37,70]

The heterostructures can be formed by heterojunctions between *p*-type and *n*-type semiconductors that have different relative valence and conduction band positions, as shown in FIGURE 1.4.[22,39] When electrons are photogenerated in the conduction band of a *p*-type semiconductor, they tend to migrate to conduction band of a *n*-type semiconductor. Similarly, holes photogenerated in the valence band of a *n*-type semiconductor tend to migrate to the valence band of a *p*-type semiconductor.[22,39,57] In a

type-II heterostructure, these processes occur spontaneously, leading to a spatial separation of the electrons and holes on different sides of heterojunction, and consequently increase the charge carriers lifetime.[69]

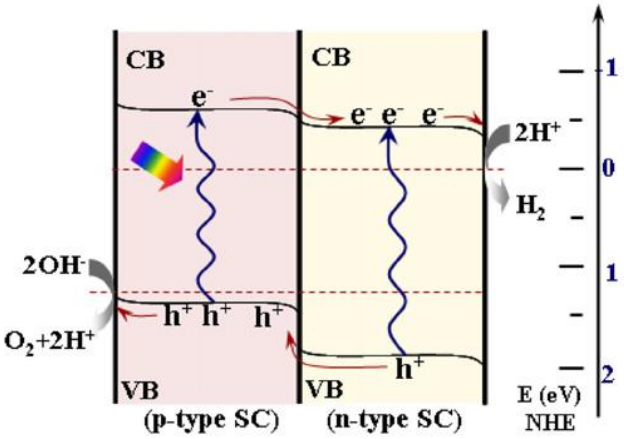

FIGURE 1.4 – Schematic illustration of a heterostructure between semiconductors *n*- and *p*-type, when the semiconductors are activated the electrons in conduction band tend to migrate from *p*- to *n*-type semiconductor, while the holes photogenerated migrate from valence band of a *n*- to *p*-type semiconductor (Available at Jang et. al.[22])

As regards to $BiVO_4$ associated to other semiconductors to form heterostructures, some works showed that heterojunctions formed increase the efficiency of photocatalytic process when compared with phases separately.[25] Several semiconductors, such as WO_3,[65,71] C_3N_4,[72,73] TiO_2,[74,75] ZnO,[76] Co_3O_4,[77] Cu_2O,[57] have been used combined with $BiVO_4$ to improve their photocatalytic performance. Recently, Wang and co-authors (2013)[57] synthesized the $BiVO_4/Cu_2O$ heterostructures by hydrothermal method and observed a significant enhancement of their photocatalytic activities for degradation of methylene blue dye and phenol when compared with $BiVO_4$ and Cu_2O isolated.[57] FIGURE 1.5 shows the probable charge transfer mechanism (forming the *p-n* type heterojunctions) and the high-resolution transmission electron microscopy (HRTEM) image in which it is possible to verify the presence of heterojunctions between $BiVO_4$ and Cu_2O.[57]

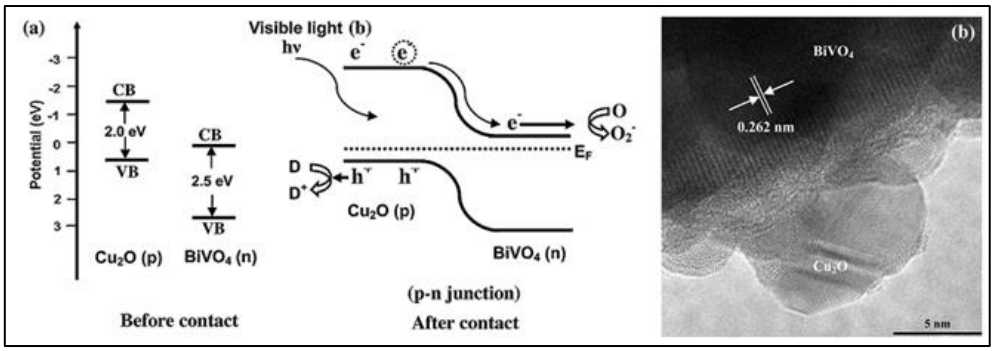

FIGURE 1.5 – a) Schematic diagram of semiconductors before of contact, and after the contact forming the p-n type heterojunction. b) HRTEM image evidenced the presence of $BiVO_4/Cu_2O$ heterostructure (Adapted from Wang et. al.[57])

Despite $BiVO_4$ coupling to several phases being widely studied, the details about the interfaces formed between $BiVO_4$ and other bismuth compounds, such as Bi_2O_3, $Bi_2O_2CO_3$, and BiOX (X = Cl, Br, I) are relatively little explored. The energetic values calculated with regard to the vacuum for the valence and conduction bands and the band gap of these semiconductors are shown in TABLE 1.1. Based on these values, it is expected the formation of type-II heterostructures by coupling of $BiVO_4$ with these phases. For example, the $BiVO_4$ (type *n*)[25,78] and Bi_2O_3 (type *p*)[79,80] semiconductors exhibit promising electronic properties to form the type-II heterostructure (*p-n* junction). Indeed, the $Bi_2O_3/BiVO_4$ heterostructure, can be activated by visible radiation, an important feature for photocatalytic applications under natural solar conditions.[25,58,78]

The formation of heterojunctions between different phases of the same material, such as Evonik P25 that is composed by anatase and rutile TiO_2 crystallites, is also a promising approach for photocatalytic applications.[81,82] Therefore, the formation of heterostructure between the monoclinic and tetragonal $BiVO_4$ phases is an interesting method for improving the photoactivity of this material.[83–85] In recent studies, different procedures for preparing *m*-$BiVO_4$/*t*-$BiVO_4$ heterostructure have been reported, and the existence of a mixed phase resulted in a higher photocatalytic activity, which was due to the separation of photoinduced electron/hole pairs.[83–85] However, the involved mechanisms have not been identified, and a clear correlation between charge separation effects and the photodegradation paths has not been established.

TABLE 1.1 - Data of electronic properties of semiconductors, $BiVO_4$, Bi_2O_3, BiOI and BiOCl.[35,80,86–89]

Semicondutor	VB (eV)	CB (eV)	Band gap
m-$BiVO_4$	2.40	0.00	2.40
t-$BiVO_4$	2.00	-0.60	2.60
Bi_2O_3	1.90	-0.70	2.60
$Bi_2O_2CO_3$	3.60	0.40	3.20

1.4 - Heterostructures Tailoring

The ability to increase the electron/hole pair lifetime in a heterostructure can only emerge if the particles are in intimate contact, that is, if there are heterojunctions between them.[37] However, the effective formation of heterojunctions between two or more semiconductors is still a challenge. Therefore, the development of efficient and cost-effective methods for combining different metal oxide nanoparticles is necessary for the improvement of technology. Different strategies have been studied to obtain the type-II heterostructures, such as one-step methods (simultaneous crystallization)[90–92] and use of one and/or both particle pre-formed (heterojunctions formation by attachment).[37,39,57] Heterojunctions are frequently achieved by thermal treatment at high temperatures, which negatively affects the properties of the nanocrystals for specific applications, such as photocatalysis, due to surface dehydroxylation and surface area reduction.[12,37]

Among the synthetic methods to obtain heterostructure by simultaneous crystallization, in which the soft-chemistry methods may be suitable for this purpose, the oxidant-peroxo method (OPM) through hydrothermal treatment is remarkable.[25,93] This method possesses several advantages for the synthesis of nanostructures, such as the low-temperatures of annealing, elimination of foreign ions or organic ligands, and control of morphology, composition and structure of the semiconductor crystals through the synthesis parameters.[91,94,95] Hydrothermal synthesis can be defined as a method of formation and growth of crystals by chemical reactions and solubility changes of substances in a sealed heated aqueous solution above ambient temperature and pressure.[96]

However, the production of such heterostructures by one-step methods has as the main the drawbacks the difficulty of controlling the simultaneous crystallization process of two different components.[37,38,42] Recently, Ye et. al. (2015)[97] proposed a synthesis method to $Bi_2O_3/BiVO_4$ heterostructured films by several processing step with high calcination temperatures requirement. Despite some interesting results through the

proposed procedure the authors identified the presence of spurious phase (V_2O_5). Cheng et. al. (2015)[98] reported an interesting method to obtain $BiVO_4/Bi_2O_3$ *p–n* heterojunction composites via a one-step mild hydrothermal, but the ratio between Bi_2O_3 and $BiVO_4$ could not be controlled.

Thus, the use of one preformed particle to build up heterostructures is of interest, because the morphology, composition and interfaces creation is easily controlled. In a system where the two constituents semiconductors has one of metal in common, for example the Bi_2O_3 and $BiVO_4$ (Bi in common), is possible create an interface between the semiconductors by growth of a phase on the sacrificial surface of preformed particle driven by difference in solubility of the compounds. Liang and co-authors (2014)[89] and De-Kun and co-authors (2012)[99], proposed a synthesis route driven by solubility difference between the Bi_2S_3 and $Bi_2O_2CO_3$, and $BiVO_4$, respectively. In these papers, it was used the principle that compounds with high solubility can be converted in compounds with low solubility, and this was observed by formation of Bi_2S_3 from $Bi_2O_2CO_3$ and $BiVO_4$, due its lower solubility.[89,99]

The formation of $Bi_2O_3/BiVO_4$ and $Bi_2O_2CO_3/BiVO_4$ heterostructures, by growth of $BiVO_4$ on Bi_2O_3 and and $Bi_2O_2CO_3$ surface, respectively, under hydrothermal conditions driven by solubility difference is an interesting way to obtain theses architectures. This proposal can be efficient, because the formation of heterojunctions is unavoidable, since mandatorily the $BiVO_4$ will grow using the bismuth present on Bi_2O_3 or $Bi_2O_2CO_3$ surface, however the combination of these phases is yet few studied.

2. - Goals and Overview

The general goal of this thesis was to study the effect of type-II heterostructure formation between *m*-$BiVO_4$ and other Bi semiconductors (*t*-$BiVO_4$, Bi_2O_3 and $Bi_2O_2CO_3$) on their photocatalytic properties.

Specific goals:

- To understand the reason for the poor photoactivity of $BiVO_4$;
- To study type-II heterostructure formation between $BiVO_4$ in the monoclinic phase with tetragonal $BiVO_4$ phase;
- To develop a synthesis method to obtain heterostructures between $BiVO_4$ and Bi_2O_3 as well as $Bi_2O_2CO_3$;
- To evaluate the role of different heterojunctions on their photocatalytic properties.

Summary of each chapter

The main idea of this thesis was to explore the formation of type-II heterostructure between *m*-$BiVO_4$ with different compounds of bismuth (*t*-$BiVO_4$, Bi_2O_3 and $Bi_2O_2CO_3$), with the purpose of overcoming two major challenges in heterogeneous photocatalysis: (i) the activation of the semiconductor under visible irradiation and (ii) increasing the lifetime of electron/hole pair recombination by the creation of interfaces between different semiconductors.

For this, initially the synthesis of pure $BiVO_4$ by the oxidant peroxide method with crystallization under hydrothermal conditions, and its catalytic performance on the photodegradation of pollutants under visible-light were studied. The photodegradation mechanism of organic pollutants catalyzed by the as-synthesized samples was evaluated to understand the main reason for the poor photoactivity of $BiVO_4$ pure. The main results of this part are presented in Chapter I.

After understanding the mechanism involved in the photocatalysis of pure $BiVO_4$, the formation of heterostructures between monoclinic/tetragonal $BiVO_4$ (*m*-$BiVO_4$/*t*-$BiVO_4$) was proposed to increase the lifetime of electron/hole pair, in a system similar to P25 (that is composed of anatase and rutile TiO_2 crystallites). It was observed that the formation of heterostructures between different phases of the same semiconductor provides a viable alternative for improving photocatalytic performance. The main results of this part are presented in Chapter II. However, the control of heterostructure composition was not possible by this synthesis method (simultaneous crystallization).

Finally, we developed a novel strategy for heterostructures tailoring based on the solubility difference of two semiconductors that possess at least one metal in common. We used as model the growth of $BiVO_4$ on preformed particles of Bi_2O_3 (Chapter III) and $Bi_2O_2CO_3$ (Chapter IV) by hydrothermal treatment with a vanadium precursor (V). The method proposed allows the control of heterostructure composition and morphology. Photocatalytic activity was enhanced by $Bi_2O_3/BiVO_4$ and $Bi_2O_2CO_3/BiVO_4$ heterostructure formation when compared with their isolated phases.

Chapter 5 presents the main conclusions of this work.

3. - Chapter I: What is the main reason for the poor photoactivity of pure $BiVO_4$?

The content of this chapter is an adaptation of the article entitled **"Synthesis of $BiVO_4$ via oxidant peroxo-method: insights into the photocatalytic performance and degradation mechanism of pollutants"** by Osmando F. Lopes, Kele T. G. Carvalho, Gabriel K. Macedo, Vagner R. de Mendonça, Waldir Avansi Jr. and Caue Ribeiro, published for New Journal of Chemistry.

Reference: New J. Chem., 2015, 39, 6231-6237.[78]

NJC

ROYAL SOCIETY OF CHEMISTRY

PAPER

View Article Online
View Journal | View Issue

CrossMark click for updates

Cite this: *New J. Chem.*, 2015, 39, 6231

Synthesis of $BiVO_4$ *via* oxidant peroxo-method: insights into the photocatalytic performance and degradation mechanism of pollutants†

Osmando F. Lopes,[ab] Kele T. G. Carvalho,[b] Gabriel K. Macedo,[c] Vagner R. de Mendonça,[d] Waldir Avansi Jr.*[e] and Caue Ribeiro[b]

3.1 - Abstract

This paper reports the synthesis of monoclinic bismuth vanadate ($BiVO_4$) by the oxidant peroxide method with crystallization under hydrothermal conditions, and its catalytic performance on the photodegradation of pollutants under visible-light. The as-synthesized $BiVO_4$ materials were characterized by means of XRD, EDX, Raman spectroscopy, UV-Vis DRS and FEG-SEM. The hydrothermal treatment above 80 °C was required to obtain pure monoclinic $BiVO_4$ phase by releasing V^{5+} ions from vanadium peroxo complexes. With the increase in hydrothermal reaction temperature, the particle size decreased. All $BiVO_4$ samples presented large size and shape distribution and band gap of approximately 2.40 eV. The as-prepared $BiVO_4$ catalysts showed high photoactivity for decomposition of model pollutants, methylene blue and rhodamine B dyes, under exposure to visible-light. The photodegradation mechanism was evaluated by adding scavengers, DMSO and $KBrO_3$, which were used to probe $^{\bullet}OH$ radical and conduction band (CB) electrons, respectively. It was observed that photodegradation of MB and RhB dyes is caused by the action of $^{\bullet}OH$ radicals, and that $BiVO_4$ CB electrons do not have reduction potential sufficiently high to reduce dissolved oxygen to $O_2^{-\bullet}$. It was proven that the indirect mechanism, i.e. $^{\bullet}OH$ radical formation, plays the major role on the $BiVO_4$-assisted photodegradation process.

3.2 - Introduction

Titanium dioxide (TiO_2)[8–13] and zinc oxide (ZnO)[14–17] are the main semiconductors applied in heterogeneous photocatalysis process such as organic pollutants degradation and water splitting.[18,19] These materials possess specific characteristics that are regarded as crucial for good photocatalytic performance under UV-light when compared with other materials, such as band gap values of 3.2 eV and 3.4 eV, respectively, suitable textural properties, and slow recombination rate of photogenerated electron/hole pair.[17,20] However, these materials can only be activated by UV radiation (wavelength below of 385 nm), which represents less than 5% of all solar energy that reachs the Earth's surface, thereby disabling their application under natural conditions.[2,4,21–24]

In this sense, semiconductors that can be activated by visible radiation have arose much scientific interest. Bismuth vanadate ($BiVO_4$) is a n-type semiconductor with band gap value ranging in 2.4 eV – 2.8 eV, depending on its crystalline phase.[25,26] $BiVO_4$ exists in three different crystalline phases: two tetragonal structures (zircon type

and scheelite type), and one monoclinic structure (scheelite type). Among them, the monoclinic phase shows better photocatalytic performance under visible radiation, probably due to the lower and suitable band gap of around 2.4 eV.[27–29] This low band gap value is a result of the hybridization between the Bi 2s orbital and the O 2p orbital, which causes a shift in the valence band, and decreases the difference of energy between the valence and conduction bands.[25,30] Although monoclinic $BiVO_4$ phase has been well studied as a photocatalyst, its role on the mechanism involved in the photocatalysis process is still open.

As a matter of fact, photocatalytic performance of semiconductors is also influenced by their structural, electronic and morphologic characteristics, and the procedure used to synthesize the photocatalysts has direct effects on their properties.[11,15,21,91,100,101] Several methods have been used to obtain photocatalysts such as sol-gel technique, polymeric precursor method, oxidant peroxide method (OPM), precipitation and co-precipitation.[25,93] Among these, the OPM method with crystallization under hydrothermal conditions is a remarkable route, since it possesses several advantages for the synthesis of nanostructures, especially the low-temperatures of crystallization, elimination of foreign ions or organic ligands, and control of morphology and structure of the semiconductor crystals through the synthesis parameters.[91,94,95]

Therefore the aim of this study was to develop a new method to obtain monoclinic $BiVO_4$ at low-temperature, and to evaluate the photocatalytic performance of this semiconductor under visible-light. The effect of the hydrothermal treatment on the structural, electronic and morphologic properties of the $BiVO_4$ is described in this paper. Furthermore, we studied the major mechanism involved in the photodegradation of model pollutants by examining the behavior of different scavengers in the photocatalytic process, and by detection of hydroxyl radical.

3.3 - Experimental

Synthesis of $BiVO_4$ - $BiVO_4$ samples were obtained using the oxidant peroxide method (OPM) succeeded by crystallization under hydrothermal conditions. First, 0.69 g of $Bi(NO_3)_3.5H_2O$ (Vetec - Sigma) and 0.16 g of NH_4VO_3 (Vetec - Sigma) were added to 40 mL of distilled water under vigorous stirring, where the Bi:V molar ratio was kept at 1:1. Then, hydrogen peroxide (H_2O_2 30%, Synth) was added to the solution with H_2O_2:M molar ratio equal to 10:1 (where M is the sum of Bi and V mols). The solution instantaneously presented a yellow color, which indicated formation of

vanadium peroxo complex.[95] This complex was crystallized for 12 hours using a homemade hydrothermal reactor, where the synthesis temperature was varied in the range between 80 °C and 160 °C. A synthesis at room temperature (25 °C) was also performed in order to understand the effect of the hydrothermal treatment on the material crystallization. The samples were washed three times with distilled water, and subsequently with isopropyl alcohol, being afterwards separated by centrifugation and dried in an oven at 60 °C for 12 h. The sample obtained at room temperature was identified as BV-25, and the other samples were identified as BV-HTXX, where HT refers to "hydrothermal treatment" and XX is the synthesis temperature.

Powder Characterization - Powder X-ray diffraction (XRD) was conducted in a Shimadzu XRD6000 diffractometer operating with Cu Kα radiation generated at 30 kV and filament current of 30 mA. The 2θ range from 10 to 70° was continuously scanned with a speed of 1° min^{-1} and a step width of 0.02°. Raman spectroscopy measurements were performed in a FT-Raman spectrometer (Bruker RAM II with a Ge detector), equipped with a Nd:YAG laser with wavelength centered at 1064 nm. Ultraviolet–visible diffuse reflectance spectroscopy (DRS) was carried out with a Cary 5G spectrometer in the total reflection mode with an integration cell and scanned wavelength range of 200-800 nm.

A field emission gun scanning electron microscope (FEG-SEM Jeol JSM 6701F) running at 5 kV was used to verify the material morphology. Semi-quantitative atomic compositions were evaluated by energy-dispersive X-ray (EDX) spectrometry using a Thermo Noran device coupled to a SEM (Jeol JEM 2010). The analysis of N_2 adsorption at 77 K was conducted in a Micrometrics ASAP 2000, and the specific surface area (SSA) was obtained by the application of BET modeling. Before these analyses, the samples were pre-treated (degasification) by heating at 80 °C under vacuum until reaching a degassing pressure of less than 10 μm Hg.

Photocatalytic Properties and Mechanism Evaluation - The photocatalytic activity of the as-synthesized $BiVO_4$ samples was evaluated by studying the photodegradation of methylene blue (MB) dye, which is considered one of the most common chemicals used in industrial processes, and often causes environmental pollution.[12,100] In order to perform the photocatalysis experiments, 10 mg of the as-synthesized sample were added to 20 mL of 5 mg L^{-1} MB aqueous solution. All experiments were perfomed at pH=6.5. The as-prepared dispersions were stirred and exposed to visible light radiation in a homemade photo-reactor with six fluorescent

lamps(Osram, 15 W and maximum intensity at 440 nm) operating at 18 °C. The representative image of the photo-reactor is showed in Appendix A (FIGURE A1). The MB photodegradation was monitored by its absorption maximum at 665 nm at regular periods of time using a UV-Vis spectrophotometer (Shimadzu – 1601PC) in the absorbance mode. In order to reach adsorption equilibrium the samples were previously kept in contact with the MB dye solution for 12 h in the dark. For comparative purposes, the photocatalytic behavior of a pristine commercial tetragonal Bi_2O_3 phase (Sigma-Aldrich, nanopowders 200 nm) was also evaluated. The crystalline phase, particle size and morphology of Bi_2O_3 were confirmed by XRD and FEG-SEM (FIGURE A2 and FIGURE A3 in Appendix A, respectively). DRS spectra was performed to answer the suitability of Bi_2O_3 as reference compound under visible light (see in Appendix A, FIGURE A2). The tetragonal Bi_2O_3 phase presented the band gap of 2.48 eV, as expected.[102] Therefore, the Bi_2O_3 used as reference in this work absorb photons at similar energies when compared with as-synthesized $BiVO_4$ samples. So, tetragonal Bi_2O_3 phase is a suitable photocatalyst for use as reference in photocatalytic process lead under visible light.

Two different methods were used to investigate the MB photodegradation mechanism catalyzed by $BiVO_4$. The first one consisted in adding reactive species scavengers directly to the $BiVO_4$-containing MB solutions. In this procedure, dimethyl sulfoxide (DMSO) and potassium bromate ($KBrO_3$) were added as scavengers for ·OH radicals and CB electrons, respectively.[103] The second method consisted in detecting indirectly ·OH radicals employing the technique described by Ishibashi et al (2002),[104,105] in which alkaline terephthalic acid (TA) solution instead of MB solution is mixed with $BiVO_4$ in the photo-reactor. TA readily reacts with $^{\bullet}OH$ and forms a highly fluorescent product, 2-hydroxyterephthalic acid. This product has a fluorescence emission at around 425 nm, and its amount is proportional to the amount of ·OH radicals formed during the photocatalytic process.[95] The concentration of TA was set at $5x10^{-4}$ mol L^{-1} in a dilute NaOH ($2x10^{-3}$ mol L^{-1}) solution.[95] At regular time intervals, aliquot parts of the suspension were collected and analyzed in a LS 50B fluorescence spectrometer (Perkin Elmer). The fluorescence emission spectra were obtained with excitation wavelength of 315 nm.

3.4 - Results and discussion

The XRD patterns for the as-synthesized $BiVO_4$ samples are shown in FIGURE 3.1. It is noted that the sample obtained without hydrothermal treatment (BV-25), presented a mixture of crystalline phases. The diffractions peaks were indexed as belonging to tetragonal $Bi_6O_6(OH)_3](NO_3)_3 \cdot 1.5H_2O$ phase (JCPDS: 53-1038, highlighted for #) and vanadium hydrogen oxide ($H_{3.7}V_6O_{13}$) (JCPDS: 38-0008, highlighted for *). It was also observed that the BV-25 suspension maintained its yellow color (the same characteristic color of the vanadium peroxo-complex) even after synthesis and centrifugation, indicating that the V^{5+} ions were not completely released from the complex, and the $BiVO_4$ formation was incomplete.[106] Conversely, the XRD patterns for the samples synthesized by hydrothermal treatment under temperatures ranging from 80 °C to 160 °C (FIGURE 3.1) were similar and presented well-defined peaks, which could be indexed as the pure monoclinic $BiVO_4$ crystalline phase (JCPDS – 83-1699). This is possibly explained by the fact that H_2O_2 reacts with V^{5+} ions forming the stable peroxo-complex under environmental conditions during relative short periods of time.[106] Thus, the subsequent hydrothermal treatment, even when performed at 80 °C, provides sufficient energy to degrade the vanadium peroxo-complex, making all V^{5+} ions free to form the $BiVO_4$ structure. Thus, XRD results clearly showed that the hydrothermal treatment has a fundamental role in the synthesis of pure monoclinic $BiVO_4$. Further increases in the temperature of hydrothermal treatment did not lead to any significant long range structural changes in the $BiVO_4$ samples.

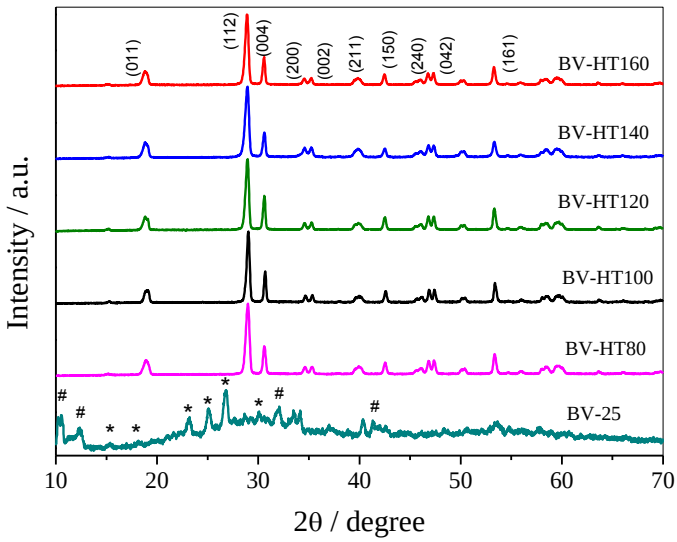

FIGURE 3.1 - Powder XRD patterns of as-synthesized $BiVO_4$ samples.

Additionally, the semi-quantitative EDS analysis, performed on the sample BV-25 (FIGURE 3.2), confirmed the presence of only Bi and V elements with approximately 71% and 15% atomic percentages of Bi and V, respectively. This confirms that V^{5+} ions were not totally released at room temperature. The small peak below 0.5 keV and the peaks around 1.5 keV are related to the presence of carbon (C) from carbon conductive adhesive and the aluminum (Al) of stub, respectively.

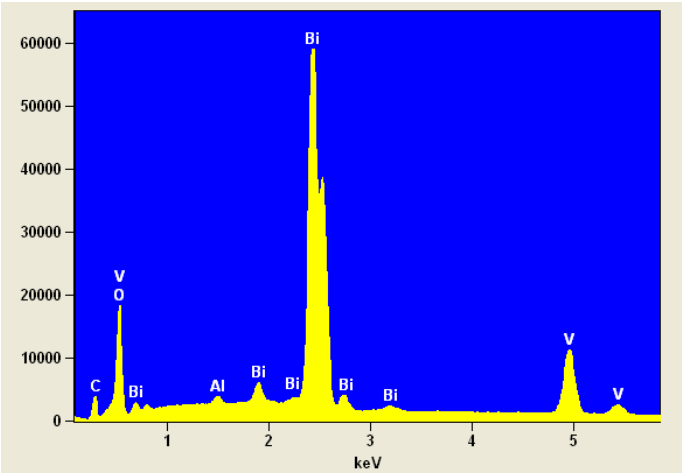

FIGURE 3.2 - EDS analysis of BV-25. The peaks related to O, Bi and V are identified in the plots.

Raman spectroscopy was performed in order to access medium-range order effects in the hydrothermally treated $BiVO_4$ samples, as seen in FIGURE 3.3. The BV-HTXX samples, i.e. those obtained via hydrothermal treatment, presented similar spectra with five main Raman shifts at 120 cm^{-1}, 200 cm^{-1}, 330 cm^{-1}, 362 cm^{-1} and 826 cm^{-1}. The peaks at 120 cm^{-1} and 200 cm^{-1} are related to external mode of $BiVO_4$; the peaks at 330 cm^{-1} and 362 cm^{-1} are ascribed to the asymmetric and symmetric deformation modes, respectively, of V-O bonds in the VO_4 tetrahedrons; and the peak at 826 cm^{-1} can be assigned to the symmetric stretching of V-O mode with A_g symmetry.[29,56] It can be verified that these bands were not shifted as the temperature of the hydrothermal treatment was increased, meaning that none significant medium-range structural change occurred in the BV-HTXX samples, confirming the XRD results (FIGURE 3.1). Furthermore, the BV-25 sample exhibited Raman scattering different from the BV-HTXX series, as expected.

The band gap values of the as-synthesized $BiVO_4$ samples were determined by applying the Tauc equation[107] to the diffuse reflectance spectroscopy UV-Vis data (FIGURE 3.4). The band gap was calculated assuming that $BiVO_4$ has a direct-

type transition, by ploting the $(\alpha h\nu)^2$ *versus* $h\nu$.[25] The band gaps values for the $BiVO_4$ samples exhibited small fluctuations, ranged from 2.35 eV to 2.45 eV (TABLE 3.1), in a good agreement with literature.[27,56] Therefore, different temperatures of hydrothermal treatment did not induce any significant changes in electronic properties, allowing activation of the as-synthesized $BiVO_4$ samples by visible-light. The BV-25 sample showed two distinct band gaps of 2.41 eV and 2.76 eV, highlighting the presence of two different crystalline phases, as observed by XRD and Raman scattering.

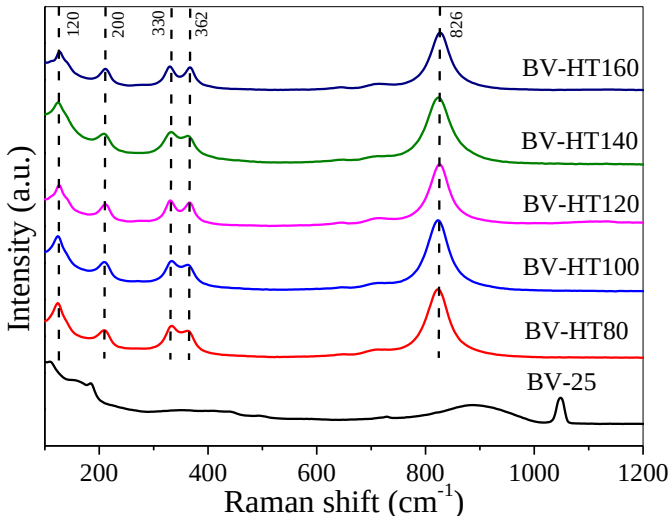

FIGURE 3.3 - Raman scattering spectra of the as-synthesized $BiVO_4$ samples.

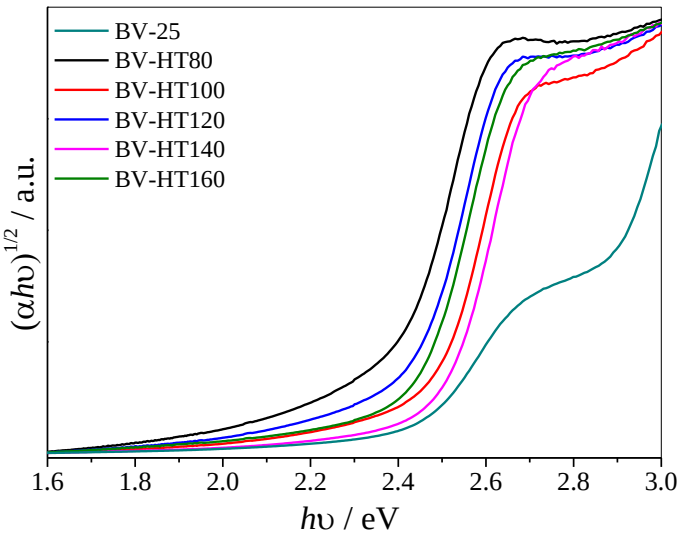

FIGURE 3.4 - A plot of $(\alpha h\upsilon)^{1/2}$ vs. photon energy ($h\upsilon$) obtained by Tauc equation from DRS spectra.

The morphology of the $BiVO_4$ samples was examined by FEG-SEM, and representative images are presented in FIGURE 3.5. The BV-25 sample displayed irregular micrometric particles with different sizes, while for the BV-HT80 sample well

faceted particles also with different sizes and shapes can be noted. On the other hand, for the BV-HT100 sample it was possible to observe the presence of more elongated particle branched in two axes, the known fish-bone $BiVO_4$ morphology.[108] Further increase in temperature (120 °C, 140 °C, and 160 °C) led to smaller particles in relation to BV-HT100. The size distribution of the particles was estimated using the software Image Pro Plus, by counting an average of 200 particles in different images (FIGURE A4). It was observed an average size equal to 828 nm, 443 nm and 561 nm for BV-HT120, BV-HT140 and BV-HT160 samples, respectively. Therefore, the sizes of BV-HT140 and BV-HT160 are similar, since both distributions are wide but presenting lower sizes than BV-HT120. Despite the fact that the BV-HT120, BV-HT140 and BV-HT160 samples had a wide distribution of sizes, it is clear that increasing temperature of hydrothermal treatment decreases particles size of $BiVO_4$.[109]

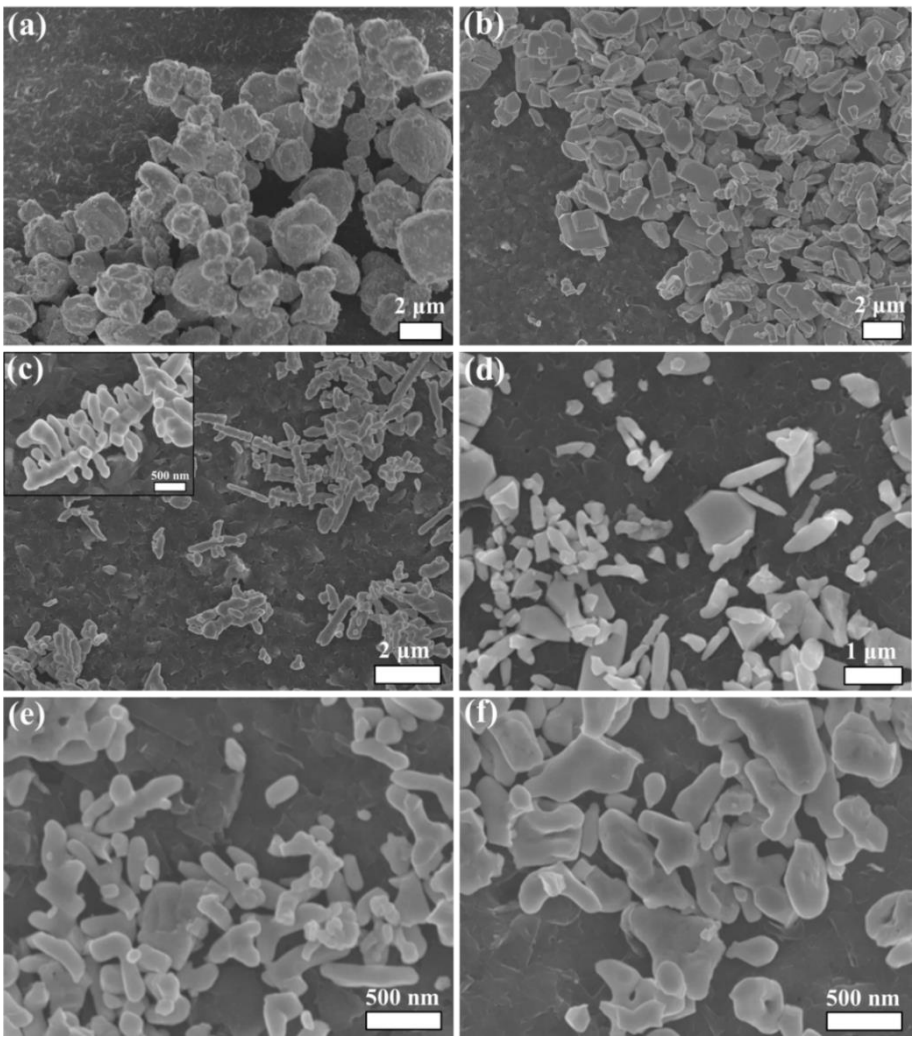

FIGURE 3.5 – Representative FEG-SEM images of (a) BV-25, (b) BV-HT80, (c) BV-HT100, (d) BV-HT120, (e) BV-HT140, and (f) BV-HT160. A magnification of a single particle is shown as an insert in c.

The photocatalytic properties of the as-synthesized samples were initially tested by using MB dye photodegradation induced by visible-light (FIGURE 3.6a). The commercial Bi_2O_3 nanopowder, employed as referential catalyst in the photocatalytic tests, presented lower photoactivity than all synthesized samples including that obtained at 25 °C. The direct photolysis of MB without catalyst was of approximately 8% after 3h exposure to visible-light. The BV-25 sample led to MB photodegradation of approximately 20%, and the MB photodegradation catalyzed for the BV-HTXX samples ranged from 40 to 50%, Fig. 6. These results confirm that the hydrothermal treatment step plays a fundamental role on the synthesis of highly efficient $BiVO_4$ photocatalysts, since the BV-25 sample (mixed $[Bi_6O_6(OH)_3](NO_3)_3 \cdot 1.5H_2O$ and $H_{3.7}V_6O_{13}$ phases) presented the lowest photoactivity among all synthesized samples.

TABLE 3.1 - Band gap values of the as-synthesized samples.

Sample	***Band gap* / eV**
BV-25	2.41/2.76
BV-HT80	2.35
BV-HT100	2.45
BV-HT120	2.40
BV-HT140	2.45
BV-HT160	2.40

In order to test the reproducibility of the photocatalytic tests, the experiments were performed in triplicate, and the first-order rate constant was calculated for each condition (TABLE 3.2). The R^2 values (higher than 0.97), confirm that the pollutant photodegradation follows a first-order mechanism. It can be observed that there was no significant photocatalytic activity difference in the BV-HTXX series if the standard deviation is taken into account. This result was expected, since the changes in temperature did not modify the features (structural, electronic and morphologic) of the $BiVO_4$ samples. All synthesized $BiVO_4$ samples presented specific surface area (SSA) below of 1 $m^2.g^{-1}$, and any significant difference between samples was verified. Therefore, we considered that the temperature treatment has not significant influence in SSA, and consequently SSA does not plays a fundamental role in this specific case. For the Bi_2O_3 samples (used as reference compound) the SSA presented the value equal to 2.8 $m^2.g^{-1}$. Despite the fact that the reference compound presented higher SSA compared to the as-synthesized samples, the performance in MB photodegradation of synthesized samples was significant higher.

The photoactivity of the BV-HTXX series was also examined for degradation of dyes with different physical-chemistry characteristics. The BV-HT120 sample (intermediate synthesis condition) was chosen as a representative sample in the study of RhB dye degradation under visible-light (FIGURE 3.6b). The result shown in FIGURE 3.6b is remarkable, since the as-synthesized $BiVO_4$ presents activity for degradation of different organic pollutants. Even though $BiVO_4$ samples presented lower photoactivity for RhB dye photodegradation compared with MB dye, its clear that the photoactivity can be improved by optimizing experimental conditions, such as pH, ionic strength and enhancement in dispersion by sonication.[100,110,111] Additional investigations in future works are necessary for its optimization.

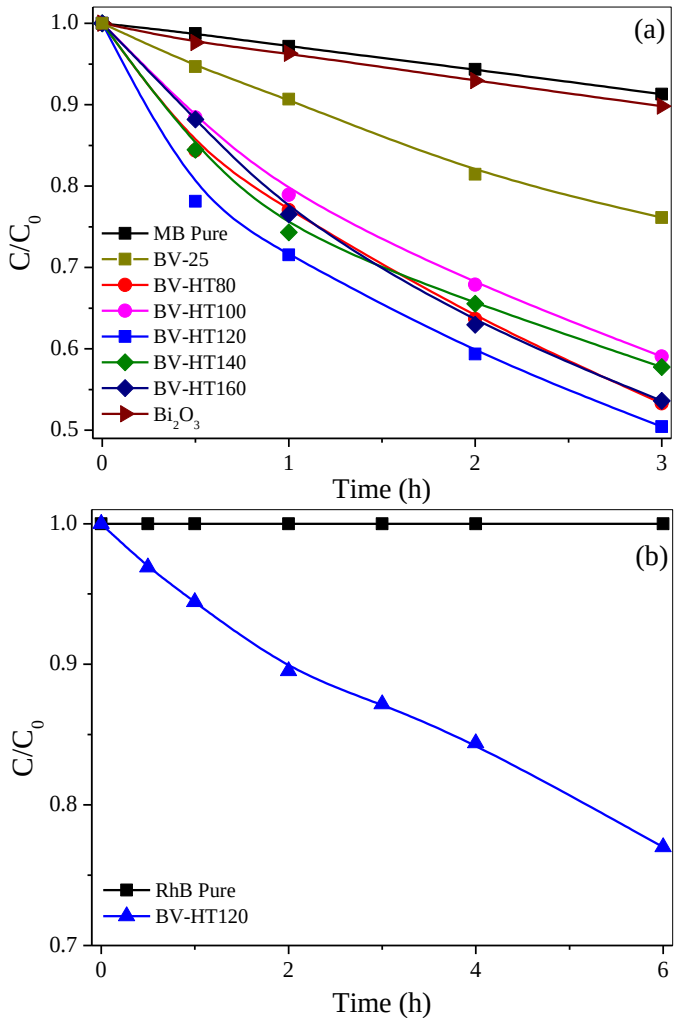

FIGURE 3.6 - (a) Photodegradation kinetics of MB dye (C_0 = 5 mg L-1) catalyzed by $BiVO_4$ as a function of visible-light exposure time; (b) Photodegradation kinetic of RhB dye (C_0 = 5 mg L-1) catalyzed by BV-HT120.

The monoclinic $BiVO_4$ phase has been extensively studied for applications in photocatalysis,[21,63,64,109] but few studies were aimed to elucidate the mechanism involved in the photocatalytic process. There are three principal mechanisms that may be involved in the catalyst-assisted photodegradation of pollutants: indirect mechanism, direct mechanism, and photosensitization process.[12,95,112–116] Initially, we studied the photocatalytic mechanism by analyzing the effects of the addition of two different reactive scavenger species to MB solution during photocatalysis: $KBrO_3$ (strong oxidant, CB electrons acceptor) and DMSO (a ·OH scavenger).[24,103] The representative BV-HT120 sample was used in these experiments, and the results are shown in FIGURE 3.7a. The dissolved oxygen is considered to be a CB electrons scavenger that inhibits fast charge carrier recombination, and consequently formation of superoxide radical ($O_2^{-\bullet}$), which is much important for some photodegradation processes.[117] Therefore, a rational way of evaluating the importance of $O_2^{-\bullet}$ is to scavenge it with $KBrO_3$.[24,103] In this sense, if the photodegradation process is driven by $O_2^{-\bullet}$ radicals, the reaction rate is expected to be greatly decreased. On the other hand, if $^{\bullet}OH$ radicals play the major role on the photodegradation process, the reaction rate should be decreased in presence of excess DMSO.[24,103,118]

TABLE 3.2 - First-order rate constants for the MB dye photodegradation reaction performed under visible irradiation.

Sample	***k* x 100 (h^{-1})**	**R^2**
Blank	0.3	0.998
BV-25	0.9 ± 0.1	0.980
BV-HT80	2.0 ± 0.2	0.980
BV-HT100	2.1 ± 0.3	0.970
BV-HT120	1.8 ± 0.3	0.970
BV-HT140	1.7 ± 0.2	0.970
BV-HT160	2.0 ± 0.2	0.986

As can be seen in FIGURE 3.7a, the excess of $KBrO_3$ in MB solution caused a great increase in the photodegradation rate, from around 40% to 48% after 3 h of exposure to visible-light (the rate constant underwent an increase of 25%). In order to check the effect of $KBrO_3$, the blank experiment with and without $KBrO_3$ in MB dye (in absent of photocatalyst) were performed and was not verified any effect in MB removal related to its presence. Thus, the effect of MB photodegradation was strictly related to electronic characteristics of the as-prepared photocatalyst. Two facts arose from this

result: first, the $O_2^{-\bullet}$ radical has a negligible effect on the MB photodegradation mechanism probably because the conduction band edge potential of $BiVO_4$ is not sufficiently high to reduce the dissolved oxygen, the irrelevant effect of dye-photosensitized mechanism on MB photodegradation was demonstrated also.[57,65] The second fact is that a suitable CB electrons acceptor, as $KBrO_3$, can enhance the photoactivity of the $BiVO_4$ sample by inhibiting fast charge carrier recombination. Then different schemes to improve the photocatalytic performance of the $BiVO_4$ samples can be performed such as use of sacrificial reagent (e.g., Ag^+ and Au^{3+} cations) to scavenge CB electrons, and formation of heterostructures with metals and other suitable oxides.

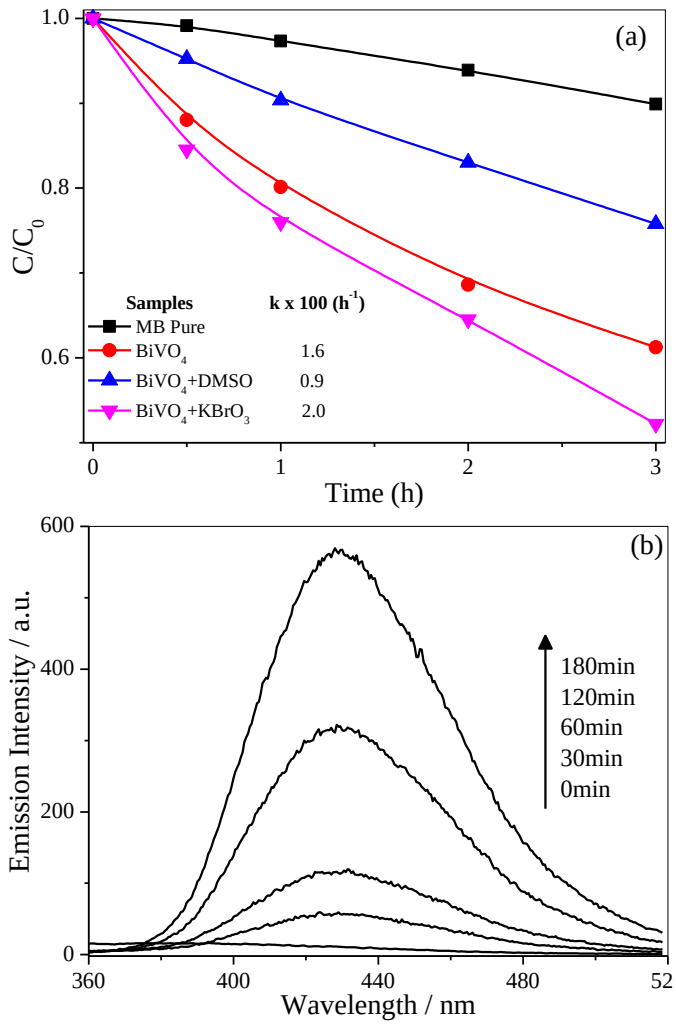

FIGURE 3.7 – (a) Photodegradation kinetic of MB dye (5 $mg.L^{-1}$) catalyzed by BV-HT120 in the presence of $KBrO_3$ (scavenger of CB electrons) and DMSO (scavenger of $^{\cdot}OH$ radicals). Kinetic rate constant values were added as an insert. (b) Spectral profile of 2-hydroxyterephthalic acid produced by BV-HT120, to detect radical $^{\cdot}OH$ indirectly, as a function of visible-light exposure time.

The second scavenger, DMSO, can react quickly with ˙OH, forming a stable adduct, thus making the DMSO excess in MB solution capture all ˙OH radicals produced during the photocatalytic process.[118] As shown in FIGURE 3.7a, the use of DMSO in excess considerably decreased the photodegradation rate from 40% to 25% after 3 h exposure (the rate constant underwent a decrease of 45%). Thus, it can be suggested that the indirect mechanism, i.e., ˙OH radical generation has a major contribution for the MB dye photodegradation process.

In order to confirm the role played by ˙OH radicals on the photocatalytic mechanism its detection was performed using terephthalic acid (TA) was used as a fluorescent probe.[104] The ˙OH radical is trapped by TA producing fluorescent 2-hydroxyterephthalic acid, as illustrated in FIGURE 3.7b. The increases in the intensity of emission shows that 2-hydroxyterephthalic acid was produced over time, proving that $BiVO_4$ sample produced hydroxyl radicals. This confirms the results obtained with DMSO scavenger, i.e., the leading mechanism of MB dye photodegradation is based on hydroxyl radical attack. This finding was unexpected, since the generally proposed mechanisms of photodegradation reactions catalyzed by $BiVO_4$ are based mainly on $O_2^{\bullet-}$ generation[119] and/or photosensitization .[113,114,120] According to our results, the mechanism of photodegradation for organic pollutants on the surface of $BiVO_4$ photocatalyst, in the absence or presence of scavengers, is schematically represented in FIGURE 3.8.

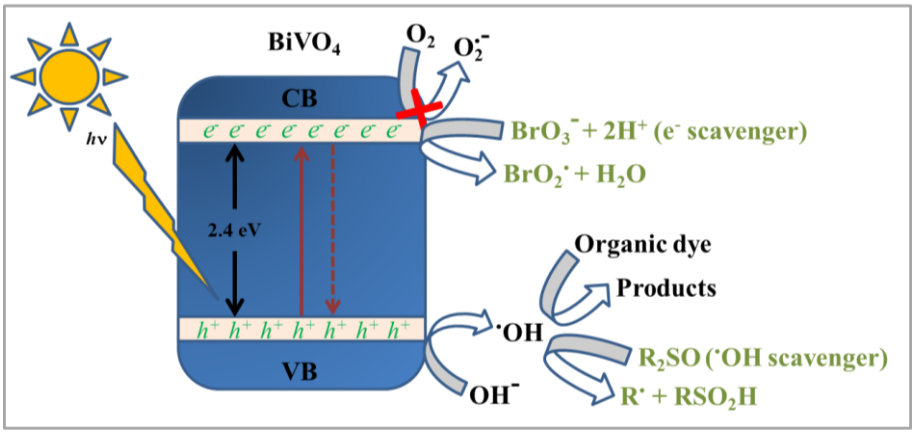

FIGURE 3.8 – Proposed mechanism for the photocatalytic reaction at the $BiVO_4$ photocatalyst surface in the absence or presence of scavengers.

3.5 - Conclusions

In summary, the synthesis proposed in this work was efficient in obtaining monoclinic $BiVO_4$ at low temperatures. The as-prepared $BiVO_4$ displayed efficient

photoactivity on the decomposition of model pollutants, methylene blue and rhodamine B dyes, under visible-light. The hydrothermal treatment was required to release V^{5+} ions from vanadium peroxo complexes, forming monoclinic $BiVO_4$ phase with band gap of around 2.40 eV. The addition of two different radical scavengers to MB solutions during photocatalysis showed that the indirect mechanism, i.e., generation of $^{\bullet}OH$ radicals has an important contribution for the photodegradation process, and that $BiVO_4$ CB electrons do not have sufficient reduction potential enough to reduce the oxygen dissolved to $O_2^{-\bullet}$. It was proven that suitable schemes (use of sacrificial reagents and formation of heterostructures between metals and oxides with $BiVO_4$) enhance the $BiVO_4$ photocatalytic performance.

4. Chapter II: Is it possible to obtain a suitable heterostructure by combining $BiVO_4$ in different phases?

The content of this chapter is an adaptation of the article entitled **"Controlled synthesis of $BiVO_4$ photocatalysts: Evidence of the role of heterojunctions in their catalytic performance driven by visible-light"** by Osmando F. Lopes, Kele T. G. Carvalho, André E. Nogueira, Waldir Avansi Jr. and Caue Ribeiro, published for Applied Catalysis B: Environmental.

Reference: Applied Catal., B., 2015, 39, 6231-6237.

Applied Catalysis B: Environmental 188 (2016) 87–97

Contents lists available at ScienceDirect

Applied Catalysis B: Environmental

journal homepage: www.elsevier.com/locate/apcatb

Controlled synthesis of $BiVO_4$ photocatalysts: Evidence of the role of heterojunctions in their catalytic performance driven by visible-light

Osmando F. Lopes [a,b], Kele T.G. Carvalho [b], André E. Nogueira [b], Waldir Avansi Jr. [c], Caue Ribeiro [b,*]

[a] Departamento de Química, Universidade Federal de São Carlos—UFSCar, Rod. Washington Luiz, km 235, CEP 13565-905 São Carlos, SP, Brazil
[b] Laboratório Nacional de Nanotecnologia para o Agronegócio (LNNA)—Embrapa Instrumentação, Rua XV de Novembro, 1452, CEP 13560-970 São Carlos, SP, Brazil
[c] Departamento de Física, Universidade Federal de São Carlos, Rod. Washington Luiz, km 235, CEP 13565-905 São Carlos, SP, Brazil

4.1. - Abstract

Despite heterostructured semiconductors gaining attention as photocatalysts due to their improved activity compared to that of the isolated materials, the role of these heterojunctions in charge separation (electron/hole) remains unclear. Therefore, we studied these aspects in monoclinic/tetragonal $BiVO_4$ (*m*-$BiVO_4$/*t*-$BiVO_4$) heterostructures, which was chosen as an active material model under visible irradiation. The synthetic route was based on vanadium peroxo complex preparation as an intermediate step in structure formation using a hydrothermal process. When V_2O_5 was used at a molar ratio of 5:1 H_2O_2:(Bi + V) with 24 h of annealing, the *m*-$BiVO_4$/*t*-$BiVO_4$ heterostructure was obtained, and this material exhibited better photocatalytic performance in methylene blue degradation under visible irradiation than isolated phases. The HRTEM images revealed that heterostructured sample was composed of nanoparticles of *m*-$BiVO_4$ and *t*-$BiVO_4$ with size lower than 10 nm, the interface of *m*-$BiVO_4$/*t*-$BiVO_4$ was also evidenced. Surprisingly, despite the *t*-$BiVO_4$ structure being less active than *m*-$BiVO_4$, the heterostructures with a higher *t*-$BiVO_4$ content were more photoactive. The *m*-$BiVO_4$/*t*-$BiVO_4$ heterostructure showed no significant deactivation even after four successive re-uses for MB photodegradation. Oxidation mechanism of the MB dye was elucidated by mass spectroscopy. Indeed, the species scavenger trapping experimental results reveal the formation of a type-II heterostructure that led to an increase in the charge carrier lifetime, where the holes (h^+), superoxide anion radicals ($O_2^{-\bullet}$) and hydroxyl radicals ($^\bullet OH$) are the main active species.

4.2. - Introduction

Semiconductors employed as photocatalysts that can be activated by visible-light radiation have attracted intense scientific interest due to their applications in heterogeneous photocatalysis, especially for the degradation of organic contaminants as well as for water splitting and artificial photosynthesis.[25,49–55] Among the various photocatalysts, bismuth vanadate ($BiVO_4$) is a promising n-type semiconductor candidate for these applications due to its narrow band gap of approximately 2.4-2.8 eV, nontoxicity, high chemical stability and photo stability, and its ability to absorb sunlight.[25,27,56–58] $BiVO_4$ exists in three different crystalline phases.[29,59] Among these phases, the monoclinic (*m*-$BiVO_4$) phase has been extensively studied due to its better photocatalytic performance under visible-light radiation, which is primarily due to the lower and more suitable band gap (i.e., approximately 2.4 eV).[60,61]

Recently, our group demonstrated that the *m*-$BiVO_4$ photoactivity was limited by its inability to reduce O_2 to $O_2^{\bullet-}$ (superoxide radical) and trap the electron photogenerated on the conduction band (CB).[121] Several strategies have been proposed to increase the performance of these photocatalysts[5,122,123] including doping,[124–126] co-catalysts loading,[127–129] and heterostructures formation.[57,65,75,86] The formation of heterojunctions between different phases of the same material is a promising approach for photocatalytic applications.[82–84,130] In addition, the formation of heterostructure between the monoclinic and tetragonal $BiVO_4$ phases is an interesting method for improving the photoactivity of these systems.[82–85,130] In recent studies, different procedures for preparing m-BiVO4/t-BiVO4 heterostructure have been reported, and the existence of a mixed phase resulted in a higher photocatalytic activity, which was due to the separation of photoinduced electron/hole pairs. However, this mechanisms involved have not been identified, and a clear correlation between charge separation effects and the photodegradation paths has not been established.

Therefore, the aim of this study was to analyze the photodegradation mechanisms and the effects of charge transfer on enhancing the activity of *m*-$BiVO_4$/*t*-$BiVO_4$ heterostructures and correlate these factors to the structural features. A synthesis method based on the previous preparation of V peroxo complexes and crystallization using a hydrothermal process has been developed. The photocatalytic activity of the as synthesized $BiVO_4$ pure and heterostructured samples were investigated for the photodegradation of MB dye in an aqueous solution, under visible irradiation**.**

4.3. - Experimental

Synthesis of materials - The oxidant peroxide method (OPM) with crystallization under hydrothermal conditions is a good route for obtaining oxide semiconductors with desirable properties for photocatalytic applications because has several advantages for the synthesis of nanostructures.[91,94,95,112,131–135] This method was used to prepare $BiVO_4$ samples using different vanadium precursors (i.e., ammonium metavanadate (NH_4VO_3, ≥ 99.0 %, Vetec - Sigma) or vanadium oxide (V_2O_5, ≥ 98.0 %, Sigma)) with different hydrogen peroxide (H_2O_2, 30 %, Synth) concentrations.

In a typical synthetic procedure,[121] 0.69 g of bismuth nitrate ($Bi(NO_3)_3.5H_2O$, ≥ 99.0 %, Aldrich) and 0.16 g of NH_4VO_3 or 0.13 g of V_2O_5 were dissolved in 40 mL of distilled water under vigorous stirring at room temperature. To study the effect of different hydrogen peroxide concentrations, H_2O_2 was added to the

solution at a H_2O_2:M molar ratio equal to 5:1 or 10:1 (where M is the sum of the moles of Bi and V). The solution instantaneously exhibited a yellow color, which indicates the formation of the vanadium peroxo complex.[106] This complex was crystallized for 12 and 24 h at 120 °C under stirring using a homemade hydrothermal reactor. Then, the obtained material was cooled to room temperature, centrifuged, repeatedly washed to remove impurities and dried overnight at 50 °C.

The as-synthesized $BiVO_4$ samples are referred to as Vp-C-t, where p is the vanadium precursor (p = 1 represents the NH_4VO_3 and p = 2, the V_2O_5), C is the H_2O_2 concentration, and t is the crystallization time.

Characterization of materials - The X-ray diffraction (XRD) patterns were recorded on a Shimadzu XRD 6000 diffractometer using Ni-filtered Cu kα (λ = 0.15406 nm) radiation operated at 30 kV and 30 mA in continuous scanning mode at a speed of 1° min^{-1} and a step width of 0.02° from 10 to 70° 2θ. UV-Vis diffuse reflectance spectra were recorded on a Varian model Cary 5G spectrometer from 200 to 800 nm to determine the band gap of the materials. The measurements were performed in total reflection mode with an integration cell containing MgO as a reference. To obtain the specific surface area (SSA) of the samples, N_2 adsorption analysis was performed at -196 °C using a Micrometrics ASAP 2000, and the respective SSA was obtained via BET modeling. Prior to the analyses, the samples were pre-treated (degasification) by heating at 80 °C under vacuum until reaching a degassing pressure lower than 10 μmHg. The zeta potential measurements were performed using Malvern – ZetaSizer model nano-ZS equipment with the catalyst in a water suspension (0.5 g L^{-1}).

The morphology and particles size of the samples were investigated using scanning electron microscopy (SEM) with a field emission gun (FEG) JEOL JSM 6701F. High resolution transmission electron microscopy (HRTEM FEI - TECNAI LaB6) operating at 200 kV was employed to verify the formation of heterostructures. TEM samples were prepared by wetting carbon-coated copper grids with a drop of colloidal alcoholic suspensions, followed by drying in air. Chemical surface analysis was performed on a K-Alpha XPS (Thermo Fisher 1 Scientific, UK) using Al Kα X-rays, vacuum > 10^{-8} mbar and charge compensation during measurements. The survey and high-resolution spectra were recorded using a pass energy of 1.0 and 0.1 eV at a resolution of 1 and 0.1 eV, respectively. The binding energy was referenced to the C 1s peak at 284.8 eV. The data analysis was performed using the CASA XPS software.

Photocatalytic performance - The photocatalytic activities of the as-prepared $BiVO_4$ samples were evaluated for the photodegradation of methylene blue (MB), which was used as a model organic dye pollutant. In a typical experiment, 10 mg of the as-prepared sample were added to 20 mL of a 10 mg L^{-1} MB aqueous solution. These dispersions were stirred and exposed to visible-light radiation using six lamps (Osram, 15 W and maximum intensity at 440 nm) in a homemade photoreactor maintained at 18 °C. The details regarding the homemade photoreactor have already been published elsewhere.[78] The MB photodegradation was monitored based on its absorption maximum at 665 nm at regular time intervals using a UV-Vis spectrophotometer (Shimadzu – 1601PC) in absorbance mode. Prior to the experiment, the samples were maintained in contact with the MB dye solution for 12 h in the dark to achieve adsorption-desorption equilibrium. To comparative purposes, we performed photocatalytic experiments using the commercial V_2O_5 – the same reagent used as V source in the synthetic processes – and it had a negligible photocatalytic effect under visible-light irradiation, which is in agreement with observed results in our previous work.[131]

To verify the MB dye photo-oxidation and the probable formation of byproducts during the catalytic process were performed study using Mass Spectrometrer and Total Organic Carbon (TOC) analyses. MB dye solution was monitored in a positive ion mode using an Electrospray Ionization Mass Spectrometrer (ESI-MS, Varian 310-MS). The formed byproducts were analyzed by introducing aliquots into the ESI source with a syringe pump at a flow rate of 20 mL min^{-1}. The spectra were obtained after 2 min of equipment stabilization. The mineralization degree of MB dye photocatalyzed by *m*-$BiVO_4$/*t*-$BiVO_4$ heterostructure (V2-5-24 sample) was evaluated by measuring the decay of dissolved organic carbon using a total organic carbon (TOC) analyzer (Sievers InnovOx, GE Analytical Instruments).

Additionally, two different methods were employed to investigate the MB photodegradation mechanism driven by the $BiVO_4$ photocatalysts. The first method consisted of adding reactive species scavengers directly to the $BiVO_4$-containing MB solutions. In this procedure, dimethyl sulfoxide (DMSO), silver nitrate ($AgNO_3$) or sodium oxalate (SO) was added as a scavenger for $^{\bullet}OH$ radicals, conduction band (CB) electrons and valence band (VB) photogenerated-holes, respectively.[103] The second method consisted of indirectly detecting the amount of $^{\bullet}OH$ radicals based on the technique described by Ishibashi et al. (2002),[104,105] where an alkaline terephthalic acid (TA) solution instead of the MB solution was mixed with $BiVO_4$ in the photoreactor. TA

readily reacts with $^{\bullet}OH$ and forms a highly fluorescent product (i.e., 2-hydroxyterephthalic acid). This product has a fluorescence emission at approximately 425 nm, and its amount is proportional to the total amount of $^{\bullet}OH$ radicals formed during the photocatalytic process.[95] The concentration of TA was set to $5x10^{-4}$ mol L^{-1} in a dilute NaOH ($2x10^{-3}$ mol L^{-1}) solution.[95] At regular time intervals, aliquots of the suspension were collected and analyzed in a LS 50B fluorescence spectrometer (Perkin Elmer). The fluorescence emission spectra were obtained at an excitation wavelength of 315 nm.

4.4. - Results and discussion

Initially, the effects of the vanadium precursors and H_2O_2:M molar ratio (M is the sum moles of Bi and V) on the properties of the as-obtained materials were analyzed. The X-ray diffraction (XRD) patterns of the as-synthesized samples using different vanadium precursors and H_2O_2 concentrations are shown in FIGURE 4.1. The results indicate that the pure *m*-$BiVO_4$ crystalline phase [JCPDS n° 014-0688] was formed in all of the samples obtained from the NH_4VO_3 precursor (V1) regardless of the H_2O_2 concentration. When the as-synthesized samples were obtained using the V_2O_5 precursor (V2), the main product was also the *m*-$BiVO_4$ phase. However, when the molar ratio of H_2O_2:M (M = Bi + V) decreased to 5, a small amount of the tetragonal $BiVO_4$ crystalline phase was identified by the appearance of diffraction peaks at $2\theta \approx 24.5°$ and 32.7° (marked with *), which correspond to the (200) and (112) planes [JCPDS n° 014-133], respectively. Based on the tetragonal $BiVO_4$ phase ($\% = I_{tetragonal\ (200)}/(I_{monoclinic\ (121)} + I_{tetragonal\ (200)} + I_{orthorhombic\ (001)})$[85] from peaks intensities of XRD patterns), the V2-5 sample contains 75 and 19 wt.% of monoclinic and tetragonal $BiVO_4$, respectively. Additionally, the presence of a spurious orthorhombic V_2O_5 phase (~ 6 and 8 wt.%) was observed in the V2-5 and V2-10 samples, respectively, which was most likely due to some unreacted vanadium precursor that was identified based on the appearance of diffraction peaks at $2\theta \approx 20.3°$ corresponding to the (001) plane [JCPDS n° 01-076-1803].

These results reveal that the H_2O_2 concentration plays an important role in the synthesis of the tetragonal $BiVO_4$ phase, especially when V_2O_5 was used as the vanadium precursor. Nag et al. reported a similar effect, where the obtained TiO_2 crystalline phase depended on the H_2O_2:Ti ratio.[136] This result may be due to different solubilities of the precursors in water, where the solubility of the V_2O_5 precursor is almost

negligible. In this case, the solubility is dependent on the vanadium peroxo complex formation due to the presence of H_2O_2.

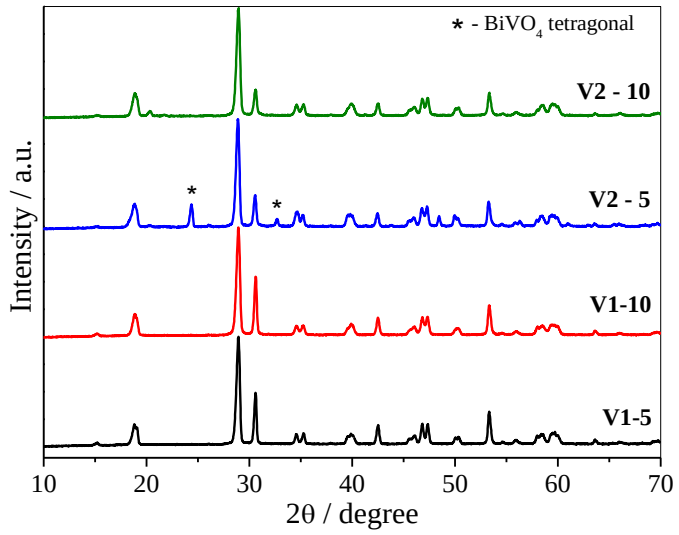

FIGURE 4.1 – XRD patterns of the as-synthesized $BiVO_4$ samples obtained using different precursors (V1=NH_4VO_3 and V2=V_2O_5) and H_2O_2 concentrations (5:1 and 10:1).

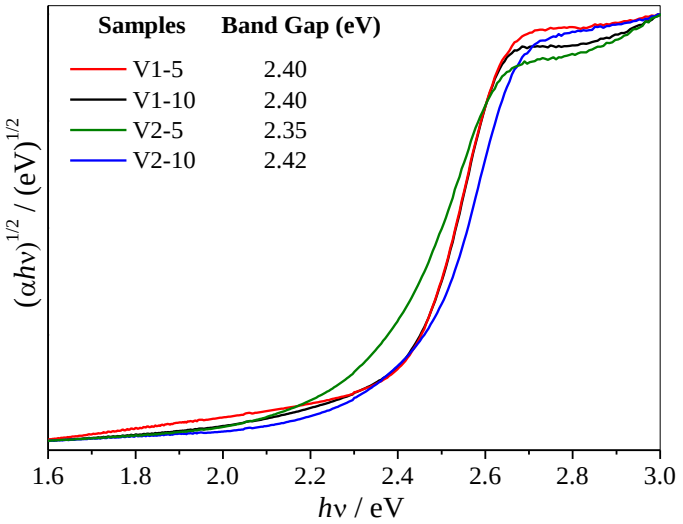

FIGURE 4.2 - Plot of $(\alpha h\nu)^{1/2}$ as a function of $h\nu$ from the UV-Vis DRS curve of the as-prepared $BiVO_4$ using different precursors (V1=NH_4VO_3 and V2=V_2O_5) and H_2O_2 concentrations (5:1 and 10:1). The band gap values obtained from the Tauc equation[107] are shown in the inset.

The optical properties of the materials were studied using UV-Vis diffuse reflectance spectroscopy (UV-Vis DRS). The band gap energy (E_g) for a direct band gap semiconductor can be determined from the plots of $(\alpha h\nu)^{1/2}$ as a function of $h\nu$ (FIGURE

4.2) originating from the Tauc equation.[107] The obtained band gap is very similar for all of the $BiVO_4$ samples and ranges from 2.35 to 2.42 eV. These results indicate that the different synthesis conditions did not lead to significant changes in the optical properties of these materials. As expected, these results also confirm that the photocatalysts can be activated by visible light.[61,137]

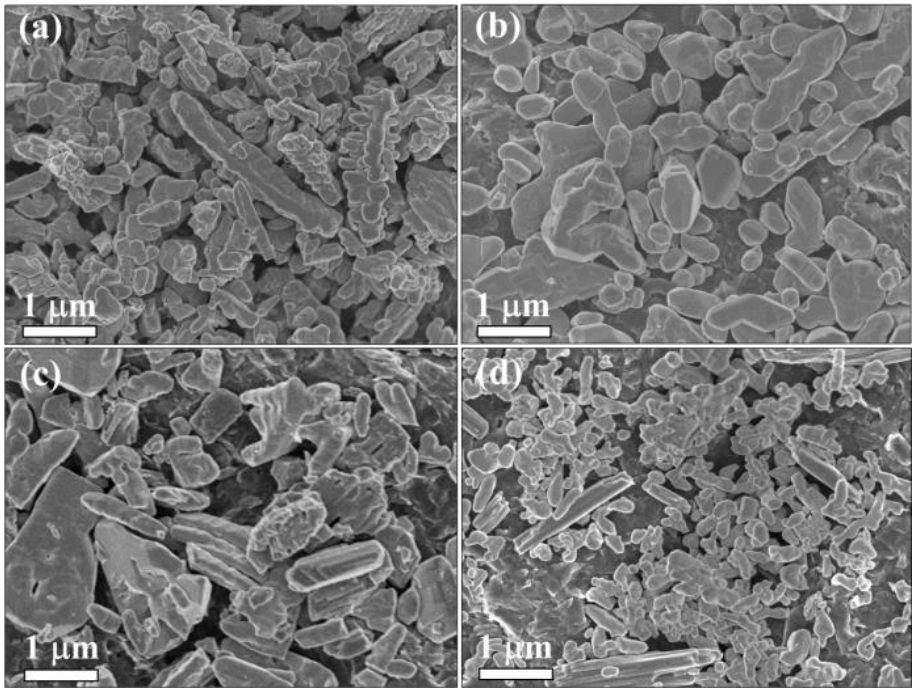

FIGURE 4.3 - Representative SEM images of the $BiVO_4$ samples obtained using different synthesis conditions: (a) V1-5, (b) V1-10, (c) V2-5, and (d) V2-10.

The morphology and size of the $BiVO_4$ particles obtained using different synthesis conditions were examined by scanning electron microscopy (SEM). As shown in FIGURE 4.3, all of the samples exhibited nanometer- and micrometer-sized particles in a range from 20 to 800 nm with sphere-like and worm-like shapes in large aggregates. However, the average particle size decreased, and the uniformity of size and shape increased (Figs. 3b and 3d) based on the H_2O_2 concentration for both cases (i.e., NH_4VO_3 and V_2O_5 precursors), which is most likely due to an increased vanadium peroxo complex formation that was induced by the increased H_2O_2 amount. This increased H_2O_2 amount controls the nucleation step and subsequent growth process. The role of the solubilization – reprecipitation processes during hydrothermal growth may be important. However, in this case, this aspect must be assumed to be an effect associated with the particle size after peroxo complex degradation because can assume that it is the first step in annealing. It is important to note that despite the phase compositions among the samples being different

(as shown in FIGURE 4.1) no specific morphologies are associated with the tetragonal phase, indicating that both phases are formed together. All of the materials exhibited very low surface areas (below 1 m^2 g^{-1}), as expected.[78]

The photocatalytic performance of the as-synthesized $BiVO_4$ using different precursors and H_2O_2 concentrations was investigated for the degradation of a MB dye solution under visible-light irradiation. Prior to the photocatalytic experiments, all of the materials were maintained in contact with the MB dye solution for 12 h in the absence of light to achieve adsorption-desorption equilibrium.

As shown in FIGURE 4.4, the blank test in the absence of the photocatalysts indicates that the photolysis contribution can be ignored. Concerning the MB adsorption effect, the as-synthesized samples exhibited low adsorption capacities, ranging from 2 to 15 %, as can be observed in the Appendix B (FIGURE B1). However, the V2-5 and V2-10 samples exhibited a higher MB adsorption capacity (ca. 10 and 15 %, respectively) than the V1-5 and V1-10 samples (ca. 2 and 4 %, respectively), indicating that the type of vanadium precursor (V_2O_5 or NH_4VO_3) can influence the physical and chemical properties that determine the adsorption potential. In fact, significant differences in one of the most important adsorption properties were observed, i.e., the surface charge of the particles measured by the zeta potential method at the natural pH of the MB solution (ca. 6.0) was highly positive (ca. +33 mV) for V1-10 and negative (ca. -24 mV) for V2-10, which imposes an electrostatic repulsion and attraction to cationic MB dye, respectively.[138] The negative charge of the nanostructures, which was obtained by the OPM method, was also similar to the results observed in a previous study.[131] As shown in TABLE B1, the degradation rate constants (k) of the $BiVO_4$ photocatalysts followed the order V1-5 ≈ V1-10 < V2-5 < V2-10. The samples synthesized using V_2O_5 (as precursor) exhibited better photoactivity than the other materials, which is most likely due to better interaction with the MB dye.

It is well known that the tetragonal $BiVO_4$ crystalline phase is less active than the monoclinic one.[25] The V2-5 sample exhibited a high activity despite containing 19 wt.% of the tetragonal phase. Therefore, the relatively high activity of the V2-5 sample is most likely related to the formation of *m*-$BiVO_4$/*t*-$BiVO_4$ heterojunctions because a simple physical mixture of both phases could exhibit a lower activity than pure *m*-$BiVO_4$. The formation of heterostructures between different phases of the same semiconductor is possible because the phases possess valence and conduction bands with suitable positions.[139–141] Titanium oxide (TiO_2 P25 - Degussa) is a classic example of a

heterostructured photocatalyst (i.e., an ideal mixed formed consisting of anatase and rutile phases), which has greater photoactivity than its isolated constituent phases.[141,142] Similarly, Ding et al. (2013) demonstrated that the relative positions of the valence and conduction bands and the Fermi energy levels of the monoclinic and tetragonal $BiVO_4$ phases are appropriated for the formation of one type-II heterostructure that is capable of promoting an effective separation of the photogenerated charges.[143] However, the ratio between the different phases in a heterostructure is a fundamental parameter that can be tuned to optimize its photocatalytic performance.

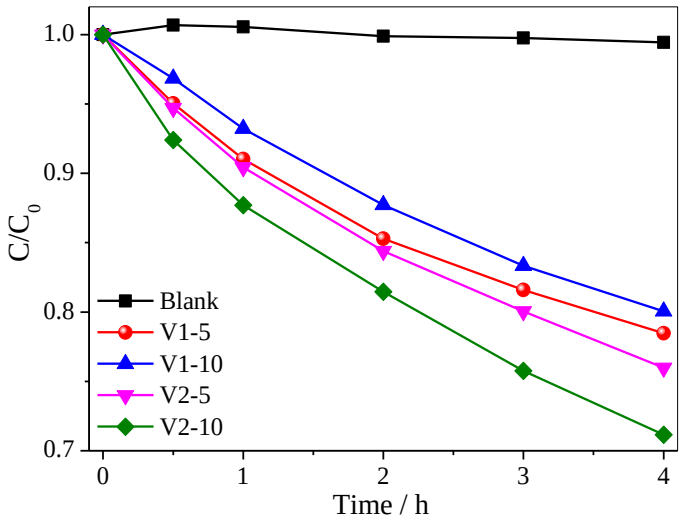

FIGURE 4.4 - Photodegradation of MB dye (10 mg L^{-1}) catalyzed by the $BiVO_4$ samples under visible irradiation.

As discussed above, the $BiVO_4$ samples that were prepared using V_2O_5 as a precursor exhibited higher adsorption and photoactivity for MB dye removal than the $BiVO_4$ samples prepared using the NH_4VO_3 precursor. The V2-5 sample contained mixed phases (i.e., *m*-$BiVO_4$/*t*-$BiVO_4$), and its higher photoactivity can be directly related to the formation of a type-II heterostructure between the constituent phases. The photocatalytic performance of heterostructures has been previously studied, and an appropriate amount of the mixed phases appears to be a key factor in the development of a photocatalyst with a higher performance.[12,67,83,91,144]

To optimize and evaluate the appropriate synthetic conditions for obtaining a heterostructure with better photocatalytic performance, the crystallization time was also evaluated. The time was increased from 12 to 24 h using both vanadium precursors (i.e., NH_4VO_3 and V_2O_5) with a fixed H_2O_2:M molar ratio equal to 5:1. To comparative purposes, the V2-10-24 sample was also synthesized, since the V2-10

sample showed a good photoactivity (FIGURE 4.4). The XRD patterns for these samples are shown in FIGURE 4.5. When the NH_4VO_3 precursor was employed (i.e., V1-5-24 sample), pure *m*-$BiVO_4$ was obtained. Therefore, the increase in the synthesis time did not cause significant structural changes compared to the synthesis being performed for 12 h under the same conditions (V1-5 sample). This result was also observed for the V2-10-24 sample, in which was obtained only $BiVO_4$ in monoclinic phase. However, when the V_2O_5 precursor was used with a fixed H_2O_2:M molar ratio equal to 5:1 (i.e., V2-5-24 sample), a DRX pattern corresponding to mixed phases consisting of monoclinic (~ 20 wt.%) and tetragonal (~ 75 wt.%) $BiVO_4$ crystalline phases were observed, and *t*-$BiVO_4$ appears to be the major crystalline phase. For the V2-5-24 sample, the presence of a spurious V_2O_5 phase (~ 5 wt.%) was also observed. According to the XRD results shown in FIGURES 4.1 and 4.5, the increase in the synthesis time led to a significant change in the ratio between the monoclinic and tetragonal phases (i.e., increase in the percentage of the *t*-$BiVO_4$ phase from 19 to 75 %).

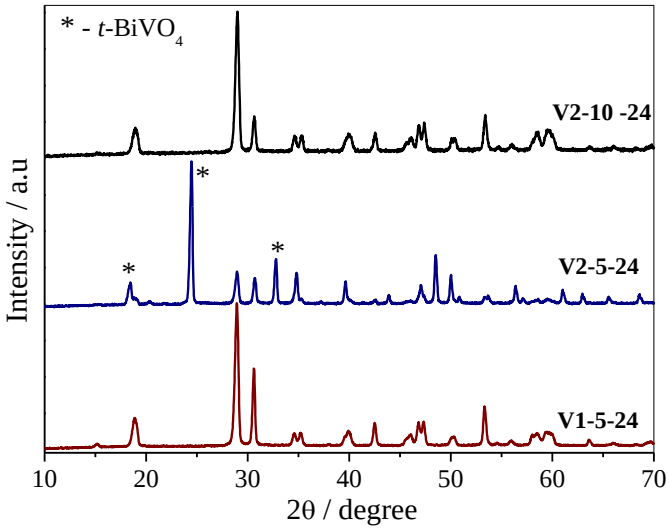

FIGURE 4.5 - Powder XRD patterns of the as-synthesized $BiVO_4$ samples.

The optical properties of the materials were investigated using UV-Vis DRS (FIGURE 4.6). The V1-5-24 sample exhibited a band gap value of 2.42 eV, which is similar to that of the V1-5 sample (inset on FIGURE 4.2). For the V2-5-24 sample, two band gaps were observed and are highlighted by dashed lines in Fig. 6. This result confirms the co-existence of two crystalline phases of $BiVO_4$. The band gap values were determined to be 2.35 and 2.61 eV, and these values are similar to those reported for the *m*- and *t*-$BiVO_4$ phases, respectively.[25]

Based on the SEM images, the V1-5-24 and V2-5-24 samples (FIGURE 4.7) exhibited morphologies that were similar to those of their corresponding samples treated for 12 h (i.e., the V1-5 and V2-5 samples, respectively). However, the increase in the hydrothermal treatment time led to a higher uniformity in the shape and size of the particles, and smaller particle sizes were obtained. The SSA data for both samples obtained using the BET model were 0.63 $m^2 g^{-1}$ and 0.26 $m^2 g^{-1}$ for the V1-5-24 and V2-5-24 samples, respectively. By considering the intrinsic error of the technique, these values can be assumed to be equal and not significant parameter for this material under these specific synthetic conditions.

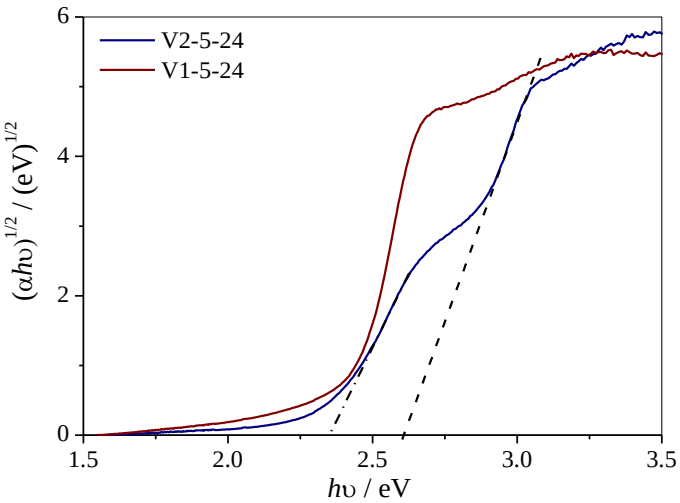

FIGURE 4.6 - Plots of $(\alpha h\upsilon)^{1/2}$ as a function of the photon energy ($h\upsilon$) obtained using the Tauc equation[107] from the DRS spectra for the V1-5-24 and V2-5-24 samples.

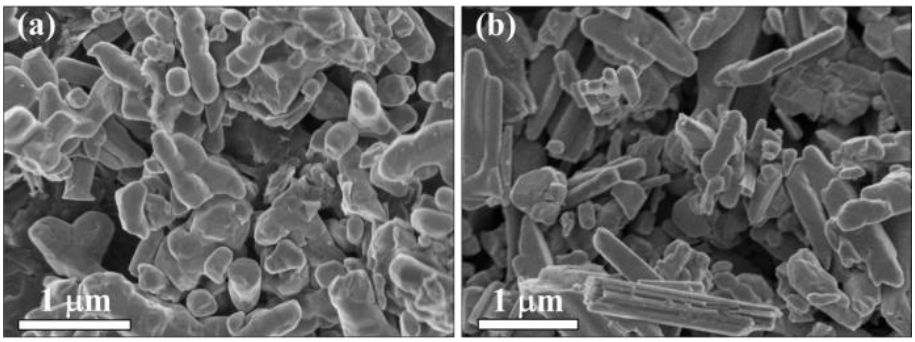

FIGURE 4.7 - Representative SEM images of the (a) V1-5-24 and (b) V2-5-24 samples.

TEM and HRTEM images of the V1-5-24 and V2-5-24 samples are shown in FIGURE 4.8. The V1-5-24 sample (FIGURE 4.8a and b) consists of agglomerates formed by a large number of well faceted $BiVO_4$ nanoparticles with size lower than 10 nm. This result is surprising because by SEM images analysis of the V1-5-24 sample

(FIGURE 4.7), it was observed only micrometric particles with smooth surface. Therefore, the SEM analysis for this kind of samples is not completely proper. HRTEM image of the V1-5-24 sample showed interlayer distance of 0.31 nm, which can be assigned to (121) plane of the monoclinic $BiVO_4$ phase. This result brings a new insight about the performance of the $BiVO_4$ photocatalysts, since the formation of heterostructures between the nanoparticles can be more effective than the formation with micrometric particles.

As shown in FIGURE 4.8c, the V2-5-24 sample exhibited similar morphological characteristics to that of the V1-5-24 sample, i.e. the presence of well faceted nanoparticles with size lower than 10 nm. Nevertheless, HRTEM image of this sample (FIGURE 4.8d) showed the coexistence in the same region of the nanoparticles of $BiVO_4$ in monoclinic and tetragonal phases, which were identified by their interlayer distances of 0.31 nm referent to (121) plane and 0.23 nm referent to (301) plane, respectively. This result is an indicative of the formation of heterojunctions between *m*-$BiVO_4$ and *t*-$BiVO_4$.

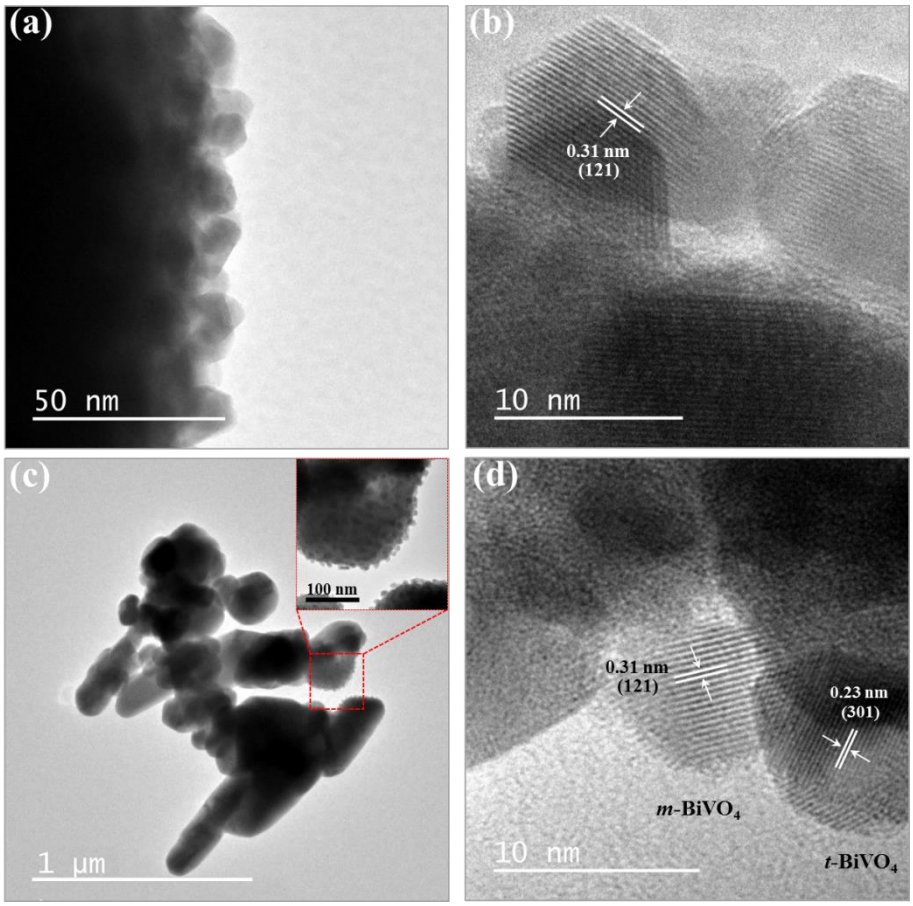

FIGURE 4.8 - TEM and HRTEM images of the (a-b) V1-5-24 and (c-d) V2-5-24 samples.

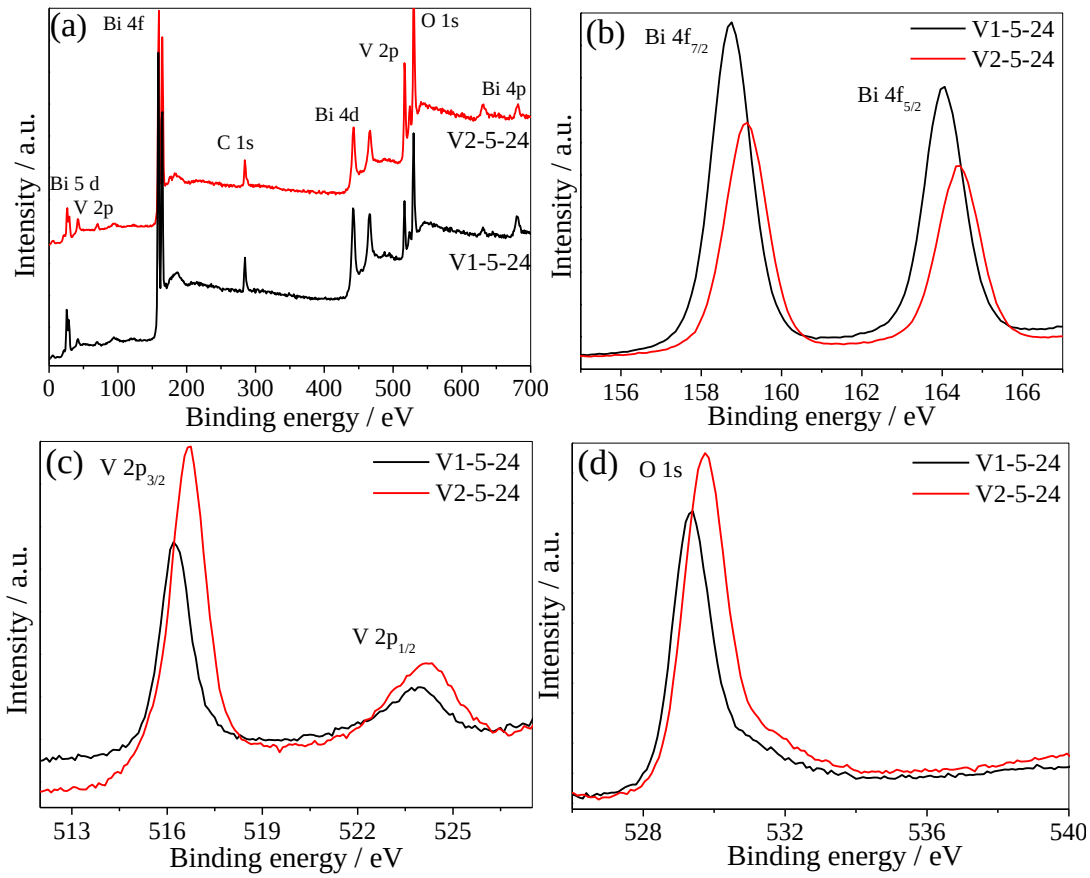

FIGURE 4.9 - X-ray photoelectron spectra of the V1-5-24 and V2-5-24 samples. (a) Survey spectra, (b) high-resolution spectra of Bi 4f, (c) high-resolution spectra of V 2p, and (d) high-resolution spectra of O 1s.

XPS analysis was performed to investigate the surface composition and chemical state of the elements of the V1-5-24 and V2-5-24 samples, and the results are shown in FIGURE 4.9. From the survey spectra (FIGURE 4.9a), the presence of Bi, V, O and C (this was used as an internal reference) were confirmed in both samples without any contamination. The XPS spectra contained the characteristic spin-orbit splitting of the Bi $4f_{5/2}$ and Bi $4f_{7/2}$ signals (Fig. 9b), V $2p_{1/2}$ and V $2p_{3/2}$ signals (FIGURE 4.9c), and O 1s peak (FIGURE 4.9d).[29,145,146] The binding energies of Bi 4f and V 2p and the difference between the low and high spin states are provided in TABLE B2. Slight shifts in the binding energies were observed among the $BiVO_4$ samples (FIGURE 4.9 and TABLE B2) because the V1-5-24 sample contains a pure *m*-$BiVO_4$ phase, whereas the V2-5-24 sample contains a mixture of *m*-$BiVO_4$ and *t*-$BiVO_4$ phases. The samples were expected to exhibit differences in their chemical environments due to the different crystal structures, which is in agreement with previous results.[29,59] It is important to note that the O 1s signal of the samples was a wide and slightly asymmetrical peak, indicating that

other oxygen species are present in the surface region, and these oxygen species might be hydroxyl oxygen and adsorbed oxygen on the surface of $BiVO_4$.[59]

The photocatalytic performance of the V1-5-24, V2-5-24 and V2-10-24 samples was probed by MB dye photodegradation under visible-light irradiation, and these results were compared to the results obtained using the V1-5 and V2-5 samples (FIGURE 4.10a and FIGURE B2a). For the samples obtained using the NH_4VO_3 precursor (V1-5 and V1-5-24), the synthesis time did not influence the adsorption or photocatalytic performance. Both samples exhibited an approximately 5 and 20 % MB removal for adsorption and photodegradation, respectively. It was also observed that the increase in hydrothermal treatment time to obtain the V2-10-24 sample did not cause any difference in its photoactivity when compared to V2-10 sample. However, for the samples V2-5 and V2-5-24, the synthesis time played a fundamental role in the preparation of photocatalysts with different phases compositions and different photocatalytic performances. The V2-5-24 sample exhibited a higher MB adsorption (approximately 45 %) and a higher catalytic activity (approximately 60 %) of MB photodegradation than the V2-5 sample, which exhibited an adsorption and photodegradation efficiency of 15 and 20 %, respectively. This trend was consistent with the results for the rate constant (k) analysis, where the V2-5-24 sample exhibited a rate constant for MB photodegradation 3.6 times higher than that observed for V2-5 (TABLE B3). The higher photoactivity of the V2-5-24 sample was unexpected because in this sample, tetragonal $BiVO_4$ is the major crystalline phase, which is less active than the *m*-$BiVO_4$ phase. The *m*-$BiVO_4$/*t*-$BiVO_4$ heterojunctions lead to the efficient separation of the electron/hole pair (i.e., an increase in lifetime of charge carriers). Therefore, this result is surprising because it is expected that an efficient heterojunction formed by this system was composed of *m*-$BiVO_4$ as the major crystalline phase.[81] This result indicates that the *t*-$BiVO_4$ crystalline phase in the V2-5-24 sample was more photoactive. The origin of great increase in the adsorption capacity of the V2-5-24 sample (FIGURE B2a) can be related to its higher content of tetragonal phase, since Zhang and co-authors (2012) have been stablished that $BiVO_4$ in tetragonal phase shows a higher affinity to MB dye than the monoclinic one.[147]

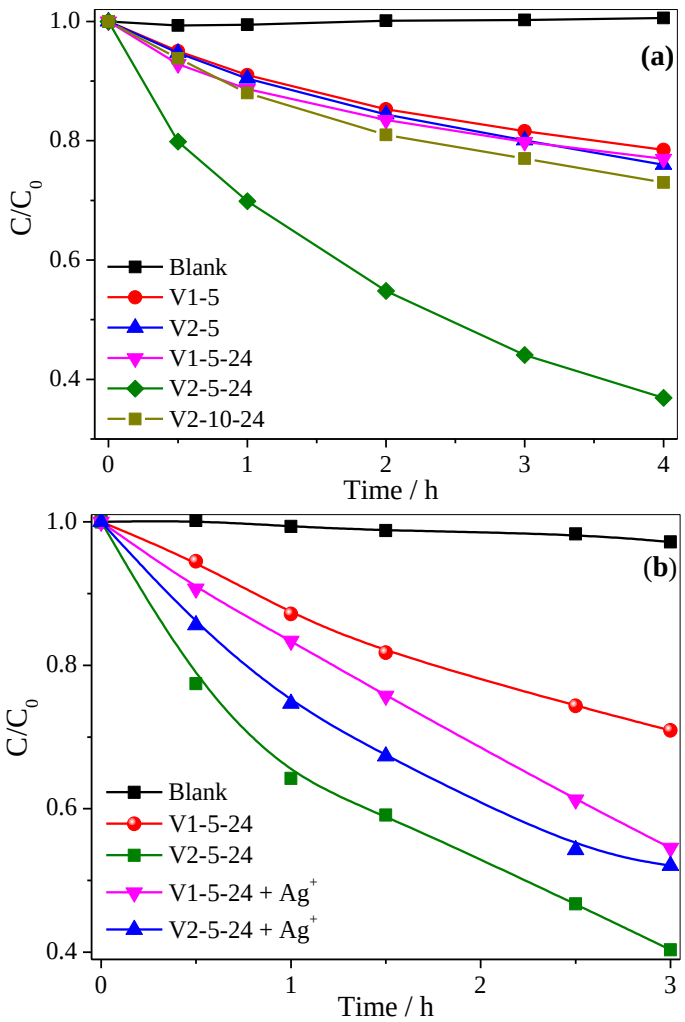

FIGURE 4.10 - (a) MB dye photodegradation catalyzed by the as-synthesized samples as a function of time under visible light irradiation. (b) Photodegradation kinetics of MB catalyzed by the V1-5-24 and V2-5-24 samples with and without Ag^+ ($AgNO_3$, 20 mmol L^{-1}).

Despite the fact that our results indicate that the *m*-$BiVO_4$/*t*-$BiVO_4$ heterojunctions are the main reason for the higher photoactivity of the V2-5 and V2-5-24 samples, an investigation of the influence of the heterojunctions on the photocatalytic performance was performed because the formation of a heterojunction can reduce the recombination rate of electron/hole pairs, which can increase the photocatalytic activity.[2,148] An analysis of the increase in the photoactivity associated with electron acceptors indirectly indicates the recombination rate of the structure. A good sacrificial reagent to use as an electron acceptor is Ag^+ (Ag^+/Ag 0.799 V vs NHE) because this ion can be spontaneously reduced at a high reduction potential.[64,149] Therefore, MB dye photodegradation tests in the presence or absence of Ag^+ ions were carried out (FIGURE

4.10b). To quantitatively evaluate the influence of photogenerated electrons, a first-order kinetic model of the photodegradation data was applied (FIGURE B2b), and the kinetic constants (*k*) for the reaction are shown in TABLE 4.1. For the V1-5-24 sample, the addition of Ag^+ in the photocatalytic tests increased the MB degradation efficiency. The degradation percentage increased from 29 to 46 % with the addition of Ag^+, and the *k* value for the process containing Ag^+ was 1.7 times higher than that of the process performed in the absence of Ag^+. Therefore, the effect of the electron acceptor (Ag^+) increased the electron/hole pair lifetime, which significantly increased the efficiency of the photocatalytic process for the samples containing the *m*-$BiVO_4$ pure phase, as observed in our previous study.[121]

A different effect was observed for the V2-5-24 sample compared to the V1-5-24 sample, where the addition of Ag^+ in the photocatalytic tests decreased the photoactivity of the sample. The rate constant of MB photodegradation for the V2-5-24 sample with Ag^+ was approximately 1.3 times lower than that in the absence of Ag^+. This result indirectly indicates that an efficient heterojunction was formed between the monoclinic and tetragonal $BiVO_4$ phases because Ag^+ did not increase the efficiency of the photodegradation process. However, the decrease in the photoactivity of the V2-5-24 sample in the presence of Ag^+ is related to the adsorption of Ag metal in actives sites liable for the adsorption of MB dye, which were created during visible-light irradiation leading to Ag^+ reduction.[150]

TABLE 4.1 - First-order rate constants for the MB photodegradation tests performed under visible irradiation in the presence and absence of a sacrificial reagent (Ag^+).

Sample	***k* x 100 (h^{-1})**	**k_{Ag} x 100 (h^{-1})***
V1-5-24	9.8	17.0
V2-5-24	23.9	18.7

*k_{Ag} is the rate constants for reaction in the presence of Ag^+

Additionally, the formation and effect of the *m*-$BiVO_4$/*t*-$BiVO_4$ heterojunctions in the V2-5-24 sample were studied by analyzing the photocatalytic performance of a physical mixture (PM) prepared by mixing 75 wt.% of *t*-$BiVO_4$, 20 wt.% of *m*-$BiVO_4$ and 5 wt.% of V_2O_5 (FIGURE B3). The *t*-$BiVO_4$ samples, which were employed as reference compounds, were prepared using the hydrothermal method reported by Guo et al. (2010).[29] In summary, the photocatalytic performances of the as-prepared samples were in the following order: V2-5-24 (*m*-$BiVO_4$/*t*-$BiVO_4$) > *m*-$BiVO_4$ >

PM > *t*-$BiVO_4$ (FIGURE B3). Interestingly, the PM sample exhibited a lower photoactivity than the V2-5-24 sample. Therefore, these results confirm that V2-5-24 is not a physical mixture, rather than contains junctions between the constituent phases that result in a higher photoactivity due to the increased in the lifetime of electron/hole pairs. In addition, the PM sample exhibited an intermediate photoactivity that was between *m*-$BiVO_4$ and *t*-$BiVO_4$, indicating that its photoactivity is only a linear combination the photoactivity of the isolated phases.

To elucidate the photo-oxidation of MB dye, it was performed the analysis of the MB solution before and after photocatalytic the experiments catalyzed by *m*-$BiVO_4$/*t*-$BiVO_4$ heterostructure using mass spectrometry (ESI-MS), depicted in FIGURE 4.11. The ESI-MS spectrum obtained without photocatalyst exhibited only a strong signal of mass/charge (*m/z*) ratio at 284, which is assigned to MB structure without any oxidation. After irradiation of the MB solution (catalyzed by *m*-$BiVO_4$/*t*-$BiVO_4$ heterostructure), mass spectrum revealed several peaks with *m/z* equal to 332, 301, 284, 270, 256, 243 and 129. The signals at *m/z* = 301 and 332 regard to one and three hydroxylation in the aromatic ring of MB, respectively.[151–154] The process of MB hydroxylation confirms that $^{\bullet}OH$ radical played an important role for MB photodegradation. The signals of *m/z* = 270, 256 and 243 are referent to cleavage of one or more methyl groups substituent on the amine groups of MB and these species are azure B, azure A and azure C, respectively.[155] The signal of *m/z* = 129 is referent to cleavage of ring aromatic due to attack of species actives photogenerated in the presence of *m*-$BiVO_4$/*t*-$BiVO_4$ heterostructure.[151–154]

Further, to confirm the efficiency of V2-5-24 sample to reduce the dissolved organic carbon in MB dye solution, its content was measured by TOC analyzer after 3 h under visible irradiation. Was observed that MB dye was 65% mineralized to CO_2 and H_2O by V2-5-24 sample. This result evidences that the photocatalytic process proposed in this study was effective not only for the color removal, but also to reduce the organic content of the MB dye solution.

The stability of the catalyst is a fundamental property for its practical application for several catalytic cycles without loss in its efficiency. Therefore, the photostability of the *m*-$BiVO_4$/*t*-$BiVO_4$ heterostructure was evaluated by performing recycling experiments for five times under the same conditions used in the MB dye photodegradation tests. After each reaction cycle, the sample was separated from the MB solution by centrifugation, and placed immediately in contact with a freshly prepared MB

solution. As shown in FIGURE B4, the photocatalytic performance of *m*-$BiVO_4$/*t*-$BiVO_4$ heterostructure was kept even after four cycles, exhibiting only a slight decrease after fourth cycle.

Despite the interesting and promising photocatalytic performance of the studied materials, a deeper analysis is required to elucidate the mechanism involved in the photocatalytic process. To evaluate the mechanism of MB photodegradation driven by the as-synthesized photocatalysts and the importance of pollutant degradation due to the formation of active radical species, such as $^{\bullet}OH$ and $O_2^{\bullet-}$, the $^{\bullet}OH$ radicals was detected using a method proposed by Ishibashi et. al. (2000)[104,156] and discussed in detail by our group.[12,95]

The rate constant formation of the $^{\bullet}OH$ radicals is shown in TABLE 4.2 and FIGURE B5. The efficiency of $^{\bullet}OH$ radical formation can be represented by the k_{OH} values listed in TABLE 4.2. The observed trend in the photoactivity of the samples obtained using the NH_4VO_3 precursor (V1-5, V1-10 and V1-5-24) for MB dye degradation was the same as that observed for $^{\bullet}OH$ radical formation (i.e., V1-5 ≈ V1-10 < V1-5-24), which indicates that an indirect mechanism plays a key role in the photoactivity. The trend of k and k_{OH} observed to reaction catalyzed by the V1 samples can be better analysed in FIGURE B6a. In fact, the pollutant photodegradation via an indirect mechanism (i.e., attack by $^{\bullet}OH$ radical) catalyzed by the *m*-$BiVO_4$ phase has been previously observed by our group.[121] However, the observed trend for the efficiency of $^{\bullet}OH$ radical formation over the samples obtained using the V_2O_5 precursor (V2-5, V2-10, V2-5-24) was different when compared to their photoactivity for MB dye photodegradation. The order observed in the photoactivity was as follows: V2-5 ≤ V2-10 < V2-5-24. However, the efficiency of $^{\bullet}OH$ radical formation was as follows: V2-5 ≤ V2-5-24 < V2-10. The relationship between k and k_{OH} to reaction catalysed by the V2 samples can be better analysed in FIGURE B6b. These results indicate that the V2-10 sample led the MB dye photodegradation primarily via an indirect mechanism (i.e., the $^{\bullet}OH$ radical was the major active species in the process catalyzed by V2-10). The V2-10 sample exhibited a k_{OH} value that was 1.8 times higher than that of the V2-5-24 sample, and for the rate constant of MB photodegradation, the V2-5-24 sample exhibited a k value that was 3.3 times higher than that of V2-10. Therefore, despite the V2-5 and V2-5-24 samples (heterojunctions) producing $^{\bullet}OH$ radicals, the indirect mechanism was not the main mechanism in MB dye degradation for these samples.

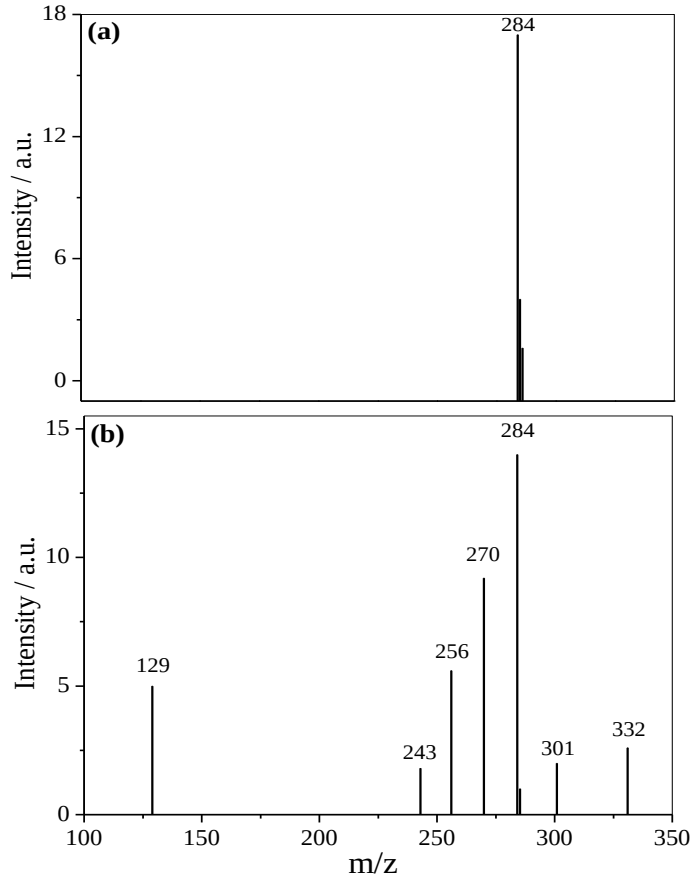

FIGURE 4.11 - ESI mass spectra of (a) MB dye pure and (b) catalyzed by the V2-5-24 sample after 3h under visible irradiation.

TABLE 4.2 - Rate constant of $^{\bullet}OH$ radical formation by the $BiVO_4$ as-synthesized samples. The *k* values from Tables S1 and S3 are reproduced to facilitate comparison.

Sample	***k***	k_{OH}
V1-5	5.9	19.6
V1-10	5.6	20.5
V2-5	6.6	44.7
V2-10	7.4	97.4
V1-5-24	6.1	32.3
V2-5-24	24.2	55.6

Additionally, to understand the photocatalytic mechanism of the reaction catalyzed by *m*-$BiVO_4$/*t*-$BiVO_4$ (V2-5-24), we evaluated the effects of the addition of three different reactive scavenger species (i.e., Ag^+ (strong oxidant, CB electrons acceptor), DMSO (a $^{\bullet}OH$ scavenger) and sodium oxalate (SO, a VB holes photogenerated scavenger)) to the MB solution during the photocatalysis experiments.[24,103,117] Dissolved oxygen is considered to be a photogenerated electron scavenger that inhibits fast charge carrier recombination, resulting in the formation of a superoxide radical ($O_2^{-\bullet}$), which is

important for some photodegradation processes.[117] Therefore, a rational approach for evaluating the importance of $O_2^{-\bullet}$ is to scavenge it with Ag^+ (previously shown in FIGURE 4.10b).[24,103] Therefore, if the photodegradation process is driven by $O_2^{-\bullet}$ radicals, the reaction rate should be substantially less with the addition of Ag^+. However, if the $^\bullet$OH radical or a direct degradation mechanism (i.e., pollutants are directly attack by VB holes) plays a major role in the photodegradation process, the reaction rate should decrease in the presence of excess DMSO and/or SO, respectively.[24,103,118]

As shown in FIGURE 4.12 and FIGURE B7, the addition of excess SO (10 mol L^{-1}) significantly inhibited the photodegradation percentage of MB dye compared to that with no scavenger under the same conditions from 59 to 34 %. The rate constant decreased by approximately 50 % (FIGURE B7), indicating that the VB photogenerated holes and/or $^\bullet$OH active species play a crucial role in the MB photooxidation process. To separate the effects of $^\bullet$OH and the VB photogenerated holes, DMSO was employed as a selective scavenger for $^\bullet$OH. Excess DMSO in the MB solution capture all of the $^\bullet$OH radicals produced during the photocatalytic process.[118] As shown in FIGURE 4.12, the use of excess DMSO resulted in slight decrease in the photodegradation percentage from 54 to 45 % after 2.5 h of exposure to visible light (the rate constant decreased by 25 %, FIGURE B7). Therefore, the direct mechanism plays a more important role than the indirect mechanism in the MB dye photodegradation process catalyzed by the V2-5-24 sample even though both mechanisms have a significant role. This result is in agreement with the result obtained for $^\bullet$OH radical formation via the terephthalic acid method.

As previously shown in FIGURE 4.10b and 12, excess of Ag^+ in the MB solution resulted in a decrease in the photodegradation percentage from approximately 60 to 48 % after 3 h of exposure to visible light (the rate constant decreased by 22 %). Therefore, in contrast to pure *m*-$BiVO_4$, the *m*-$BiVO_4$/*t*-$BiVO_4$ heterostructured sample has a conduction band edge with a sufficiently high potential or lifetime of photogenerated electron to reduce the dissolved oxygen. Therefore, the superoxide radical ($O_2^{-\bullet}$) plays also an important role in the MB photodegradation mechanism catalyzed by the *m*-$BiVO_4$/*t*-$BiVO_4$ heterostructure sample.

To understand the photodegradation mechanism and charge transfer between the phases contained in the V2-5-24 heterostructure sample, the valence band (VB) was determined using XPS and compared to that of V1-5-24 (FIGURE B8). The spectrum thresholds of the V1-5-24 and V2-5-24 samples are 1.2 and 2.0 eV,

respectively. The value of VB top in V1-5-24 was consistent with that of the *m*-$BiVO_4$ phase, as previously reported.[59] The *t*-$BiVO_4$ phase has a less positive VB top (0.9 eV) than the *m*-$BiVO_4$ phase (1.1 eV), as reported by Li et. al. (2012).[59] Therefore, the V2-5-24 sample exhibited a VB top value that was much higher than expected compared to those of the *m*- and/or *t*-$BiVO_4$ phases, indicating that a heterojunction forms between the phases resulting in a shift in the VB top of both phases.

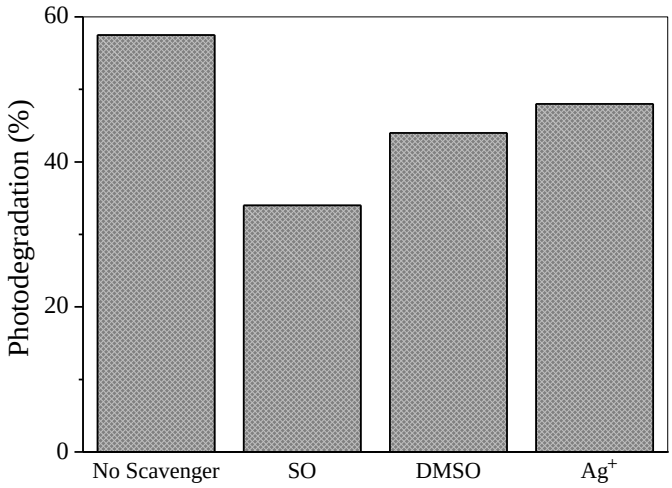

FIGURE 4.12 - MB dye photodegradation percentage catalyzed by the V2-5-24 sample with different scavengers during 2.5 h of visible-light irradiation.

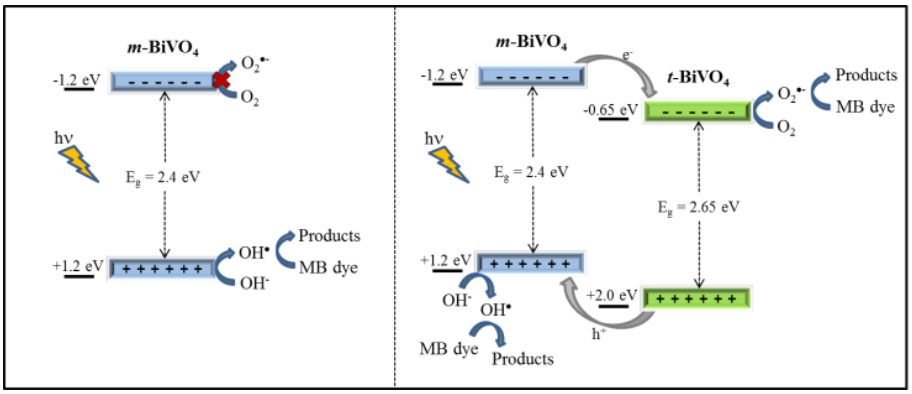

FIGURE 4.13 – (a) MB dye photodegradation catalyzed by the as-synthesized samples as a function of time under visible light irradiation. (b) Photodegradation kinetics of MB

In summary, according to our results, the mechanism for the photodegradation of organic pollutants on the surface of the pure *m*-$BiVO_4$ photocatalyst occurs primarily via an indirect mechanism (i.e., $^{\bullet}OH$ radical generation and attack). However, the *m*-$BiVO_4$/*t*-$BiVO_4$ heterostructure led the photodegradation of pollutants via direct and indirect mechanisms (i.e., by the formation and attack of $^{\bullet}OH$ and $O_2^{-\bullet}$ radicals and direct VB hole oxidation). Therefore, the great increase in *m*-$BiVO_4$/*t*-$BiVO_4$

heterostructure photoactivity can be related to its ability to activate three different photodegradation paths. The main photodegradation mechanism of *m*-$BiVO_4$ is compared to the mechanism and charge transfer of the enhanced photocatalytic performance of the *m*-$BiVO_4$/*t*-$BiVO_4$ heterostructure in FIGURE 4.13.

4.5. - Conclusions

In summary, the formation of heterostructures between different phases of the same semiconductor provides a viable alternative for improving the photocatalytic performance. Using the proposed synthesis method, a pure *m*-$BiVO_4$ phase as well as *m*-$BiVO_4$/*t*-$BiVO_4$ heterostructures were prepared by controlling the synthesis parameters. The heterostructured samples are composed of nanoparticles of *m*-$BiVO_4$ and *t*-$BiVO_4$ with size lower than 10 nm, and the probable interface between them was also observed. Samples that contain the *m*-$BiVO_4$ and *t*-$BiVO_4$ phases exhibited better photocatalytic performance for MB degradation under visible-light irradiation than that of the isolated phases. The *m*-$BiVO_4$/*t*-$BiVO_4$ heterostructure showed no significant deactivation even after four successive re-uses for MB photodegradation. Oxidation mechanism of the MB dye was elucidated by mass spectroscopy and. The photoactivity enhancement in the *m*-$BiVO_4$/*t*-$BiVO_4$ sample was due to the formation of a suitable heterojunction between the $BiVO_4$ phases, promoting the effective separation of photogenerated charges. The experiments using active scavenger species and the VB top analysis based on XPS indicated the formation of a type-II heterostructure where the increase in the charge carrier lifetime enabled the formation of active species. In addition, holes (h^+), superoxide anion radicals ($O_2^{-\bullet}$) and hydroxyl radicals ($^{\bullet}OH$) were the primary active species responsible for MB photodegradation.

5. - Chapter III: How to obtain $Bi_2O_3/BiVO_4$ heterostructures effectively?

The content of this chapter is an adaptation of the manuscript entitled **"Growth of $BiVO_4$ nanoparticles on a Bi_2O_3 surface: effect of heterojunction formation on catalytic performance driven by visible irradiation"** by Osmando F. Lopes, Kele T. G. Carvalho, Waldir Avansi Jr and Caue Ribeiro that is under preparation.

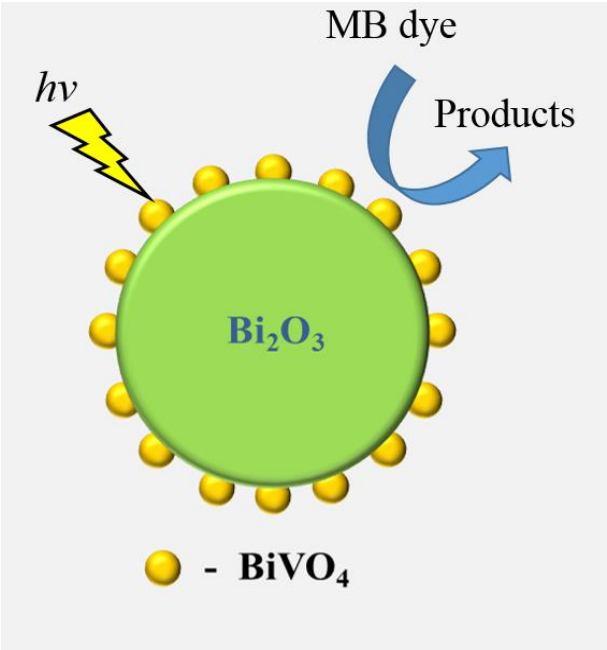

5.1. - Abstract

The formation of heterostructures between different semiconductors is an interesting way to decrease rapid charge carrier recombination in photocatalysts, but the development of efficient synthesis methods for this purpose remains a challenge. This work describes a novel strategy for tailoring heterostructures, based on the difference in solubility of two semiconductors that possess at least one metal in common. The growth of $BiVO_4$ on a preformed Bi_2O_3 particle was used as a model for the formation of heterojunctions. The quantity of $Bi_2O_3/BiVO_4$ heterojunctions was tuned using synthesis variables (temperature and V concentration) and the particle size of preformed Bi_2O_3. The synthesis of $Bi_2O_3/BiVO_4$ heterostructures using nanoparticles of Bi_2O_3 resulted in a greater quantity of heterojunctions, due to higher solubility of the nanoparticles, compared to micrometric Bi_2O_3, leading to a classical heterogeneous precipitation over the preformed surfaces. The proposed growth mechanism was effective in obtaining heterostructured $Bi_2O_3/BiVO_4$ semiconductors that presented enhanced photocatalytic performance, compared to the isolated phases. The greater photoactivity of the as-synthesized heterostructures could be explained by increased spatial separation of the photogenerated electron/hole pair, due to the formation of a type-II heterostructure, as observed by time-resolved photoluminescence (TRPL) analysis. In this case, the photogenerated electrons were transferred from the conduction band of the *p*-type semiconductor (Bi_2O_3) to the *n*-type ($BiVO_4$) semiconductor, while photogenerated holes were transferred from the valence band of the *n*-type semiconductor to the *p*-type semiconductor.

5.2. - Introduction

The formation of heterostructures between semiconductors has been widely studied for applications in heterogeneous photocatalysis such as organic pollutant degradation,[12,67,91,157] water splitting,[158–160] and artificial photosynthesis [161–164]. A special feature of a suitable heterostructure is the capacity to increase the lifetime of the photogenerated electron/hole pair by suppressing its recombination. As a result, the charges migrate to the semiconductor surface, increasing the occurrence of redox reactions over the heterostructure surface.[37–43] In addition, the system formed between the $BiVO_4$ (type *n*)[25,78] and Bi_2O_3 (type *p*) semiconductors[79,80] exhibits promising electronic properties for the creation of type-II heterostructures (with *p*-*n* junctions).[48] Due to its band gap characteristics, this heterostructure can be activated by visible

radiation, which is an important feature for photocatalytic applications under natural sunlight.[25,58,78]

Heterostructured $Bi_2O_3/BiVO_4$ has been studied due to its potential for use in photocatalytic degradation of organic pollutants[92,98] and for water splitting in photoelectrochemical (PEC) cells.[97] However, the formation of efficient heterojunctions between these two semiconductors remains a challenge. Recently, Ye et al.[97] proposed a synthesis method for building heterostructured $Bi_2O_3/BiVO_4$ films with a remarkable photocurrent in PEC cells. However, this method is based on multiple steps, which favors the formation of a spurious phase (V_2O_5). Cheng et al.[98] reported an interesting method for obtaining $BiVO_4/Bi_2O_3$ composites using a mild one-step hydrothermal process, but the ratio between Bi_2O_3 and $BiVO_4$ could not be controlled. The main challenge to be overcome is the difficulty in controlling the simultaneous crystallization of two different components with suitable physical, chemical, and electronic properties.[37]

The use of a preformed particle to build up heterostructures is of interest because the morphology and creation of interfaces can be easily controlled. Since Bi_2O_3 and $BiVO_4$ have Bi in common, it is possible create an interface between the semiconductors by growing one phase on the sacrificial surface of a preformed particle, driven by the difference in solubility of the compounds. Therefore, the aim of this study was to develop a novel and efficient synthesis method to obtain $Bi_2O_3/BiVO_4$ heterostructures, based on a hydrothermal treatment, and to evaluate the influence of the heterojunction on photocatalytic performance. Investigation was made of the effect of the particle size (micrometric or nanometric) of the preformed Bi_2O_3, as well as the hydrothermal treatment temperature, on the amount of $BiVO_4$ grown on the Bi_2O_3 surface. The photoactivity of the heterostructures was probed using the photodegradation of methylene blue dye (MB) under visible irradiation. A mechanism is proposed for the effect of charge transfer in increasing the charge carrier lifetime of the type-II $Bi_2O_3/BiVO_4$ heterostructure formed.

5.3. - Experimental

Synthesis of $Bi_2O_3/BiVO_4$ Heterostructures - The synthesis of heterostructured $Bi_2O_3/BiVO_4$ samples was performed by dispersing 0.2 g of either micrometric (Sigma-Vetec, 98%) or nanometric (Sigma-Aldrich, 90-210 nm particle size, 99.8%) preformed Bi_2O_3 precursor in 30 mL of distilled water, followed by the addition of NH_4VO_3 precursor in different Bi:V molar ratios (1:1 or 1:2). The resulting reaction

mixture was hydrothermally treated at 150 or 200 °C for 12 h. The materials obtained were washed with distilled water and centrifuged three times to remove impurities, and then dried in an oven at 50 °C. FIGURE 5.1 shows a proposal for the growth of $BiVO_4$ particles on the Bi_2O_3 sacrificial surface, driven by the solubility difference between them. For comparative purposes, pure $BiVO_4$ was synthesized using a method similar to that described above, with $Bi(NO_3)_3.5H_2O$ and NH_4VO_3 added to 30 mL of distilled water at a Bi:V molar ratio of 1:1, followed by hydrothermal treatment of this mixture at 150 °C for 12 h.

The heterostructured samples are referred to as *s*-Het-x:y T, where *s* is the size scale of the Bi precursor (*m* for micrometric and *n* for nanometric), x:y is the Bi:V molar ratio, and T is the crystallization temperature.

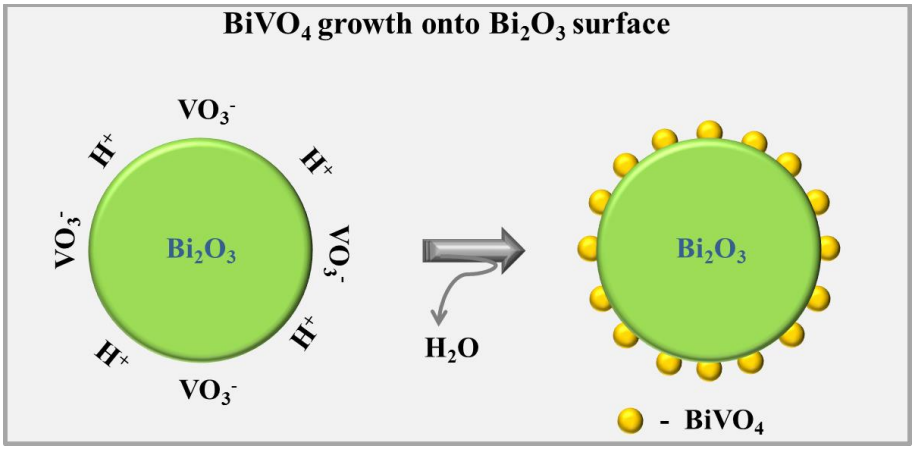

FIGURE 5.1 - Proposed growth of $BiVO_4$ on a Bi_2O_3 surface.

<u>*Powder characterization*</u> - X-ray diffraction (XRD) patterns were recorded using a Shimadzu XRD 6000 diffractometer with Ni-filtered Cu kα (λ = 0.15406 nm) radiation. The instrument was operated at 30 kV and 30 mA, in continuous scanning mode at a speed of 2° min^{-1} and with a step width of 0.02°, from 10 to 60° 2θ. Raman spectroscopy measurements were performed using a FT-Raman spectrometer (Bruker RAM II with a Ge detector) equipped with a Nd:YAG laser with a wavelength centered at 1064 nm. UV-Vis diffuse reflectance spectra were recorded from 200 to 800 nm, using a UV-Vis spectrophotometer (Shimadzu UV-2600) equipped with an integrating sphere (ISR-2600 Plus), in order to determine the band gap of the materials. The measurements were performed in total reflection mode, employing barium sulfate ($BaSO_4$) as a standard compound. The specific surface area (SSA) of the samples was calculated according to the BET model, using the N_2 adsorption data obtained at -196 °C (Micrometrics ASAP

2000 instrument). All the samples were pre-treated (degasified) by heating at 80 °C under vacuum until reaching a degassing pressure of less than 20 μm Hg.

The morphology and size of the particles were investigated using field emission gun scanning electron microscopy (FE-SEM) (JEOL JSM 6701F). Semi-quantitative atomic composition analysis and elemental mapping of Bi and V atoms were performed by energy-dispersive X-ray spectroscopy (EDS), using a Thermo Noran device coupled to a scanning electron microscope (JEOL JEM 2010). The formation of heterostructures was confirmed by high resolution transmission electron microscopy (HRTEM), using a TECNAI G2 F20–LaB6 instrument operated at 200 kV. The samples were prepared for TEM by wetting carbon-coated copper grids with a drop of the colloidal alcoholic suspensions and then drying in air.

Photocatalytic Performance and photodegradation mechanism evaluation - The photocatalytic activities of the as-prepared samples were evaluated using the photodegradation of methylene blue (MB). In a typical experiment, 10 mg of the photocatalyst was added to 20 mL of a 10 $mg.L^{-1}$ MB aqueous solution. The dispersions were stirred and exposed to visible irradiation using six lamps (Osram, 15 W, maximum intensity at 440 nm) in a homemade photoreactor maintained at 18 °C. The photodegradation of MB was monitored at regular time intervals by UV-Vis spectrophotometry (1601PC, Shimadzu), using the absorbance maximum at 665 nm. Prior to irradiation, the suspensions were maintained for 12 h in the dark, under magnetic stirring, to achieve adsorption-desorption equilibrium.

The lifetimes of the charge carriers of the as-synthesized samples were determined by time-resolved photoluminescence, using time-correlated single photon counting (TCSPC). A 405 nm pulsed laser diode (LDH P-C-405, PicoQuant) with an approximate 50 ps pulse width and 40 MHz repetition rate was used as the excitation source. The PL emission was spectrally resolved using collection optics and an emission monochromator. The TCSPC module (PicoHarp 300, PicoQuant) was used for ultrafast detection. The deconvolution of the PL decay was performed using fitting software (FluoFit, PicoQuant) to deduce the time constant associated with exponential decay.

5.4. - Results and discussion

XRD patterns of as-synthesized samples (FIGURE 5.2) were obtained to confirm the presence of both $BiVO_4$ and Bi_2O_3 crystalline phases and estimate the weight

ratio between them. The hydrothermal treatment of *m*-Bi_2O_3 in the presence of the V precursor leads to mixed crystalline phases between the monoclinic Bi_2O_3 (JCPDS, n° 41-1449) and monoclinic $BiVO_4$ (JCPDS, n° 83-1699). The weight percentage of $BiVO_4$ in each heterostructured sample was calculated using the relative intensities of their main peaks (($\% = I_{BiVO4\,(121)}/(I_{Bi2O3\,(120)} + I_{BiVO4\,(121)})$),[85] identified in FIGURE 5.2a and TABLE 5.1. It can be seen that increases of the concentration of the V precursor and the hydrothermal treatment temperature (except for the *m*-Het-1:2 200 °C sample) resulted in greater amounts of monoclinic $BiVO_4$ formed on the as-synthesized samples. The *m*-Het-1:2 200 °C sample showed different behavior, with formation of a third spurious phase (probably $V_2O_5.nH_2O$, indicated by the peaks at $2\theta \approx 11.4$ and 11.6), due to the excess of unreacted V precursor together with a condition that provided suitable thermal energy for the crystallization of vanadium compounds.[106,131]

The effect of Bi_2O_3 precursor particle size on heterostructure synthesis was evaluated using the nanometric Bi_2O_3 (FIGURE 5.2b). As observed earlier, despite the difference in precursor particle size, a mixed crystalline phase containing the tetragonal Bi_2O_3 (JCPDS, n° 27-0050) and monoclinic $BiVO_4$ (JCPDS, n° 83-1699) crystalline phases was obtained (FIGURE 5.2b). However, use of the *n*-Bi_2O_3 precursor in the heterostructure synthesis resulted in formation of a greater amount of $BiVO_4$, compared to synthesis using the *m*-Bi_2O_3 precursor (FIGURE 5.2b, TABLE 5.1). The increases in V precursor concentration and hydrothermal treatment temperature caused a greater amount of $BiVO_4$ to be formed on the heterostructure. Therefore, the synthesis strategy employed here provided effective growth of $BiVO_4$ on the sacrificial surface of Bi_2O_3. Therefore, the growth of $BiVO_4$ on the Bi_2O_3 surface could be proposed to follow a classical solubilization-precipitation reaction mechanism, as follows:

$$NH_4\,VO_{3(aq)} \rightarrow NH_4^+{}_{(aq)} + VO_3{}^-{}_{(aq)}$$

$$2\,Bi_2O_3 + 4\,VO_3{}^-{}_{(aq)} + 4H^+{}_{(aq)} \rightarrow 4\,BiVO_4 + 2\,H_2O$$

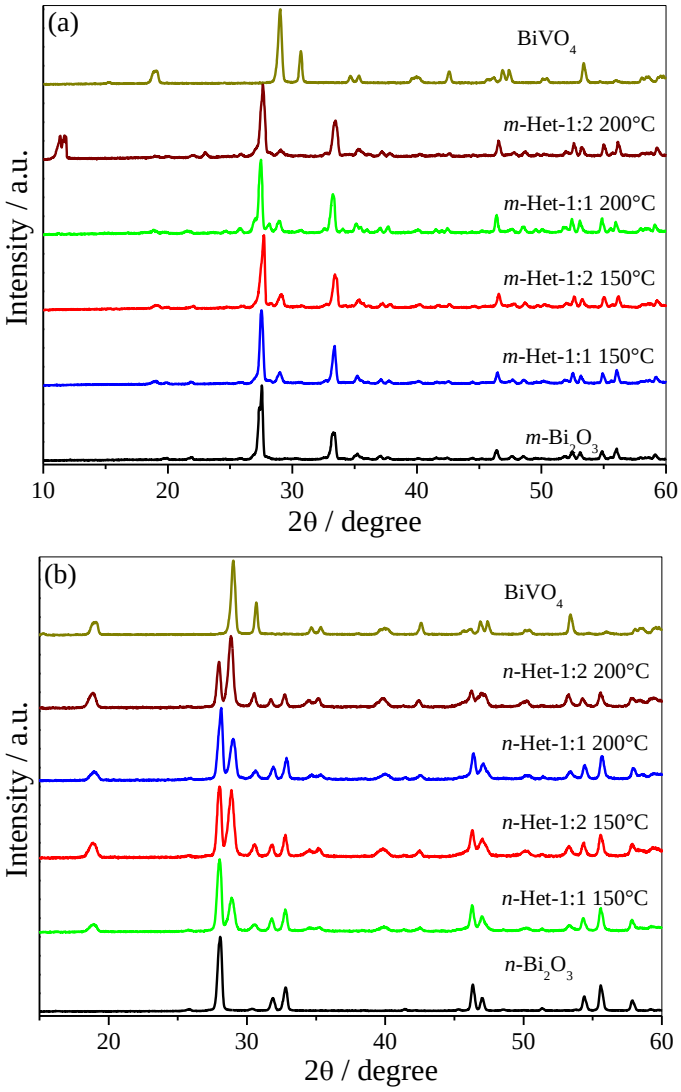

FIGURE 5.2 - – XRD patterns of (a) commercial *m*-Bi_2O_3, $BiVO_4$, and the as-synthesized $Bi_2O_3/BiVO_4$ heterostructures, and (b) commercial *n*-Bi_2O_3, $BiVO_4$, and the as-synthesized $Bi_2O_3/BiVO_4$ heterostructures.

These results are in agreement with the findings of Liang et al. (2014)[89] and De-Kun et al. (2012),[99] who proposed synthesis routes driven by solubility differences between Bi_2S_3 and $Bi_2O_2CO_3$, and between Bi_2S_3 and $BiVO_4$, respectively. These studies used the principle that compounds with high solubility can be converted to compounds with low solubility, as observed by the formation of Bi_2S_3 from $Bi_2O_2CO_3$ and $BiVO_4$, due to its lower solubility, compared to the other compounds.[89,99] Therefore, since *n*-Bi_2O_3 has smaller particle size and higher specific surface area than *m*-Bi_2O_3, *n*-Bi_2O_3 is expected to show higher solubility, and consequently greater conversion to $BiVO_4$ in the presence of the V precursor, in agreement with the XRD results (FIGURE 5.2, TABLE 5.1).

TABLE 5.1 – Weight percentage of the monoclinic $BiVO_4$ phase in the as-synthesized samples.

Samples	Wt. % $BiVO_4$[a]	Wt.% $BiVO_4$[b]
Het-1:1 150°C	16	33
Het-1:2 150°C	18	48
Het-1:1 200°C	18	37
Het-1:2 200°C	13	60

[a] Percentage of $BiVO_4$ phase in heterostructure formed from *m*-Bi_2O_3
[b] Percentage of $BiVO_4$ phase in heterostructure formed from *n*-Bi_2O_3

Considering that NH_4VO_3 is highly water soluble, adsorption over Bi_2O_3 is expected to be the first step, prior to subsequent growth, with the surface reaction occurring by partial dissolution and fast re-precipitation. However, this reaction needs to occur locally in order to ensure heterostructure formation, because otherwise the precipitation could lead to a mixture of phases. Representative SEM images of the as-synthesized heterostructured samples were analyzed to determine the morphology and confirm the crystallization/growth of $BiVO_4$ nanoparticles over the *m*- and *n*-Bi_2O_3 surfaces (FIGURES 5.3 and 5.4, respectively). The *m*-Bi_2O_3 surface showed the presence of rod-like micrometric particles with smooth surfaces. In the case of the *m*-Het-1:1 200 °C sample, particles with size and morphology similar to the *m*-Bi_2O_3 precursor were observed, indicating that *m*-Bi_2O_3 was not fully solubilized and re-precipitated under this condition. However, the existence of a rougher surface composed of a large number of quasi-spherical nanoparticles could be attributed to the $BiVO_4$ phase. In fact, the EDX spectrum and elemental mapping image showed the presence of Bi and V in the *m*-Het-1:1 200 °C sample (see Appendix C, FIGURE C1), confirming that the spherical nanoparticles were related to $BiVO_4$ and had grown evenly on the *m*-Bi_2O_3 surface. In the case of the *m*-Het-1:2 200 °C sample, the EDX spectrum and elemental mapping image of the Bi and V atoms (FIGURE C2) confirmed the formation of a spurious crystalline phase of V ($V_2O_5.nH_2O$). In addition, it was observed that growth of the phases obtained was segregated, with the Bi and V atoms having different spatial positions, in agreement with the XRD observations.

The *n*-Bi_2O_3 sample exhibited uniform spherical morphology, with average particle size of 150 nm and a smooth surface,[78] as can be seen in FIGURE 5.4a. The *n*-Het-1:1 150 °C sample showed particles with size and morphology similar to *n*-Bi_2O_3 (FIGURE 5.4c), which confirmed that this oxide was not fully solubilized during the hydrothermal treatment at 150 ºC. However, it can be observed that the surface of the

n-Het-1:1 150 °C sample became rough, with a large number of nanospheres, which could have been due to the formation of $BiVO_4$ on the *n*-Bi_2O_3 surface. The *n*-Het-1:2 150 °C sample showed particles with clearly different morphology and larger particle size than the *n*-Bi_2O_3 precursor. This could be explained by considering that under this synthesis condition, the excess of V precursor resulted in some particles of *n*-Bi_2O_3 being completely converted in $BiVO_4$, with further growth leading to phase segregation.

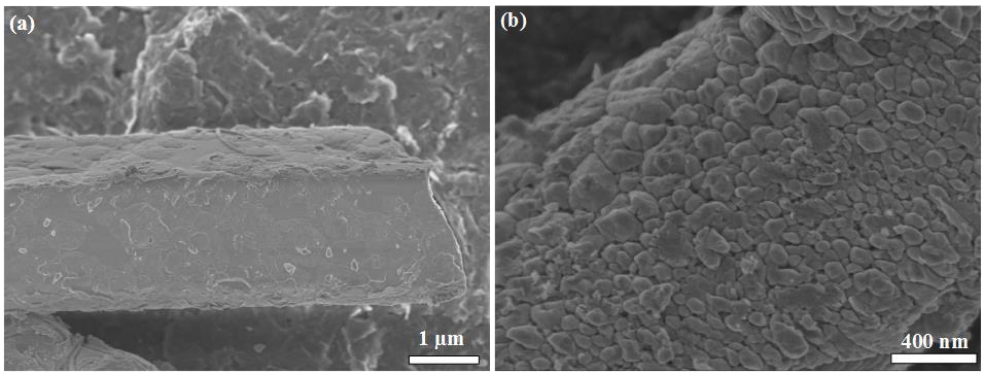

FIGURE 5.3 – Representative FE-SEM images of (a) commercial *m*-Bi_2O_3 and (b) *m*-Het-1:1 200 °C.

For the *n*-Het-1:1 200 °C sample, the particle size and morphology were very similar to the features of the *n*-Bi_2O_3 precursor, but with a rough surface, indicating that $BiVO_4$ had grown on the Bi_2O_3 surface. This result was supported by the EDX spectrum and the elemental mapping image (FIGURE C3), from which it could be seen that under this synthesis condition, the Bi and V atoms shared the same spatial position, confirming the growth of $BiVO_4$ on the Bi_2O_3 surface. The *n*-Het-1:2 200 °C sample presented a completely different morphology and particle size, compared to the *n*-Bi_2O_3 precursor, indicating that there was segregation of $BiVO_4$ after its formation, in agreement with the growth mechanism proposed for the *n*-Het-1:2 150 °C sample. This was confirmed by the EDX spectrum and the elemental mapping of the Bi and V atoms of the *n*-Het-1:2 150 °C heterostructured sample (FIGURE C4), where the V atoms were segregated in specific positions, showing that there were two different phases in the same particles. Therefore, an excess of V precursor in the synthesis had a deleterious effect on the preparation of heterostructures by growth of $BiVO_4$ on the Bi_2O_3 surface, because under these conditions there was a high degree of segregation between the crystalline phases, with this effect being greater at higher hydrothermal treatment temperature.

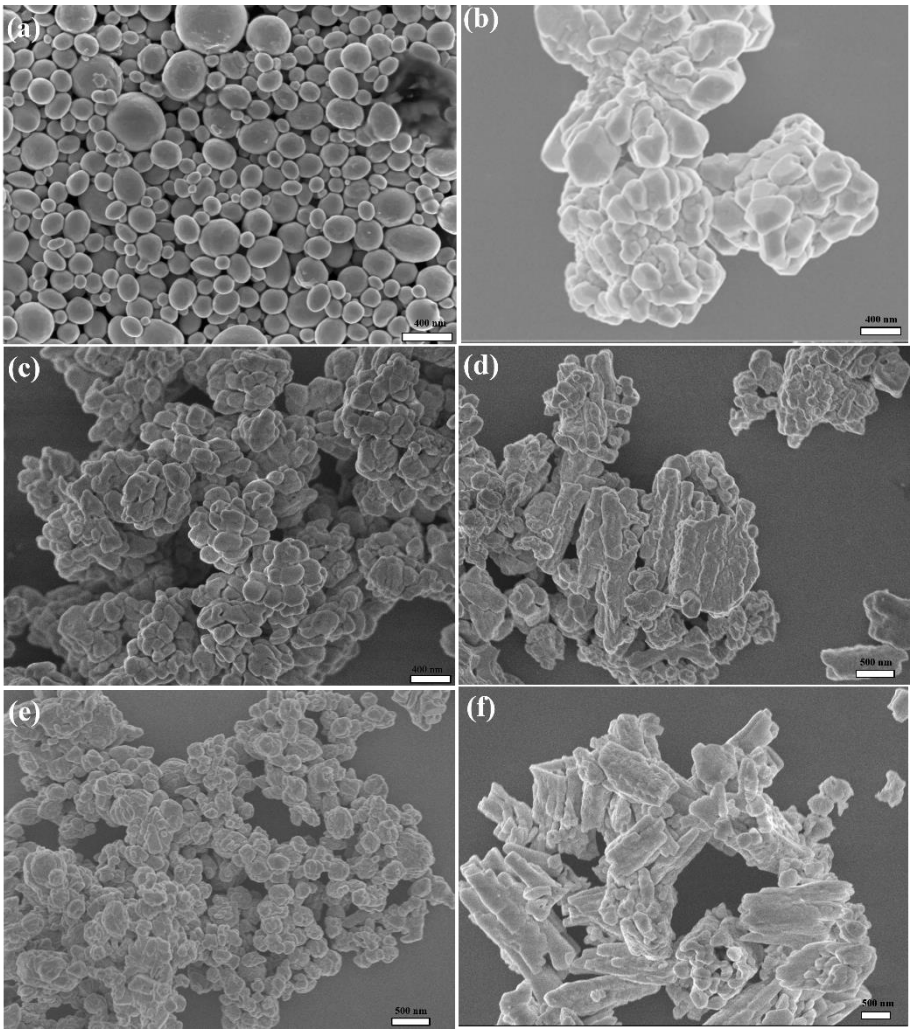

FIGURE 5.4 – Representative FE-SEM images of (a) commercial *n*-Bi_2O_3, (b) $BiVO_4$, (c) *n*-Het-1:1 150 °C, (d) *n*-Het-1:2 150 °C, (e) *n*-Het-1:1 200 °C, and (f) *n*-Het-1:2 200 °C.

Formation of the Bi_2O_3/$BiVO_4$ heterojunction was confirmed by TEM and HRTEM images obtained for the *n*-Het-1:1 200 °C sample (FIGURE 5.5). The TEM image revealed the presence of clearly faceted nanoparticles with sizes smaller than 10 nm on the Bi_2O_3 surface. However, the HRTEM image of this sample (FIGURE 5.5b) showed the coexistence, in the same region, of nanoparticles of $BiVO_4$ and Bi_2O_3 in monoclinic and tetragonal phases, respectively. The growth of $BiVO_4$ on the Bi_2O_3 surface was identified by its interlayer distance of 0.31 nm for the (121) plane. This result confirmed the formation of heterojunctions between Bi_2O_3 and $BiVO_4$.

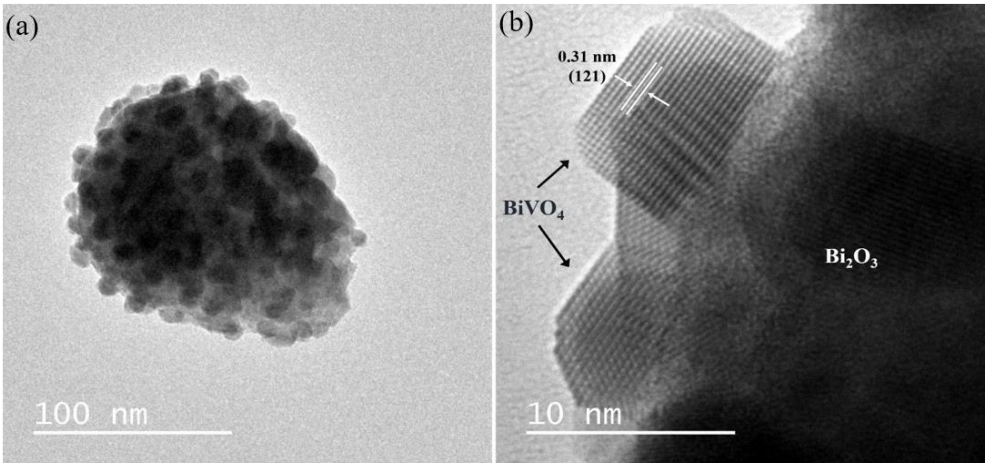

FIGURE 5.5 – TEM and HRTEM images of the *n*-Het-1:1 200 °C sample.

Raman spectroscopy analyses were performed to determine the medium-range structures of the as-synthesized heterostructured samples. The Raman scattering spectra of the *m*-Bi_2O_3 precursor and the corresponding heterostructures are shown in FIGURE 5.6a. The *m*-Bi_2O_3 precursor showed the typical Raman spectrum of monoclinic crystalline Bi_2O_3, with characteristic peaks at 70, 95, 122, 141, 153, 186, 213, 315, 413, 450, and 542 cm^{-1}, with these vibrational modes having A_g or B_g symmetry (or both).[165] The Raman scattering peaks observed in the region below 120 cm^{-1} were mainly assigned to shifts of Bi atoms. Peaks in the range from 120 to 150 cm^{-1} were attributed to shifts of Bi and O atoms, while those above 150 cm^{-1} were assigned to displacements of O atoms.[166] The $BiVO_4$ sample showed a characteristic Raman spectrum with five main peaks at 120, 200, 330, 362, and 826 cm^{-1}.[29] The peaks at 120 and 200 cm^{-1} were assigned to the external vibrational mode of $BiVO_4$, the peaks at 330 and 362 cm^{-1} were related to the asymmetric and symmetric deformation modes of V-O bonds on tetrahedral VO_4, respectively, and the peak at 826 cm^{-1} was assigned to the symmetric stretching mode of V-O bonds with A_g symmetry.[56] The Raman spectra of the heterostructured *m*-Bi_2O_3/$BiVO_4$ samples showed peaks related to both crystalline phases (Bi_2O_3 and $BiVO_4$), in good agreement with the XRD analysis. There was a gradual increase in the intensity of the peaks related to the $BiVO_4$ phase as the amount of V precursor and the hydrothermal treatment temperature were increased. The Raman spectrum of the *n*-Bi_2O_3 precursor showed six well-defined peaks at 70, 91, 127, 232, 315, and 467 cm^{-1}, which could be attributed to tetragonal crystalline Bi_2O_3 (FIGURE 5.6b), where the peaks at 70 and 91 cm^{-1} were related to E_g and A_g symmetry vibration modes of Bi atoms, respectively.[29,165,166] The peaks at 127, 315, and 467 cm^{-1} were assigned to Bi-O bond stretching.[29,165,166] In the case of the *n*-Bi_2O_3/$BiVO_4$ heterostructured samples, the Raman

spectra presented peaks related to both crystalline phase constituents (Bi_2O_3 and $BiVO_4$), in good agreement with the XRD results.

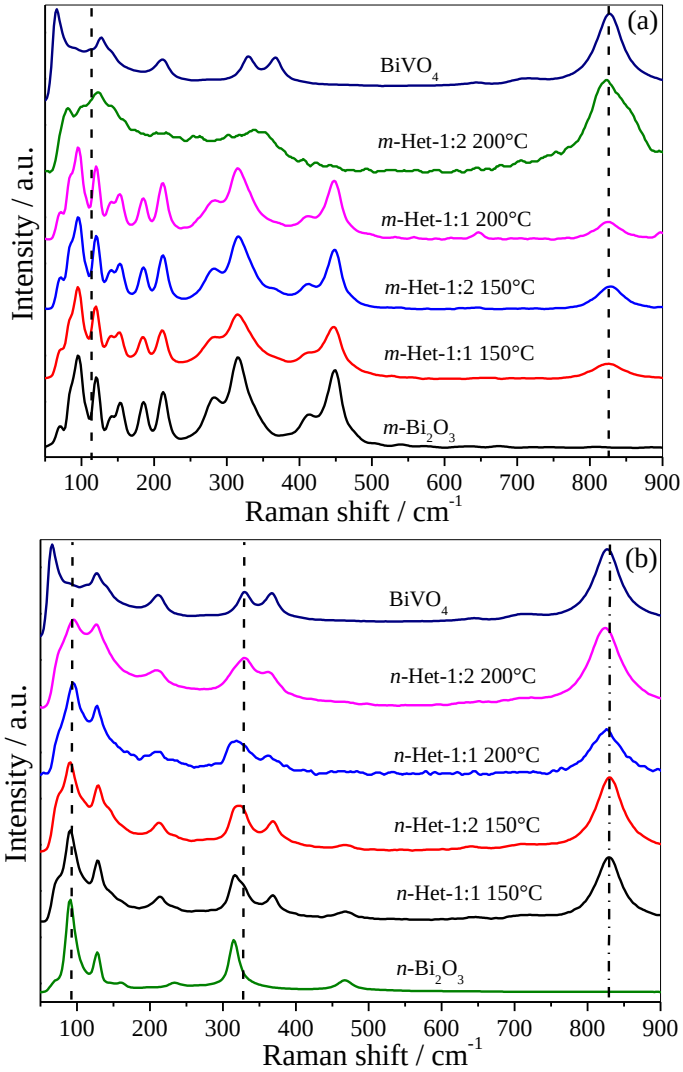

FIGURE 5.6 – Raman scattering spectra of (a) *m*-Bi_2O_3, $BiVO_4$, and the as-synthesized *m*-Bi_2O_3/$BiVO_4$ heterostructures, and (b) *n*-Bi_2O_3, $BiVO_4$, and the as-synthesized *n*-Bi_2O_3/$BiVO_4$ heterostructures.

Due to the fundamental role of the electronic properties of a semiconductor in heterogeneous photocatalysis applications, the band gap values of *m*-Bi_2O_3, *n*-Bi_2O_3, and their corresponding heterostructures were determined by applying the Tauc equation to the DRS data for the samples (FIGURE 5.7, TABLE 5.2). The *m*-Bi_2O_3 precursor showed a band gap of 2.70 eV, in agreement with values previously reported in the literature.[102] The heterostructured *m*-Bi_2O_3/$BiVO_4$ samples showed different band gap values, with small fluctuations, which ranged from 2.35 to 2.40 eV. This confirmed that the $BiVO_4$ evenly decorated the surface of the *m*-Bi_2O_3 precursor, since these band gap

values are characteristic of monoclinic $BiVO_4$. The results demonstrated that the Bi:V ratio and the hydrothermal treatment temperature did not affect the band gap characteristics. The band gap of the *n*-Bi_2O_3 precursor was 2.60 eV (TABLE 5.2).[102] Different band gap features were observed for the *n*-Bi_2O_3/$BiVO_4$ samples (FIGURE 5.7b). The heterostructured *n*-Bi_2O_3/$BiVO_4$ samples showed two band gaps, with values of approximately 2.40 and 2.60 eV related to $BiVO_4$ and *n*-Bi_2O_3, respectively.

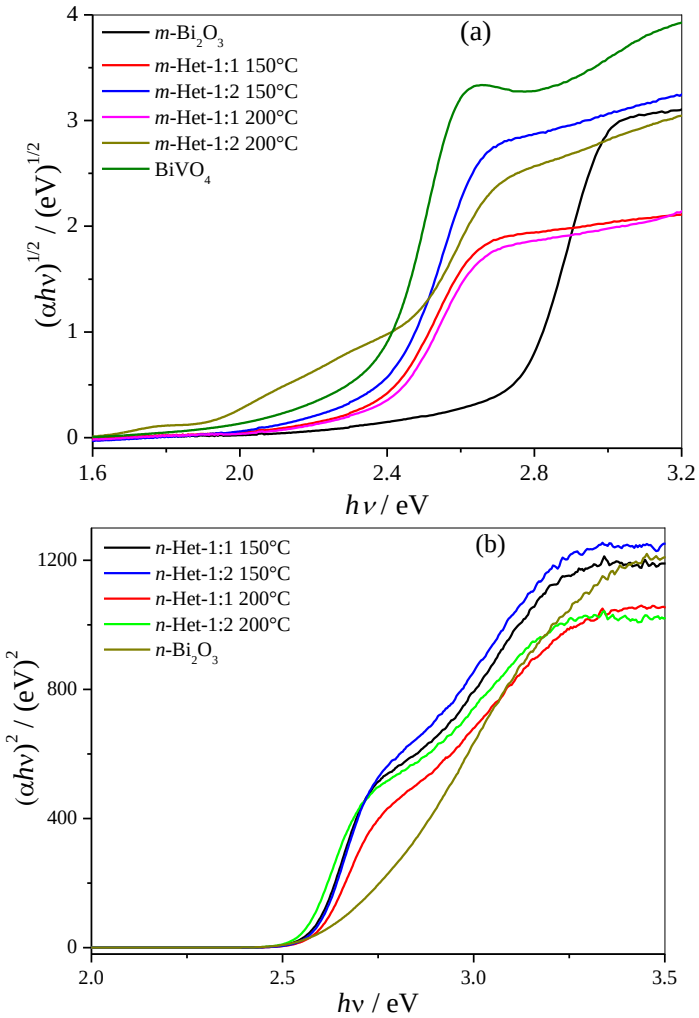

FIGURE 5.7 – Band gap determination applying indirect and direct Tauc plot, respectively, to DRS data of (a) *m*-Bi_2O_3, (b) *n*-Bi_2O_3, and their respective heterostructured samples.

Determination of the specific surface areas of the as-synthesized samples (TABLE 5.3) showed that the formation of $BiVO_4$ on the Bi_2O_3 surface decreased the specific surface area, as expected, due to greater particle size after the synthesis. This

indicated that any positive effect on the photocatalytic performance of the heterostructures was not related to the specific surface area.

TABLE 5.2 – Band gap values of pure *m*-Bi_2O_3 and *n*-Bi_2O_3 and their corresponding heterostructures.

Samples	**Band gap (eV)[a]**	**Band gap (eV)[b]**
Bi_2O_3	2.70	2.60
Het-1:1-150	2.35	2.50 e 2.60
Het-1:2-150	2.40	2.40 e 2.60
Het-1:1-200	2.35	2.50 e 2.60
Het-1:2-200	2.30	2.40 e 2.55

[a] Band gap values of the heterostructures formed from *m*-Bi_2O_3
[b] Band gap values of the heterostructures formed from *n*-Bi_2O_3

TABLE 5.3 - Specific surface area (SSA) of the *m*- and *n*-Bi_2O_3 precursors and their respective heterostructures more photoactive.

Samples	**SSA ($m^2.g^{-1}$)**
m-Bi_2O_3	0.15
m-Het-1:1 200°C	0.10
n-Bi_2O_3	2.80
n-Het-1:1 200°C	0.40
$BiVO_4$	0.60

The photocatalytic properties of the *m*-Bi_2O_3/$BiVO_4$ heterostructures were evaluated using the photodegradation of MB dye and the results were compared to those obtained with the pure *m*-Bi_2O_3 sample (FIGURE 5.8a). All the *m*-Bi_2O_3/$BiVO_4$ heterostructures were photoactive for MB dye photodegradation and showed higher activity than the *m*-Bi_2O_3 precursor. Based on the reaction rate constants, calculated using the pseudo-first order equation (TABLE 5.4), the photoactivity followed the order: *m*-Het-1:1 200 °C > *m*-Het-1:2 200 °C ≈ *m*-Het-1:2 150 °C ≈ *m*-Het-1:1 150 °C. The heterostructure with the greatest amount of $BiVO_4$ showed the highest photoactivity for MB dye degradation, indicating that effective heterojunctions were formed among the *m*-Bi_2O_3 and $BiVO_4$ phases and acted to increase the charge carrier lifetime. FIGURE 5.8b shows the MB dye photodegradation catalyzed by the *n*-Bi_2O_3/$BiVO_4$ heterostructures. As observed previously for the *m*-Het heterostructures, all the heterostructures showed

higher photoactivity, compared to the precursor (*n*-Bi_2O_3). Based on the reaction rate constants (TABLE 5.4), the photoactivity of the heterostructures was in the following order: *n*-Het-1:1 200 °C > *n*-Het-1:2 150 °C > *n*-Het-1:1 150 °C ≈ *n*-Het-1:2 200 °C. For these samples, a composition intermediate between the *n*-Bi_2O_3 and $BiVO_4$ phases resulted in improved photoactivity. The higher activity of the *n*-Het-1:1 200 °C sample was due to an ideal amount of $BiVO_4$ (37 wt.%), together with a better distribution of $BiVO_4$ on the Bi_2O_3 surface. This was because the heterostructures obtained with an excess of V precursor (*n*-Het-1:2 150 °C and *n*-Het-1:2 200 °C) showed high amounts of $BiVO_4$ and segregation between the phases, as observed from the SEM images and the EDX elemental mapping.

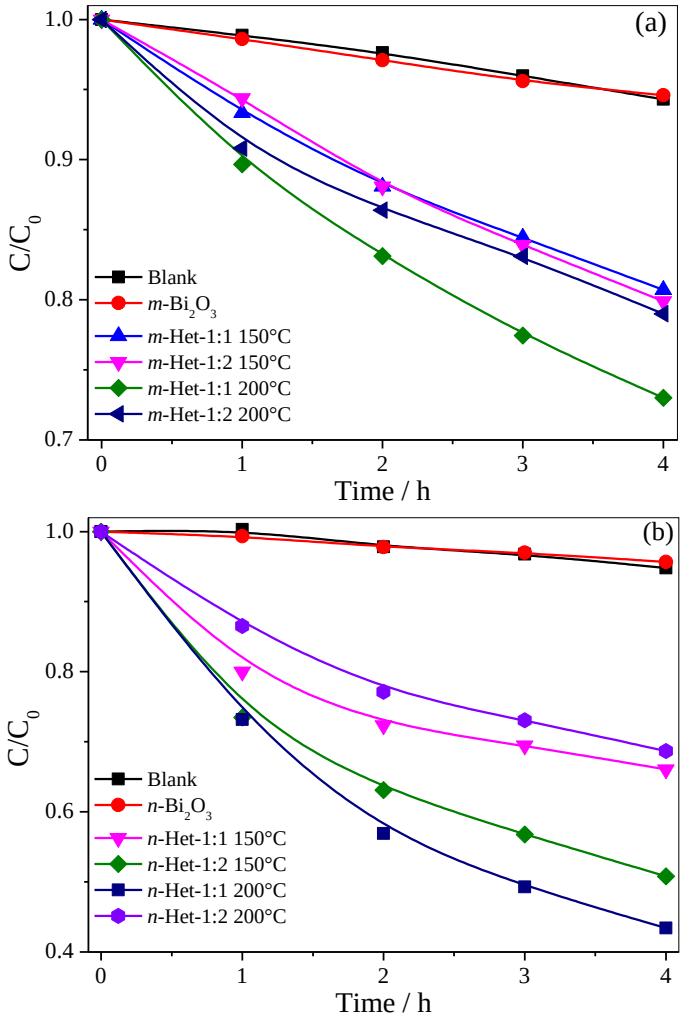

FIGURE 5.8 – Kinetic curves for MB dye (5 mg/L) photodegradation catalyzed by (a) *m*-Bi_2O_3 and the *m*-Bi_2O_3/$BiVO_4$ heterostructures, and (b) *n*-Bi_2O_3 and the *n*-Bi_2O_3/$BiVO_4$ heterostructures.

TABLE 5.4 – First order rate constants (k x 10^2) for the MB dye photodegradation reaction under visible irradiation, catalyzed by Bi_2O_3 and the heterostructures.

Samples	***m*-Bi_2O_3/$BiVO_4$**	***n*-Bi_2O_3/$BiVO_4$**
	***k* x 10^2**	***k* x 10^2**
Bi_2O_3	1.4	1.1
Het-1:1 150 °C	5.2	9.7
Het-1:2 150 °C	5.6	16.0
Het-1:1 200 °C	7.8	20.6
Het-1:2 200 °C	5.6	9.2

[a] reaction catalyzed by heterostrucuture formed from *m*-Bi_2O_3
[b] reaction catalyzed by heterostrucuture formed from *n*-Bi_2O_3

Despite the obvious formation of heterojunctions between the Bi_2O_3 and $BiVO_4$ phases, an additional investigation comparing the heterostructures (*m*-Het-1:1 200 °C and *n*-Het-1:1 200 °C) with the two isolated phases (Bi_2O_3 and $BiVO_4$) and the corresponding physical mixtures was needed in order to confirm the effect of the heterojunctions and formation of the type-II heterostructure. The *m*-Het-1:1 200 °C heterostructure exhibited lower activity for MB dye photodegradation, compared to pure $BiVO_4$ (FIGURE 5.9a). However, the heterostructure showed higher photoactivity than the physical mixture of $BiVO_4$ and *m*-Bi_2O_3 prepared in the same proportions as *m*-Het-1:1 200 °C. This heterostructured sample showed lower activity than pure $BiVO_4$ due to the high amount of *m*-Bi_2O_3 precursor (82 wt.%), which exhibits insignificant photoactivity for MB dye photodegradation under visible irradiation. The *n*-Het-1:1 200 °C sample showed superior photoactivity for MB dye degradation (FIGURE 5.9b), compared to the isolated phases (*n*-Bi_2O_3 and $BiVO_4$) and the corresponding physical mixture. Hence, the as-synthesized *m*-Het-1:1 200 °C and *n*-Het-1:1 200 °C samples both showed higher photocatalytic performance, compared to their corresponding physical mixtures, indicating that formation of the heterojunctions acted to increase the charge carrier lifetimes, probably due to type-II heterostructure formation.

The results showed that the heterostructures obtained with the *n*-Bi_2O_3 precursor were more efficient than the heterostructures obtained with the *m*-Bi_2O_3 precursor. The *n*-Bi_2O_3/$BiVO_4$ heterostructures provided MB dye degradation approximately 2-fold higher than obtained with the *m*-Bi_2O_3/$BiVO_4$ heterostructures. From the previous analysis, this was expected because the heterostructures synthesized using the nanometric Bi_2O_3 particles possessed a greater amount of $BiVO_4$ on their

surfaces, compared to the heterostructures synthesized using the micrometric Bi_2O_3 particles, resulting in increased formation of heterojunctions between the Bi_2O_3 and $BiVO_4$ phases. These effects on photocatalytic performance can be clearly seen from the pseudo-first order reaction rate constants for MB photodegradation as a function of the amount of the $BiVO_4$ phase in the heterostructures (FIGURE 5.10).

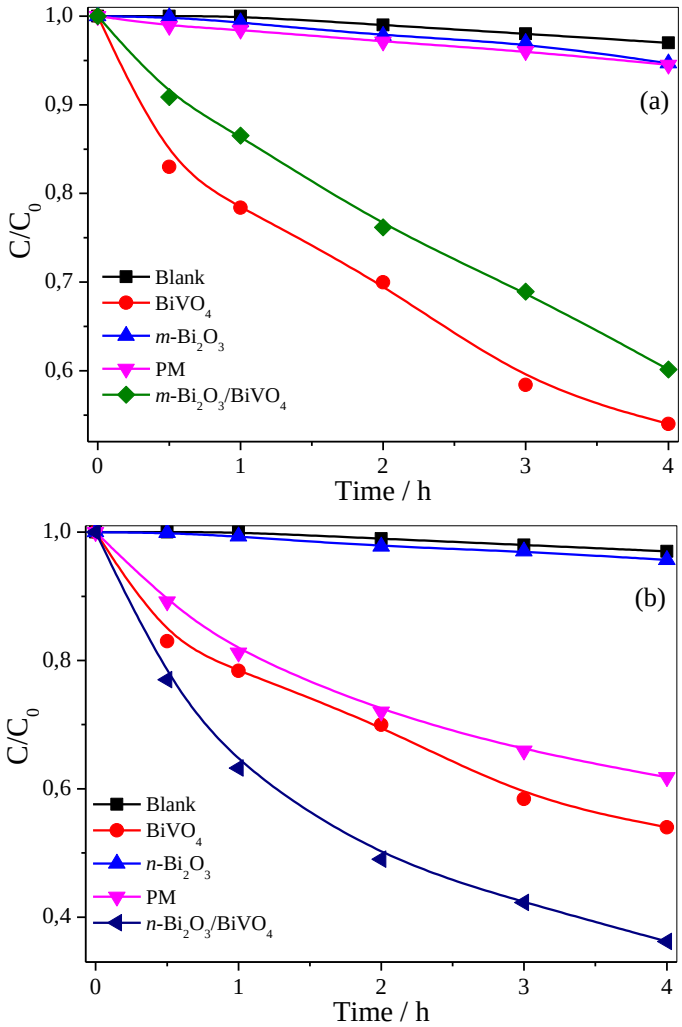

FIGURE 5.9 – Photocatalytic performance in MB dye (5 mg/L) degradation, using the heterostructures obtained with the precursors (a) *m*-Bi_2O_3 and (b) *n*-Bi_2O_3, as well as their corresponding physical mixtures (PM) and the isolated phases.

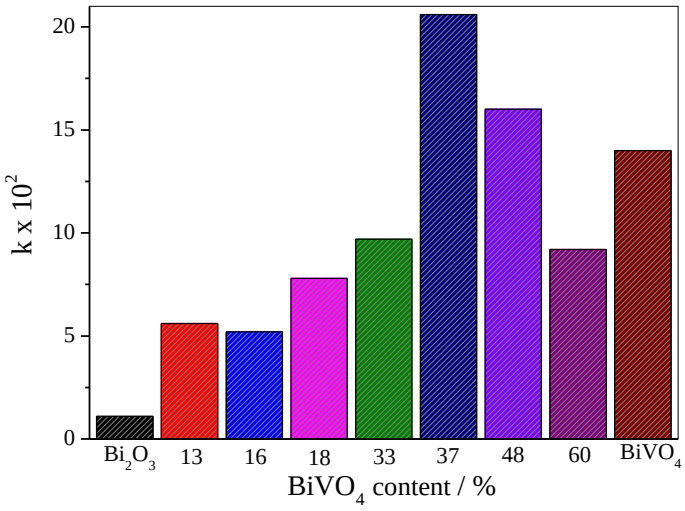

FIGURE 5.10 – First-order rate constants for the MB dye photodegradation reaction as a function of $BiVO_4$ content in the heterostructures.

Finally, in order to confirm formation of the *n*-Bi_2O_3/$BiVO_4$ heterostructure, the electron/hole pair lifetime was calculated using time-resolved photoluminescence (TRPL). The photoluminescence decay spectra at 545 nm of the $BiVO_4$ and *n*-Bi_2O_3/$BiVO_4$ samples are shown in FIGURE 5.11. The TRPL decays of both samples were fitted with a first order exponential function in order to calculate the charge carrier lifetime. The electron/hole pair lifetime of the *n*-Bi_2O_3/$BiVO_4$ heterostructure was significantly higher than that of the pure $BiVO_4$. The lifetime of the band-band emission (the electron/hole pair recombination at 545 nm) of the *n*-Bi_2O_3/$BiVO_4$ heterostructure was 0.71 ns, while the lifetime for $BiVO_4$ was about 0.20 ns. These results showed that the lifetime of the electron/hole pair of the *n*-Bi_2O_3/$BiVO_4$ heterostructure was 3.5-fold longer, compared to pure $BiVO_4$, proving that the junction of Bi_2O_3 with $BiVO_4$ formed a suitable type-II heterostructure.

The enhanced photocatalytic activity of the Bi_2O_3/$BiVO_4$ heterostructures could therefore be explained by spatial separation of the photogenerated electron/hole pair. The interface between the phases enabled transfer of the photogenerated electrons from the *p*-type (Bi_2O_3) to the *n*-type ($BiVO_4$) semiconductor, while the photogenerated holes were transferred from the *n*-type ($BiVO_4$) to the *p*-type (Bi_2O_3) semiconductor.[92,97,98] Hence, the photogenerated electrons were accumulated in the $BiVO_4$ conduction band, while the photogenerated holes were accumulated in the Bi_2O_3 valence band, where the MB dye oxidation reaction occurred.

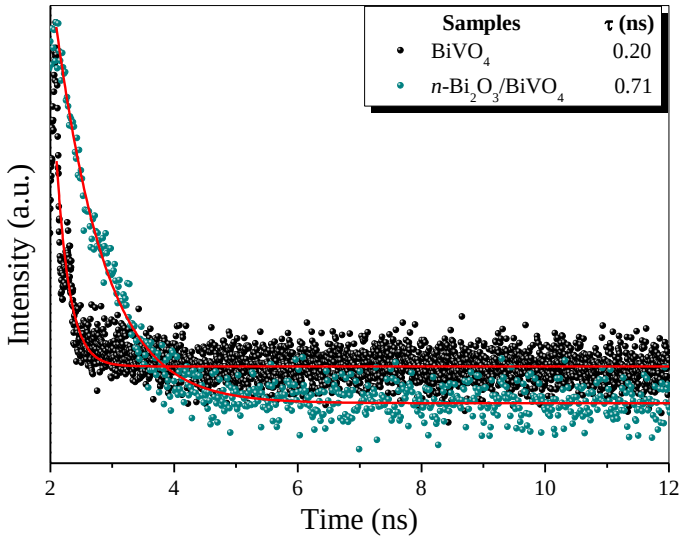

FIGURE 5.11 – Observed (points) and calculated (lines) time-resolved photoluminescence intensities (decay lifetimes) of the *n*-$Bi_2O_3/BiVO_4$ and Het-1:0.3 samples. The powders were excited at 405 nm and photoluminescence was monitored at 545 nm.

5.5. - Conclusions

An alternative method to obtain $Bi_2O_3/BiVO_4$ heterostructures, based on solubility differences, was developed using preformed micro- or nanometric particles of Bi_2O_3. The technique enabled efficient heterojunction tailoring, with the amount of $BiVO_4$ in the heterostructure being dependent on the particle size of the preformed Bi_2O_3, due to solubility differences between micro- and nanometric Bi_2O_3. The mechanism of growth of $BiVO_4$ on a self-sacrificial Bi_2O_3 surface was elucidated and formation of the $Bi_2O_3/BiVO_4$ heterojunctions was confirmed from HRTEM images. The photocatalytic activity was enhanced due to the formation of the $Bi_2O_3/BiVO_4$ heterostructures, compared to the isolated phases. The formation of the type-II heterostructure acted to increase the spatial separation of the photogenerated electron/hole pair, consequently increasing its lifetime, as demonstrated by PL and TRPL analyses.

6. - Chapter IV: Is the solubility difference method, used to obtain $Bi_2O_3/BiVO_4$ heterostructures, efficient to other schemes?

The content of this chapter is an adaptation of the manuscript entitled **"Insights into the Photocatalytic Performance of $Bi_2O_2CO_3/BiVO_4$ Heterostructure Prepared by One-Step Hydrothermal Method"** by Osmando F. Lopes, Kele T. G. Carvalho, Waldir Avansi Jr, Debora M. B. Milori and Caue Ribeiro that is under preparation.

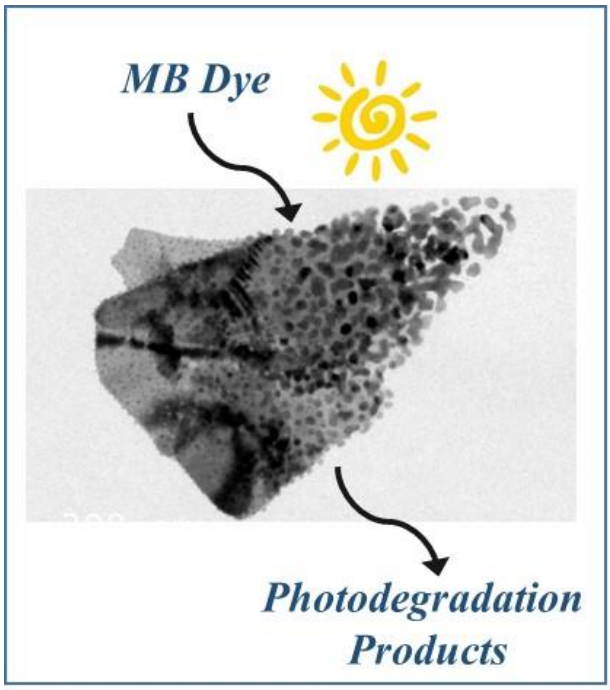

6.1. - Abstract

This paper describes the synthesis of $Bi_2O_2CO_3/BiVO_4$ heterostructures through a one-step method based on the difference in solubility between two semiconductors that possess a metal in common. The as-synthesized $Bi_2O_2CO_3/BiVO_4$ heterostrucutures were characterized by X-ray diffraction (XRD), thermogravimetric analysis (TGA), Raman spectroscopy, ultraviolet-visible diffuse reflectance spectroscopy (UV-Vis DRS), scanning electron microscopy (SEM), transmission electron microscopy (TEM), N_2 physisorption, X-ray photoelectron spectroscopy (XPS) and time resolved photoluminescence spectroscopy (TRPL). The role of the heterojunction formed was evaluated by methylene blue (MB) dye photodegradation under visible and UV irradiation. The formation of the heterostructure was observed indirectly by the great increase in the thermal stability of $Bi_2O_2CO_3$ phase when compared to its pure phase. The amount of heterojunction formed between the $Bi_2O_2CO_3$ and $BiVO_4$ was tuned by vanadium precursor concentration. The proposed strategy was efficient for obtaining $Bi_2O_2CO_3/BiVO_4$ heterostructures with enhanced photocatalytic performance when compared to their isolated phases, MB photodegradation occurred mainly by the action of $^{\bullet}OH$ radicals, i.e. by an indirect mechanism. Based on TRPL spectroscopy and VB-XPS results, an enhancement of photoactivity related to increase in the spatial separation of photo-generated electron/hole pair was observed due to the formation of a type-II heterostructure.

6.2. - Introduction

The use of semiconductor in photocatalytic processes has many applications, due to the possibility of inducing reactions of great interest in a rapid and efficient way, such as: organic pollutants photodegradation and water-splitting.[25,112,167,168] Among various semiconductors, bismuth-containing materials as bismuth subcarbonate ($Bi_2O_2CO_3$) has remarkable properties that make it a great candidate for photocatalytic applications.[89,169] The origin of suitable properties of $Bi_2O_2CO_3$ is due to the internal layered structure of aurivillius structured, which could guide the lower growth rate along (001) axis compared to that along other axes, and thus form 2D morphologies like nanosheets.[80,86,169] However, $Bi_2O_2CO_3$ exhibits two main drawbacks for photocatalytic applications: the rapid recombination of electron/hole pairs and the impossibility of activation under visible irradiation.[80]

Several strategies have been developed to minimize or overcome these undesirable effects. In particular, the association of semicondutors with metals or other semiconductors to form heterostructures is a promising approach.[22,168] Previous studies have shown that heterostructure formation can extend spectral response range and efficiently separate charge carriers, provoking a synergistic effect between the semiconductors.[170–173] In this sense, the formation of a heterostructure between $Bi_2O_2CO_3$ and $BiVO_4$ is an interesting approach to enhance photocatalytic properties due to their suitable electronic characteristics for a type-II heterostructure and also $BiVO_4$ is active under visible irradiation.[86] Different strategies have been studied to obtain heterostructures such as one-step methods (simultaneous crystallization)[92,98,174] and the use of one and/or two preformed particles (heterojunctions formation by attachment).[37,175] The growth of $BiVO_4$ on $Bi_2O_2CO_3$ surface (preformed) under hydrothermal conditions driven by their difference in solubility is a more interesting and efficient approach for the formation of this kind of heterostructure. This is because the formation of the heterojunction is unavoidable, since mandatorily $BiVO_4$ will grow using the bismuth present on the surface of $Bi_2O_2CO_3$.

Therefore, we study this method to obtain $Bi_2O_2CO_3/BiVO_4$ heterostructure using preformed $Bi_2O_2CO_3$ particles based on hydrothermal treatment. The effect of the molar ratio between $Bi_2O_2CO_3$ and the vanadium precursor on the amount of $BiVO_4$ grown on $Bi_2O_2CO_3$ surface was evaluated. The role of heterojunction formation on photocatalytic performance was probed by methylene blue dye photodegradation under visible and UV irradiation and by time resolved photoluminescence spectroscopy. The formation of a type-II heterostructure between $Bi_2O_2CO_3$ and $BiVO_4$ and its charge transfer mechanism for the increase in charge carrier lifetime was also proposed.

6.3. - Experimental

Synthesis of $Bi_2O_2CO_3/BiVO_4$ heterostructures – To obtain the $Bi_2O_2CO_3/BiVO_4$ heterostructures, 0.2 g of $Bi_2O_2CO_3$ (obtained by a typical synthesis[102] between $Bi(NO_3)_3.5H_2O$ and Na_2CO_3) and suitable amounts of NH_4VO_3 (Vetec, 99%) were added to 35 mL of distilled water and the solution was hydrothermally treated at 150 °C for 12h. The precipitate was washed with distilled water and centrifuged to remove impurities and was dried in an oven at 50 °C. Three different molar ratios of Bi:V were studied: 1:1, 1:0.7 and 1:0.3 and the samples were named as $BiVO_4$, Het-1:0.7, and

Het-1:0.3, respectively. For comparative purposes, pure $Bi_2O_2CO_3$ was also hydrothermally treated at 150 °C for 12h.

Heterostructures Characterization - X-ray diffraction (XRD) was conducted in a Shimadzu XRD6000 diffractometer operating with a nickel-filtered Cu Kα radiation generated at 30 kV and a filament current of 30 mA. The 2θ range from 10 to 60° was continuously scanned at speed of 1° min^{-1} with a step width of 0.02°. Raman spectroscopy analyses were performed with a FT-Raman spectrometer (Bruker RAM II with a Ge detector), equipped with a Nd:YAG laser with a wavelength centered at 1064 nm generating a power of 100 mW at a resolution of 2 cm^{-1}. Thermogravimetric analysis (TGA) of the as-synthesized samples was performed in a TA Q500 thermogravimetric analyzer (TA Instruments) under the following conditions: weight 10.00 ± 0.50 mg; synthetic air flow of 60 mL min^{-1}; heating rate 10 °C min^{-1}; and temperature range of 30–550 C. UV-Vis diffuse reflectance spectra (DRS) were recorded with a UV-2600 Shimadzu spectrophotometer coupled with an integrating sphere (ISR-2600Plus) from 250 to 800 nm to determine the band gap of the materials. The measurements were performed in the total reflection mode with $BaSO_4$ as a reference.

The morphology of the as-synthesized samples was verified by images obtained in a field emission gun scanning electron microscope (FE-SEM Jeol JSM 6701F) working at 5 kV. Semi-quantitative atomic compositions were evaluated by energy-dispersive X-ray spectroscopy (EDS) using a Thermo Noran device coupled to a SEM (Jeol JEM 2010). High resolution transmission electron microscopy (HRTEM FEI - TECNAI) operating at 200 kV was employed to verify the formation of the heterostructures. The samples were prepared by wetting carbon-coated copper grids with a drop of colloidal alcoholic suspensions and drying in air.

Specific surface area (SSA) of the as-synthesized samples was estimated applying the BET model to N_2 adsorption data conducted at -196 ºC with a Micrometrics ASAP 2000 equipment. Before the analysis, the samples were pre-treated (degassed) by heating at 80 °C under vacuum until reaching a degassing pressure lower than 20 µmHg. Chemical surface analysis was performed with a K-Alpha XPS equipment (Thermo Fisher 1 Scientific, UK) using Al Kα X-rays, vacuum > 10^{-8} mbar and charge compensation during measurements. The survey and high-resolution spectra were recorded using a pass energy of 1.0 and 0.1 eV, respectively. The binding energy was referenced to the C 1s peak at 284.8 eV. The data analysis was performed using the CASA XPS software.

Photocatalytic tests - The photoactivity of the as-synthesized samples was evaluated for the degradation of methylene blue (MB) dye under visible and ultraviolet (UV) irradiation. In typical procedure, 10 mg of a photocatalyst was placed in contact with 20 mL of aqueous solution of MB (10 mg·L^{-1}). All the experiments were carried out in a photoreactor equipped with six UVC (Philips TUV, 15 W, maximum intensity at 254 nm, and light intensity at 20 cm of 4.0 mW·cm^{-2}) or six fluorescent (Osram, 15 W, and maximum intensity at 440 nm) lamps, a magnetic stirrer, and a heat exchanger that maintained the temperature at 18 °C. The photodegradation of the MB dye was monitored at regular intervals by its maximum absorbance at 654 nm using a Shimadzu-UV-1601 PC spectrophotometer. Before the kinetic experiments, the suspensions were kept in the dark for 12 h to reach adsorption/desorption equilibrium.

The hydroxyl radical ($^{\bullet}OH$) generated in the photocatalytic process under visible irradiation was indirectly detected by using a fluorescent probe, terephtalic acid (TA).[95,104,105,133] TA readily reacts with $^{\bullet}OH$ to form 2-hydroxyterephthalic acid (HTA), a highly fluorescent product with emission at approximately 425 nm. The amount of HTA is directly proportional to the quantity of $^{\bullet}OH$ radicals produced by the irradiated photocatalyst. In a typical procedure, 10 mg of the photocatalyst was added to 20 mL of TA solution ($5x10^{-4}$ mol L^{-1}) prepared from a dilute NaOH solution ($2x10^{-3}$ mol L^{-1}), and the dispersions were maintained under visible irradiation for 2h. After this period, an aliquot was analyzed in a Shimadzu RF-5301PC spectrofluorophotometer, and the fluorescence emission spectra were obtained with an excitation wavelength of 315 nm.

The lifetime of the charge carriers of the as-synthesized samples were determined by time resolved photoluminescence using time-correlated single photon counting (TCSPC). A pulsed diode laser head of 405 nm (LDH P-C-405, PicoQuant) with an approximate 50 ps pulse width and 40 MHz repetition rate was used as the excitation source. The PL emission was spectrally resolved using collection optics and an emission monochromator. The TCSPC module (PicoHarp 300, PicoQuant) was used for ultrafast detection. The deconvolution of the PL decay was performed using a fitting software (FluoFit, PicoQuant) to deduce the time constant associated with exponential decay.

6.4. - Results and Discussion

X-ray diffraction (XRD) patterns of the as-synthesized samples were collected to verify the presence of $BiVO_4$ and $Bi_2O_2CO_3$ phases (FIGURE 6.1). The pure $Bi_2O_2CO_3$ sample which was hydrothermally treated showed a typical XRD pattern

assigned to tetragonal crystalline phase (JCPDS, n° - 041-1488) without any contaminant or spurious phase indicating crystallographic stability under the hydrothermal treatment. When $Bi_2O_2CO_3$ was hydrothermally treated in the presence of V precursor with molar ratio of Bi:V 1:0.3 (Het-1:0.3 sample) an intense diffraction peak at $2\theta \approx 28.8$ related to monoclinic $BiVO_4$ crystalline phase (JCPDS, n° - 083-1699) was observed. The decrease of $Bi_2O_2CO_3$ content in the heterostructure is difficult to visualize by XRD patterns since the most intense diffraction peak, i.e. (103) plane, it is overlapped by the diffraction peak of $BiVO_4$ referent to the (004) plane. However, the disappearance of $Bi_2O_2CO_3$ phase can be easily visualized by the decreasing intensity of the peak referent to the (110) plane. Further, it was observed that increasing the proportion of the V precursor (Het-1:0.7 sample) increased significantly the amount of $BiVO_4$ formed. With an increase in the molar ratio between Bi:V, i.e. 1:1, it was observed that $Bi_2O_2CO_3$ converted fully into $BiVO_4$, without any spurious phase. In this sense, the formation of $BiVO_4$ on $Bi_2O_2CO_3$ surface or the full transformation can occur according to the reactions below[176]:

$$Bi_2O_2CO_{3(aq)} \rightarrow [Bi_2O_2]^{2+} + CO_3^{2-}$$
$$NH_4VO_3 \rightarrow NH_4^+ + VO_3^-$$
$$[Bi_2O_2]^{2+} + 2VO_3^- \rightarrow 2BiVO_4$$

These results are in agreement with previous studies,[89,99] where the principle that compounds with high solubility can be converted into compounds with low solubility was utilized to obtain heterostructures of $Bi_2S_3/Bi_2O_2CO_3$ and $Bi_2S_3/BiVO_4$.[89,99]

FIGURE 6.2 shows the Raman scattering spectra of the as-synthesized samples. The $Bi_2O_2CO_3$ sample showed a typical Raman spectrum, with characteristic bands at 1068, 367, 166 and 80 cm^{-1}. The band at 1068 cm^{-1} was assigned to symmetric stretching of CO_3^{2-}, while the three bands below 400 cm^{-1} were related to vibrational modes of Bi=O bond lattice.[86] For the Het-1:0.7 and Het-1:0.3 samples, all the bands related to $Bi_2O_2CO_3$ disappeared, however the typical Raman spectrum of monoclinic $BiVO_4$ phase with characteristic bands at 826, 362, 330, 200, and 120 cm^{-1} can be observed.[78] This effect is most likely due to the coating of the $Bi_2O_2CO_3$ surface by $BiVO_4$, resulting in a higher Raman scattering intensity related to $BiVO_4$ rather than $Bi_2O_2CO_3$.

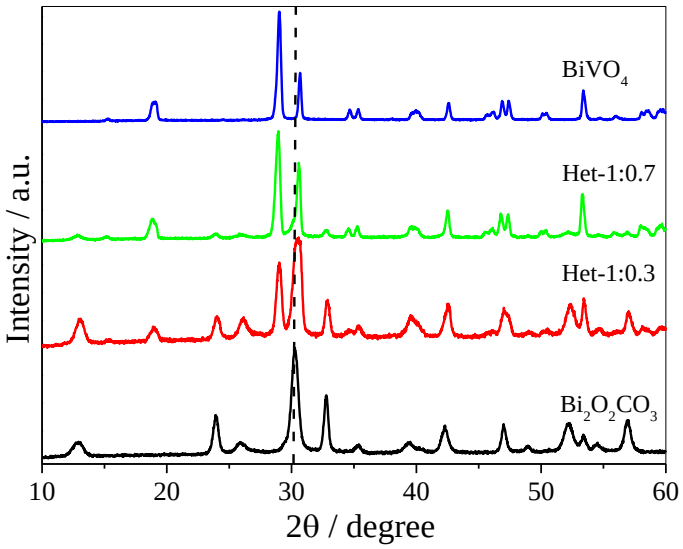

FIGURE 6.1 - XRD patterns of $Bi_2O_2CO_3$, $BiVO_4$ and $Bi_2O_2CO_3/BiVO_4$ samples in different molar ratios of Bi:V.

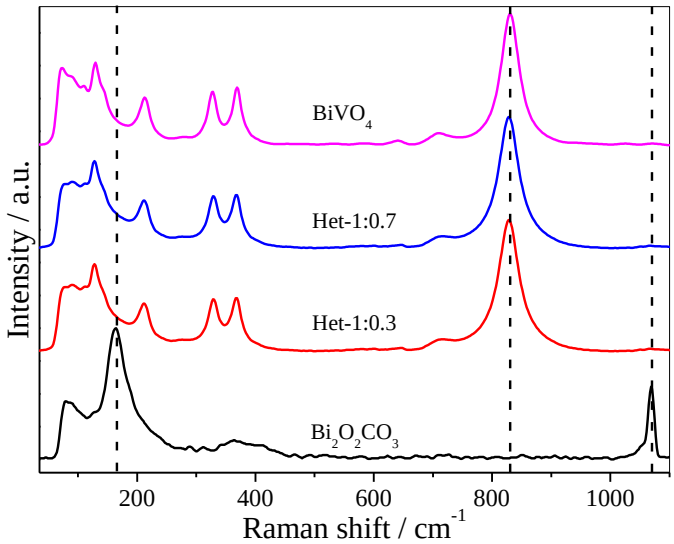

FIGURE 6.2 - Raman scattering spectra of $Bi_2O_2CO_3$, $BiVO_4$ and $Bi_2O_2CO_3/BiVO_4$ samples.

Thermogravimetric analysis (TGA) of $Bi_2O_2CO_3$, $BiVO_4$ and Het-1:0.7 samples were performed to evaluate the thermal decomposition of $Bi_2O_2CO_3$ (i.e., the formation of Bi_2O_3 by the loss of carbonate group) and the concentration of $BiVO_4$ in the heterostructured samples. As shown in FIGURE 6.3a the $Bi_2O_2CO_3$ sample lost ~9.0 % of its initial mass, due to the total decomposition of the carbonate group. On the other hand, the $BiVO_4$ sample exhibited an insignificant weight loss (lower than 0.2 wt.%), which confirms that the $Bi_2O_2CO_3$ phase reacted completely to form $BiVO_4$ when the Bi:V molar ratio of 1:1 was used. From these results, it is possible to observe that

$Bi_2O_2CO_3$ reacts completely to form $BiVO_4$ in this condition. The Het-1:0.7 sample showed a weight loss of ~4.3 %, meaning that the $Bi_2O_2CO_3$ content in this heterostructure is approximately 45 wt%, which is in close agreement with the theoretical amount, i.e. 40 wt% of $Bi_2O_2CO_3$. The analysis of the derivative thermogravimetry (DTG) curves in FIGURE 6.3b showed that the decomposition temperature of $Bi_2O_2CO_3$ occurs at 356 °C, while in the Het-1:0.7 sample this event occur at 460 °C. The increase in decomposition temperature of the carbonate group (> 100 °C) for the Het-1:0.7 sample is due to the formation of a heterojunction with strong interaction between the phases. This result suggests that the heterojunction was not formed by the complete dissolution of the $Bi_2O_2CO_3$ phase followed by the subsequent crystallization of both phases in a segregated form, but rather the formation of $BiVO_4$ occurred directly on the surface of $Bi_2O_2CO_3$, which acts as a Bi provider.

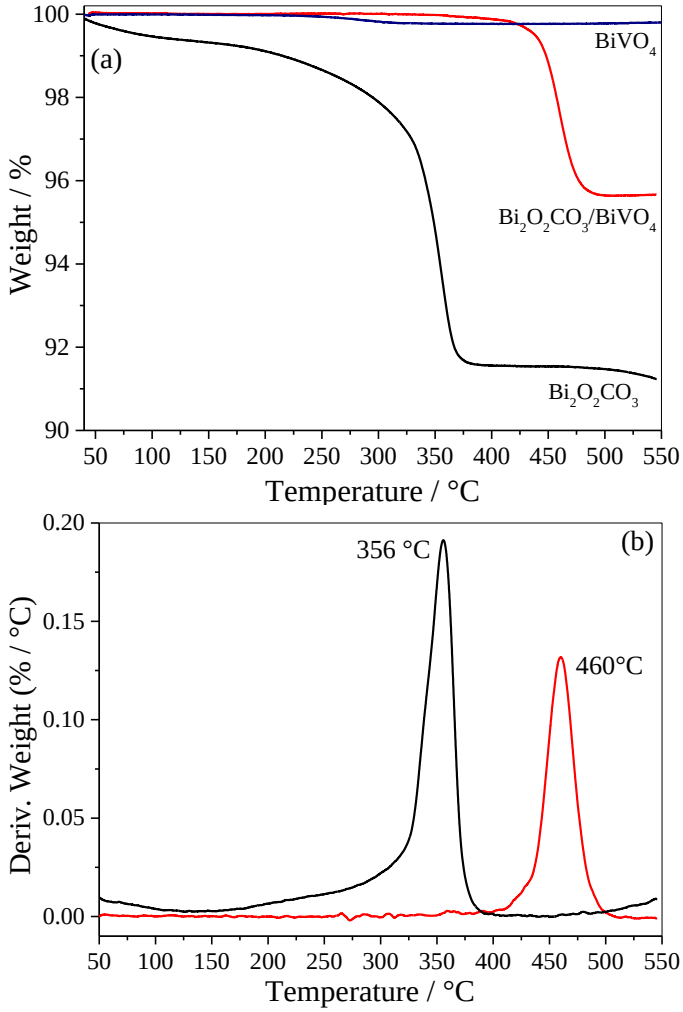

FIGURE 6.3 – (a) Thermogravimetric analysis (TGA) and (b) their respective derivative (DTG) for $Bi_2O_2CO_3$, $BiVO_4$ and Het-1:0.7 samples.

The morphology of the as-synthesized samples was examined using scanning electron microscopy (SEM), and representative images are shown in FIGURE 6.4. The $Bi_2O_2CO_3$ sample exhibited a typical morphology of this phase, i.e. micrometric sheets with nanometric thickness.[86,169] Pure $BiVO_4$ showed dense micrometric particles with different shapes and sizes. The heterostructured $Bi_2O_2CO_3/BiVO_4$ samples exhibited characteristic morphology referent to both phases in the same region. However, it can be observed that in some regions, apparently the $Bi_2O_2CO_3$ phase was completely converted into $BiVO_4$, resulting in a heterogeneous morphology.

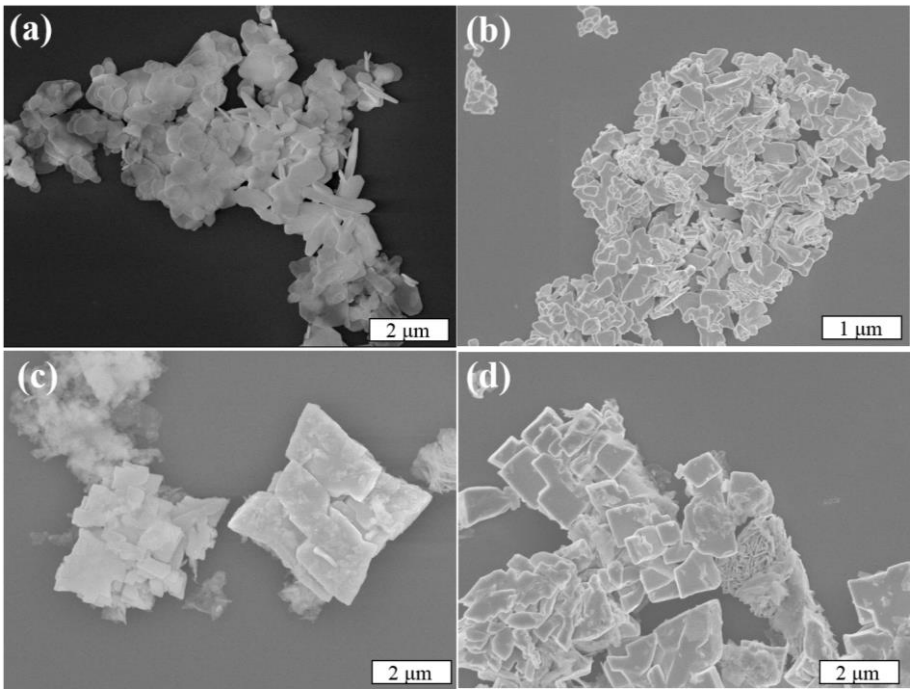

FIGURE 6.4 – Representative FE-SEM images of (a) $Bi_2O_2CO_3$, (b) $BiVO_4$ (c) Het-1:0.3 and (d) Het-1:0.7 samples.

As shown in FIGURE 6.5a, the Het-1:0.3 sample presented morphology very similar to pure $Bi_2O_2CO_3$, except for the nanoparticles on its surface. The HRTEM image of this sample (FIGURE 6.5b) confirms that the particles on the $Bi_2O_2CO_3$ surface are $BiVO_4$ in the monoclinic phase, FIGURE 6.5b. The growth of $BiVO_4$ over $Bi_2O_2CO_3$ was identified by its interlayer distance of 0.31 nm referent to the (121) plane. This result indicates the formation of heterojunctions between the $Bi_2O_2CO_3$ and $BiVO_4$ phases.

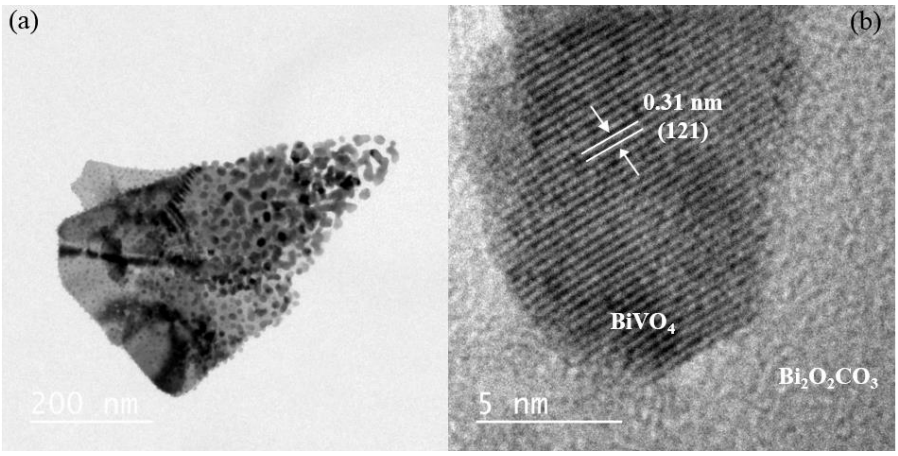

FIGURE 6.5 – (a) TEM and (b) HRTEM images of the Het-1:0.3 sample.

The band gap values of the as-synthesized samples were determined by applying the Tauc equation to UV-Vis DRS data (FIGURE 6.6). The $Bi_2O_2CO_3$ and $BiVO_4$ samples exhibited band gap values of 3.40 and 2.40 eV, respectively, which are in agreement with those described in the literature for these phases.[78,89,169] The Het-1:0.3 sample exhibited two band gap values of 2.35 and 2.75 eV, which are related to both phases that compose it. The Het-1:0.7 sample showed only a band gap value of 2.40 eV related to $BiVO_4$ phase, indicating that $BiVO_4$ covering the surface of $Bi_2O_2CO_3$, as observed by Raman analysis (FIGURE 6.2).

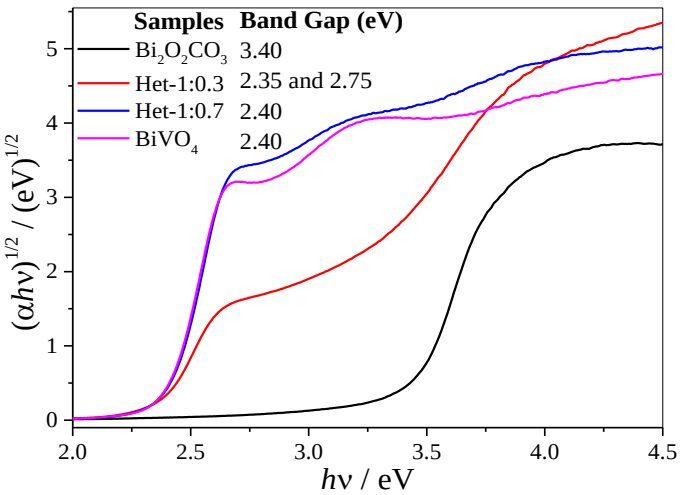

FIGURE 6.6 – Tauc equation applied to DRS UV-Vis data to obtain the band gap values of the $Bi_2O_2CO_3$, $BiVO_4$, Het-1:0.7 and Het-1:0.3 samples.

The photocatalytic properties of the as-synthesized samples were evaluated by MB dye photodegradation under visible and UV irradiation (FIGURE 6.7a and b). The experiments were conducted using two different radiation sources (visible and UV) because the $Bi_2O_2CO_3$ phase is only active under UV irradiation. The self-

photodegradation percentages of the MB dye (FIGURE 6.7), i.e. direct photolysis, were approximately 6 and 14 % under Vis and UV irradiation, respectively. Further, before the photocatalytic tests, the as-synthesized samples were kept in contact with the MB dye solution for 120 min to reach adsorption/desorption equilibrium, and it was observed that all the samples presented insignificant MB adsorption, thus, the observed MB discoloration can be related to its oxidation. The MB photodegradation curves in FIGURE 6.7a and b show that all samples were photoactive, since their curves are below the pure MB curve. The activity of the photocatalysts followed the same order under both radiation sources: Het-1:0.3 > Het-1:0.7 > $BiVO_4$ > $Bi_2O_2CO_3$, as observed in TABLE 6.1. In fact, from these results, it is clear that the heterostructured samples showed higher photoactivity than the pure $Bi_2O_2CO_3$ and $BiVO_4$ phases. This finding evidences interface creation between the $Bi_2O_2CO_3$ and $BiVO_4$ phases, resulting in the a type-II heterostructure formation, and leading to an increase of charge carrier lifetime. It is worth pointing out that the heterostructure formation extended spectral response range since the heterostructure with the higher amount of $Bi_2O_2CO_3$ showed higher photocatalytic performance under visible irradiation.

Due to the nature of catalytic process, i.e. the process takes place on the catalyst's surface, the specific surface area (SSA) of the as-synthesized samples was determined (TABLE 1). The formation of $BiVO_4$ on $Bi_2O_2CO_3$ surface decreased the SSA compared to that of the $Bi_2O_2CO_3$ precursor, because of morphological transformation. As previously seen in the SEM images (FIGURE 6.4), the size of the particles increased after the synthesis of $BiVO_4$. Therefore, this is an indication that any enhancement of the photocatalytic performance of the heterostructures cannot be related to their SSA.

TABLE 6.1 – Kinetic constants for MB dye photodegradation under visible (k_{vis}) and UV (k_{uv}) irradiation, and specific surface area of the as-synthesized samples.

Samples	k_{vis} **x** 10^2 / h^{-1}	k_{uv} **x** 10^2 / h^{-1}	**SSA** ($m^2.g^{-1}$)
MB	0.1	6.0	--
$Bi_2O_2CO_3$	1.2	21.0	12.0
Het-1:0.3	3.3	89.0	7.70
Het-1:0.7	1.6	67.0	2.90
$BiVO_4$	1.4	19.0	2.70

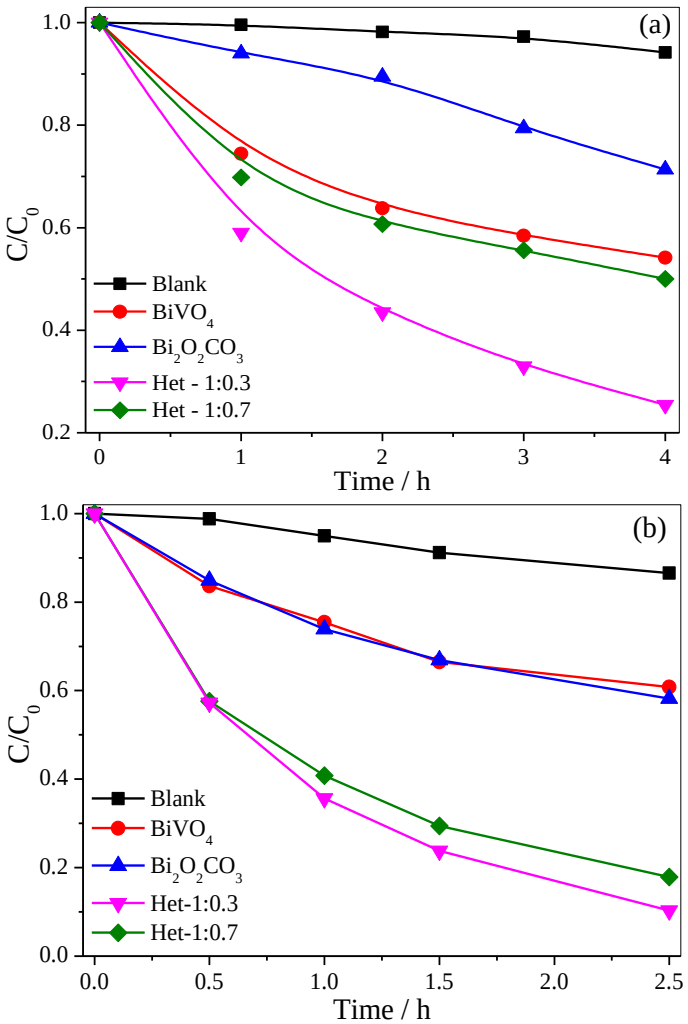

FIGURE 6.7 - MB dye (5 mg L^{-1}) photodegradation curves catalyzed by the isolated phases and the $Bi_2O_2CO_3/BiVO_4$ heterostructures under (a) visible and (b) UV irradiation.

Despite the interesting and promising photocatalytic performance of the $Bi_2O_2CO_3/BiVO_4$ heterostructures, it is necessary that the mechanism involved in the photocatalytic process is elucidated. For this purpose, the $^{\bullet}OH$ radicals were detected using the method proposed by Ishibashi et. al.[104,156] and also studied in great detail by our group.[12,95] In this mechanism, the $^{\bullet}OH$ radical is trapped by TA producing the fluorescent 2-hydroxyterephthalic acid, as illustrated in FIGURE 6.8. The photoactivity of the as-synthesized samples on $^{\bullet}OH$ radical formation followed the order: Het-1:0.3 > $BiVO_4$ > $Bi_2O_2CO_3$. Therefore, the observed trend in the photoactivity of the samples for MB dye degradation was the same as that observed for $^{\bullet}OH$ radical formation, which indicates that an indirect mechanism (i.e., by $^{\bullet}OH$ radical attack) plays a main role on the photoactivity of the as-synthesized heteroestructure.

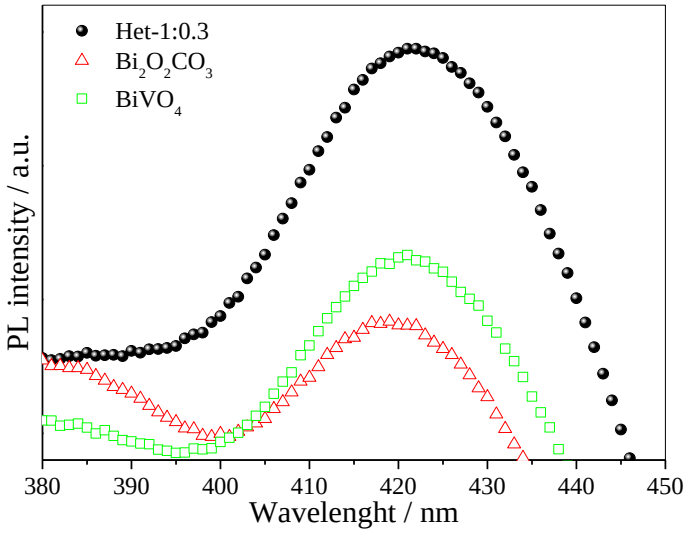

FIGURE 6.8 - PL spectra of 2-hydroxyterephthalic acid formation using pure $Bi_2O_2CO_3$, Het-1:0.3 and $BiVO_4$ photocatalysts after 2h under visible irradiation.

To confirm heterojunction formation and consequent increase in charge carrier lifetime the time resolved photoluminescence (TRPL) measurements of the $BiVO_4$ and Het-1:0.3 samples were performed to find the constant lifetime of the electron/hole pairs (τ). FIGURE 6.9 exhibits the decay of PL intensity monitored at 545 nm and excited by a laser source centered at 405 nm for both samples. The PL decays of all the samples were fitted with a first order exponential function to calculate the lifetime of the electron/hole pair. The PL lifetime of the band-band emission (i.e., the electron/hole pair recombination) for Het-1:0.3 sample was 0.84 ns, while the $BiVO_4$ sample was approximately 0.69 ns, which presents an increase of approximately 18%. These results confirm that the lifetime of the electron/hole pair of heterostructure (Het-1:0.3 sample) is significantly higher than that of the pure $BiVO_4$ phase, proving that the heterojunction between $Bi_2O_2CO_3$ and $BiVO_4$ formed a suitable type-II heterostructure.

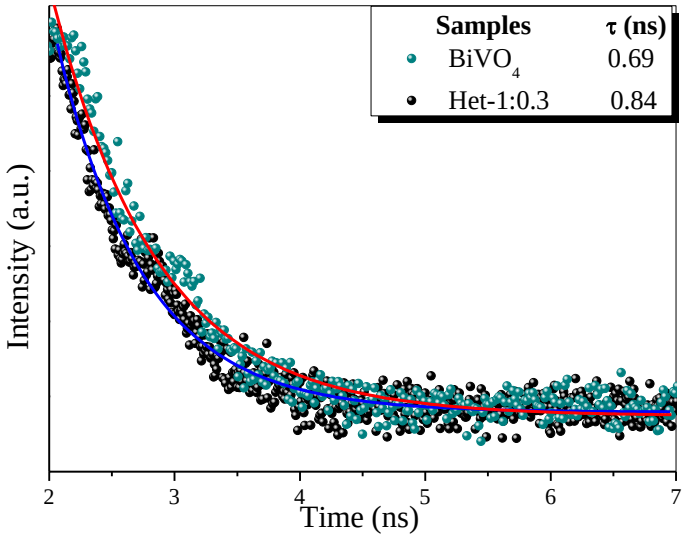

FIGURE 6.9 – TRPL (lifetime decay) curves of the $BiVO_4$ and Het-1:0.3 samples. The powder was excited at 405 nm and photoluminescence was monitored at 545 nm. The lifetime decay curves observed (scatter) and calculated (line).

XPS analysis was performed to investigate the surface composition and chemical state of the elements of the $BiVO_4$, $Bi_2O_2CO_3$ and Het-1:0.7 samples, FIGURE 6.10. From the survey spectra (FIGURE 6.10a), the $BiVO_4$ sample showed the presence of Bi, V, O and C (this was used as an internal reference, 284.8 eV). The $Bi_2O_2CO_3$ and Het-1:0.7 samples showed only the presence of Bi, O and C. The high-resolution spectra of Bi 4f (FIGURE 6.10b) exhibit two strong symmetrical characteristic spin–orbit splitting of Bi 4f peaks at about 158.9 and 164.4 eV, which are assigned to Bi $4f_{7/2}$ and Bi $4f_{5/2}$, respectively.[86,169,174] A shift in Bi 4f peaks was observed from $BiVO_4$ to $Bi_2O_2CO_3$ phase, indicating that Bi atoms are in different chemical environments, however with the same chemical state (Bi^{3+}). The high-resolution spectra of C 1s for the as-synthesized samples (FIGURE 6.10c) showed two peaks located at 284.8 and 288.8 eV, which are ascribed to the carbon reference from the XPS instrument and to the carbonate ion (O-C=O) related to the $Bi_2O_2CO_3$ phase.[86] In this sense, although the XRD data (FIGURE 6.1) showed a typical diffraction pattern of the pure $BiVO_4$ phase, the C 1s XPS results reveal the presence of a small amount of CO_3^{2-} group on the material's surface. The $BiVO_4$ and Het-1:0.3 samples exhibited two peaks of V 2p (FIGURE 6.10d), which are related to the $BiVO_4$ phase, while the $Bi_2O_2CO_3$ sample did not present any peaks related to the V atom. FIGURE 6.10e shows that the high-resolution O 1s spectra of the $Bi_2O_2CO_3$, Het-1:0.3 and $BiVO_4$ samples exhibited three peaks (with different intensities) at 529.6, 530.8, and 531.8 eV, respectively. The shoulder peak at 529.6 eV is

ascribed to the oxygen attached to the Bi–O bond, and the other two peaks at ca. 530.8 and 531.8 eV can be assigned to lattice oxygen and chemisorbed OH and C-O species in $Bi_2O_2CO_3$, respectively.[169] The different intensities for the two peak related to O species are expected for the Het-1:0.3 samples due to the coexistence of both crystalline phases.

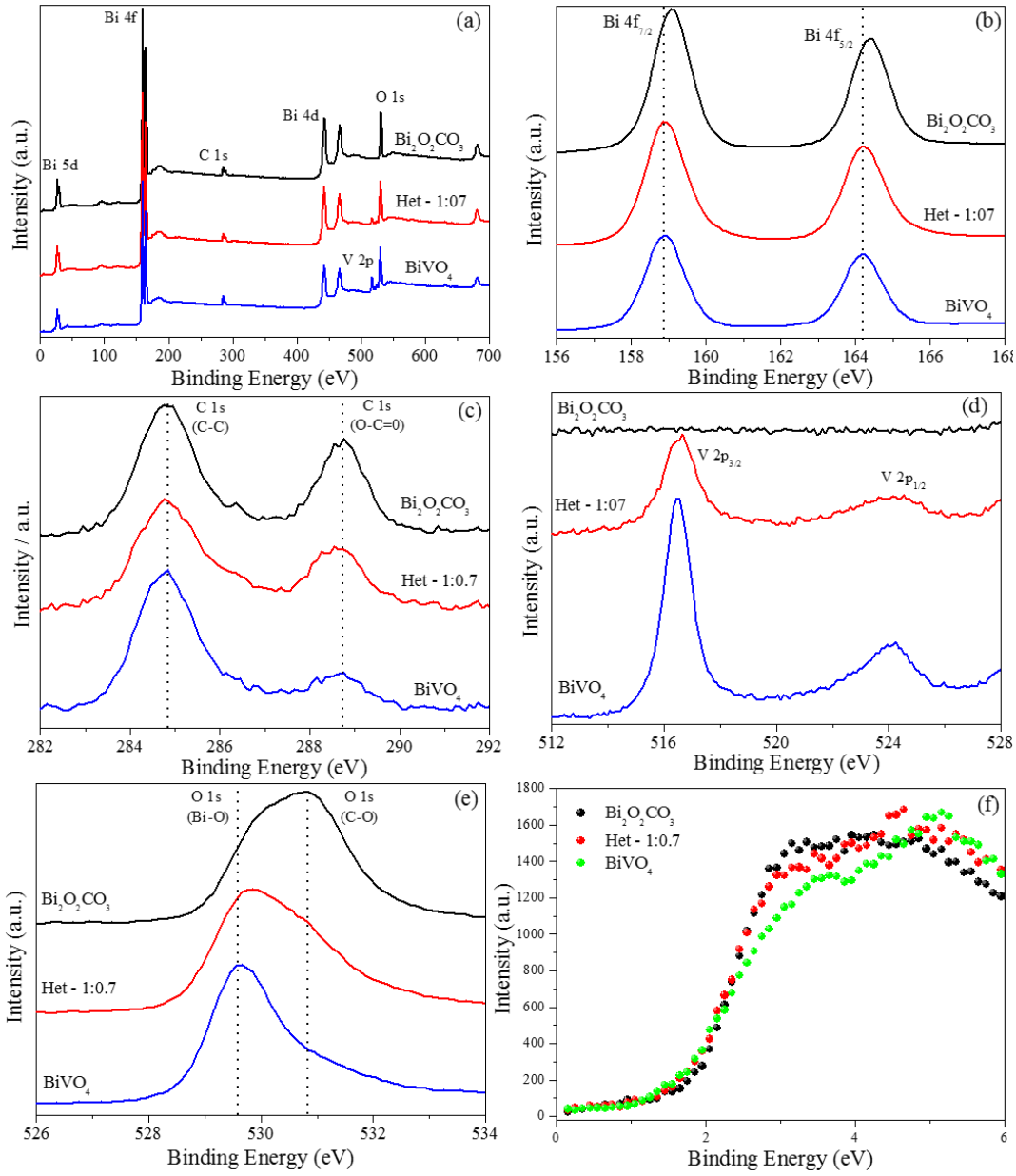

FIGURE 6.10 - X-ray photoelectron spectra of the $BiVO_4$, $Bi_2O_2CO_3$ and Het-1:0.7 samples. (a) Survey spectra, (b) high-resolution spectra of Bi 4f, (c) C 1s, (d) V 2p, (e) O 1s and (f) valence band region.

To determine the valence band (VB) edges of the as-synthesized photocatalysts, the total densities of the VB states of the samples were measured by XPS valence band region (VB-XPS).[177] The conduction band (CB) bottom potentials of the

three samples can be obtained using the equation $E_{CB} = E_{VB} - E_g$. As shown in FIGURE 6.10f, the VB top of $Bi_2O_2CO_3$, $BiVO_4$ and Het-1:0.7 were determined to be 1.8, 1.4, 1.7 eV, respectively. This result indicates that an interfacial structure was formed, and the local environment and electron density of the elements changed to some extent. Therefore, the comparison of the band structures of isolated $Bi_2O_2CO_3$ and $BiVO_4$ samples is shown in FIGURE 6.11a (before contact). On the other hand, when the two semiconductors are in contact FIGURE 6.11b, the CB and VB positions of $Bi_2O_2CO_3$ and $BiVO_4$ change to reach the equilibration of their Fermi levels (E_f).[178–181] Therefore, heterojunction formation allows the diffusion of electrons from the CB of $BiVO_4$ to the CB of $Bi_2O_2CO_3$, while the holes transfer from the VB of $Bi_2O_2CO_3$ to the VB of $BiVO_4$, resulting in an accumulation of electrons in the CB of $Bi_2O_2CO_3$ and holes in the VB of $BiVO_4$. As a matter of fact, the $Bi_2O_2CO_3/BiVO_4$ heterostructures could effectively separate the photogenerated electron/hole pairs and remarkably reduce the recombination of photogenerated charge carrier, as observed by the TRPL and photocatalytic results. Therefore, the $Bi_2O_2CO_3/BiVO_4$ heterostructures exhibit the best photocatalytic activity for the degradation of MB dye under visible and UV irradiation.

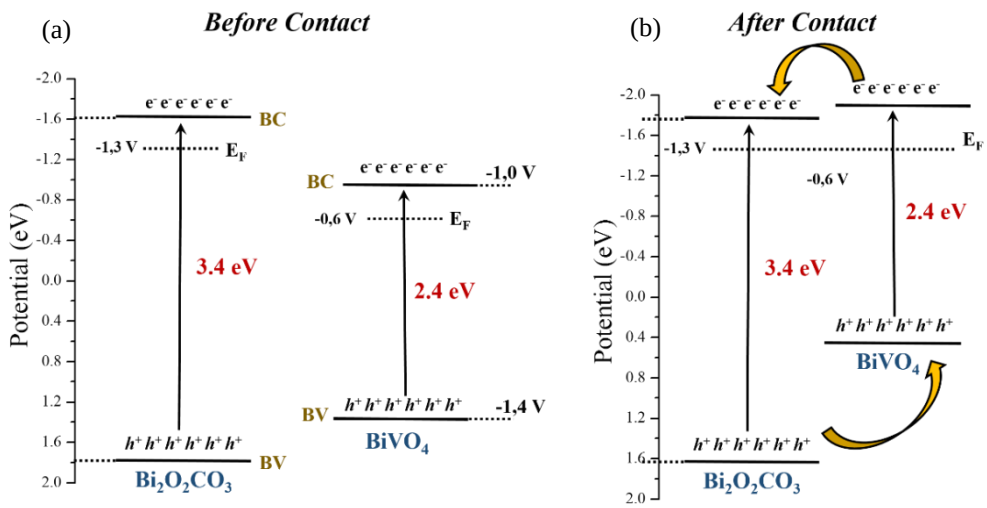

FIGURE 6.11 - Estimated band positions from XPS and DRS results for $Bi_2O_2CO_3$, $BiVO_4$ samples, (a) before and (b) after contact.[178–181]

6.5. - Conclusions

In summary, the method proposed was efficient to obtain $Bi_2O_2CO_3/BiVO_4$ heterostructures with significant enhancement of photocatalytic performance. The formation of the heterostructure was observed indirectly by the great increase in thermal stability of $Bi_2O_2CO_3$ phase when compared to its pure phase. The

heterojunctions formed between $Bi_2O_2CO_3$ and $BiVO_4$ were indicated by HRTEM image. The $Bi_2O_2CO_3/BiVO_4$ heterostructures showed higher photoactivities than their isolated phases (i.e., $Bi_2O_2CO_3$ and $BiVO_4$) for MB degradation under both visible and UV irradiation. The photodegradation of MB dye is caused by the action of $^{\bullet}OH$ radicals, i.e. by an indirect mechanism. The TRPL spectroscopy and XPS results revealed that the formation of the heterostructure led to an effective spatial separation of charge carriers, with consequent increase in lifetime of heterostructure, which confirmed that $Bi_2O_2CO_3/BiVO_4$ is a type-II heterostructure.

7. - General Conclusions

In this thesis it was possible to demonstrate the potentialities of the type-II heterostructure to enhance the photocatalytic properties of $BiVO_4$. In according with the results showed and based in proposed goals it can be concluded that the formation of heterostructures between different phases of the Bi-based semiconductors provides a viable alternative for improving the photocatalytic performance for organic molecules degradation under visible irradiation. Also, other remarks may be highlighted:

- The heterostructure *m*-$BiVO_4$/*t*-$BiVO_4$ is efficient for photoactivity increse due to the formation of a suitable heterojunctions, showing that even different phases of same stoichiometry are enough to form a viable heterostructure; *m*-$BiVO_4$/*t*-$BiVO_4$ heterostructure showed no significant deactivation even after four successive re-uses for MB photodegradation; the primary active species responsible for photodegradation were holes (h^+), superoxide anion radicals ($O_2^{-\bullet}$) and hydroxyl radicals ($^{\bullet}OH$);
- The oxidant peroxide method employed in $BiVO_4$ synthesis was efficient for single phase (monoclinic or tetragonal), as well as for *m*-$BiVO_4$/*t*-$BiVO_4$ heterostructure preparation;
- The *m*-$BiVO_4$ photoactivity was limited by its inability to reduce O_2 to $O_2^{\bullet-}$ (superoxide radical) and trap the electron photogenerated on the conduction band (CB);
- An alternative method to heterojunction formation was proposed, using preformed particles of Bi_2O_3 or $Bi_2O_2CO_3$ to obtain the $Bi_2O_3/BiVO_4$ or $Bi_2O_2CO_3/BiVO_4$ heterostructures, respectively, based on the solubility difference between them.

8. References

1. NAKATA, K. & FUJISHIMA, A. "TiO_2 photocatalysis: design and applications." J. Photochem. Photobiol. C Photochem. Rev., 13 (3): 169, 2012.
2. TONG, H.; OUYANG, S.; BI, Y.; UMEZAWA, N.; OSHIKIRI, M. & YE, J. "Nano-photocatalytic materials: possibilities and challenges." Adv. Mater., 24 (2): 229, 2012.
3. HOFFMANN, M. R.; MARTIN, S. T.; CHOI, W. & BAHNEMANN, D. W. "Environmental applications of semiconductor photocatalysis." Chem. Rev., **95**: 69, 1995.
4. CHATTERJEE, D. & DASGUPTA, S. "Visible light induced photocatalytic degradation of organic pollutants." J. Photochem. Photobiol. C Photochem. Rev., 6 (2-3): 186, 2005.
5. CHEN, X.; SHEN, S.; GUO, L. & MAO, S. S. "Semiconductor-based photocatalytic hydrogen generation". Chem. Rev., **110**: 6503, 2010.
6. BENSAID, S.; CENTI, G.; GARRONE, E.; PERATHONER, S. & SARACCO, G. "Towards artificial leaves for solar hydrogen and fuels from carbon dioxide." ChemSusChem., 5 (3): 500, 2012.
7. LINSEBIGLER, A. L.; LU, G. & YATES, J. T. "Photocatalysis on TiO_2 surfaces: Principles, mechanisms, and selected results." Chem. Rev., 95 (3): 735, 1995.
8. GAYA, U. I. & ABDULLAH, A. H. "Heterogeneous photocatalytic degradation of organic contaminants over titanium dioxide: A review of fundamentals, progress and problems." J. Photochem. Photobiol. C Photochem. Rev., 9 (1): 1, 2008.
9. AUGUGLIARO, V.; BELLARDITA, M.; LODDO, M.; PALMISANO, G.; PALMISANO, L. & YURDAKAL, S. "Overview on oxidation mechanisms of organic compounds by TiO_2 in heterogeneous photocatalysis" J. Photoch. Photobio. C., 13 (3): 224, 2012.
10. FOX, M. & DULAY, M. "Heterogeneous photocatalysis." Chem. Rev., 93 (1): 341, 1993.
11. DE MENDONÇA, V. R. & RIBEIRO, C. "Influence of TiO_2 morphological parameters in dye photodegradation: A comparative study in peroxo-based synthesis." Appl. Catal. B Environ., 105 (3-4): 298, 2011.
12. DE MENDONÇA, V. R.; LOPES, O. F.; FREGONESI, R. P.; GIRALDI, T. R. & RIBEIRO, C. "TiO_2-SnO_2 heterostructures applied to dye photodegradation: The relationship between variables of synthesis and photocatalytic performance." Appl. Surf. Sci., **298**: 182, 2014.
13. FAN, H. J.; LU, C. S.; LEE, W. L. W.; CHIOU, M. R. & CHEN, C. C. "Mechanistic pathways differences between P25-TiO_2 and Pt-TiO_2 mediated CV photodegradation." J. Hazard. Mater., **185**: 227, 2011.
14. DANESHVAR, N.; SALARI, D. & KHATAEE, A. "Photocatalytic degradation of azo dye acid red 14 in water on ZnO as an alternative catalyst to TiO_2." J. Photochem. Photobiol. A Chem., 162 (2-3): 317, 2004.
15. GIRALDI, T. R.; SANTOS, G. V. F.; DE MENDONCA, V. R.; RIBEIRO, C. & WEBER, I. T. "Effect of synthesis parameters on the structural characteristics and photocatalytic activity of ZnO." Mater. Chem. Phys., 136 (2-3): 505, 2012.

16. MILAO, T. M.; DE MENDONÇA, V. R.; ARAÚJO, V. D.; AVANSI, W.; RIBEIRO, C.; LONGO, E. & BERNARDI, M. I. "microwave hydrothermal synthesis and photocatalytic performance of ZnO and M:ZnO nanostructures (M=V, Fe, Co)." Sci. Adv. Mater., 4 (1): 54, 2012.
17. KUMAR, S. G. & RAO, K. S. R. K. "Zinc oxide based photocatalysis: tailoring surface-bulk structure and related interfacial charge carrier dynamics for better environmental applications." RSC Adv., 5 (5): 3306, 2014.
18. MAEDA, K. "Photocatalytic water splitting using semiconductor particles: History and recent developments." J. Photochem. Photobiol. C Photochem. Rev., 12 (4): 237, 2011.
19. YU, J.; QI, L. & JARONIEC, M. "Hydrogen production by photocatalytic water splitting over Pt/TiO_2 nanosheets with exposed (001) facets." J. Phys. Chem. C., 114 (30): 13118, 2010.
20. HENDERSON, M. A. "A surface science perspective on TiO_2 photocatalysis." Surf. Sci. Rep., 66 (6-7): 185, 2011.
21. YU, J. & KUDO, A. "Effects of structural variation on the photocatalytic performance of hydrothermally synthesized $BiVO_4$." Adv. Funct. Mater., 16 (16): 2163, 2006.
22. JANG, J. S.; KIM, H. G. & LEE, J. S. "Heterojunction semiconductors: A strategy to develop efficient photocatalytic materials for visible light water splitting." Catal. Today, 185 (1): 270, 2012.
23. SOARES, G. B.; BRAVIN, B.; VAZ, C. M. P. & RIBEIRO, C. "Facile synthesis of N-doped TiO_2 nanoparticles by a modified polymeric precursor method and its photocatalytic properties." Appl. Catal. B Environ., 106 (3-4): 287, 2011.
24. CAO, J.; XU, B.; LUO, B.; LIN, H. & CHEN, S. "Novel BiOI/BiOBr heterojunction photocatalysts with enhanced visible light photocatalytic properties." Catal. Commun., 13 (1): 63, 2011.
25. PARK, Y.; MCDONALD, K. J. & CHOI, K.-S. "Progress in bismuth vanadate photoanodes for use in solar water oxidation." Chem. Soc. Rev., 42 (6): 2321, 2013.
26. ZHANG, X.; DU, L.; WANG, H.; DONG, X.; ZHANG, X.; MA, C. & MA, H. "Highly ordered mesoporous $BiVO_4$: Controllable ordering degree and super photocatalytic ability under visible light." Microporous Mesoporous Mater., **173**: 175, 2013.
27. OBREGÓN, S.; CABALLERO, A. & COLÓN, G. "Hydrothermal synthesis of $BiVO_4$: Structural and morphological influence on the photocatalytic activity." Appl. Catal. B Environ., **117-118**: 59, 2012.
28. ZHANG, Y.; LI, G.; YANG, X.; YANG, H.; LU, Z. & CHEN, R. "Monoclinic $BiVO_4$ micro-/nanostructures: Microwave and ultrasonic wave combined synthesis and their visible-light photocatalytic activities." J. Alloys Compd., **551**: 544, 2013.
29. GUO, Y.; YANG, X.; MA, F.; LI, K.; XU, L.; YUAN, X. & GUO, Y. "Additive-free controllable fabrication of bismuth vanadates and their photocatalytic activity toward dye degradation." Appl. Surf. Sci., 256 (7): 2215, 2010.
30. YANG, J.; WANG, D.; ZHOU, X. & LI, C. "A theoretical study on the mechanism of photocatalytic oxygen evolution on $BiVO_4$ in aqueous solution." Chem. A. Eur. J., 19 (4): 1320, 2013.

31. LI, R.; ZHANG, F.; WANG, D.; YANG, J.; LI, M.; ZHU, J.; ZHOU, X.; HAN, H. & LI, C. "Spatial separation of photogenerated electrons and holes among {010} and {110} crystal facets of $BiVO_4$." Nat. Commun., **4**: 1432, 2013.
32. ZHOU, L.; WANG, W.; XU, H.; SUN, S. & SHANG, M. "Bi_2O_3 hierarchical nanostructures: controllable synthesis, growth mechanism, and their application in photocatalysis." Chemistry, 15 (7): 1776, 2009.
33. ZHANG, K.; LIU, C.; HUANG, F.; ZHENG, C. & WANG, W. "Study of the electronic structure and photocatalytic activity of the BiOCl photocatalyst." Appl. Catal. B Environ., 68 (3-4), 125–129, 2006.
34. ZHANG, X.; AI, Z.; JIA, F. & ZHANG, L. "Generalized one-pot synthesis, characterization, and photocatalytic activity of hierarchical BiOX (X = Cl, Br, I) nanoplate microspheres." J. Phys. Chem. C., 112 (3): 747, 2008.
35. LI, Y.; WANG, J.; YAO, H.; DANG, L. & LI, Z. "Chemical etching preparation of $BiOI/Bi_2O_3$ heterostructures with enhanced photocatalytic activities." Catal. Commun., 12 (7): 660, 2011.
36. LI, L. & YAN, B. "$BiVO_4/Bi_2O_3$ submicrometer sphere composite: Microstructure and photocatalytic activity under visible-light irradiation." J. Alloys Compd., 476 (1-2): 624, 2009.
37. DE MENDONÇA, V. R.; DALMASCHIO, C. J.; LEITE, E. R.; NIEDERBERGER, M. & RIBEIRO, C. "Heterostructure formation from hydrothermal annealing of preformed nanocrystals." J. Mater. Chem. A, **3**: 2216, 2015.
38. ZHENG, Y.; ZHENG, L.; ZHAN, Y.; LIN, X.; ZHENG, Q. & WEI, K. "Ag/ZnO heterostructure nanocrystals: Synthesis, characterization, and photocatalysis." Inorg. Chem., 46 (17): 6980, 2007.
39. TIAN, J.; ZHAO, Z.; KUMAR, A.; BOUGHTON, R. I. & LIU, H. "Recent progress in design, synthesis, and applications of one-dimensional TiO_2 nanostructured surface heterostructures: a review." Chem. Soc. Rev., 43 (20): 6920, 2014.
40. LIN, D.; WU, H.; ZHANG, R. & PAN, W. "Enhanced photocatalysis of electrospun Ag−ZnO heterostructured nanofibers." Chem. Mater., 21 (15): 3479, 2009.
41. AMIRAV, L. & ALIVISATOS, A. P. "Photocatalytic hydrogen production with tunable nanorod heterostructures." J. Phys. Chem. Lett., 1 (7): 1051, 2010.
42. ZHENG, Y.; CHEN, C.; ZHAN, Y.; LIN, X.; ZHENG, Q.; WEI, K. & ZHU, J. "Photocatalytic activity of Ag/ZnO heterostructure nanocatalyst: Correlation between structure and property." J. Phys. Chem. C, 112 (29): 10773, 2008.
43. LIU, G.; WANG, L.; YANG, H. G.; CHENG, H. M. & LU, G. Q. "Titania-based photocatalysts - crystal growth, doping and heterostructuring." J. Mater. Chem., 20 (5): 831, 2010.
44. FUJISHIMA, A. & HONDA, K. "Electrochemical photolysis of water at a semiconductor electrode." Nature, 238 (5358): 37–38, 1972.
45. TEOH, W. Y.; SCOTT, J. A. & AMAL, R. "Progress in heterogeneous photocatalysis: from classical radical chemistry to engineering nanomaterials and solar reactors." J. Phys. Chem. Lett., 3 (5): 629, 2012.
46. Nogueira, R. F. P. & Jardim, W. F. "Heterogeneous photocatalysis and its environmental applications." Quim. Nova, 21 (1): 69, 1998.

47. GRÄTZEL, M. "Photoelectrochemical cells." Nature, **414**: 338, 2001.
48. WANG, H.; ZHANG, L.; CHEN, Z.; HU, J.; LI, S.; WANG, Z.; LIU, J. & WANG, X. "Semiconductor heterojunction photocatalysts: design, construction, and photocatalytic performances." Chem. Soc. Rev., 43 (15): 5234, 2014.
49. MONIZ, S. J. A.; SHEVLIN, S. A.; MARTIN, D. J.; GUO, Z.-X. & TANG, J. "Visible-light driven heterojunction photocatalysts for water splitting - a critical review." Energy Environ. Sci., 8 (3): 731, 2015.
50. LI, Q.; GUO, B.; YU, J.; RAN, J.; ZHANG, B.; YAN, H. & GONG, J. R. "Highly efficient visible-light-driven photocatalytic hydrogen production of CdS-cluster-decorated graphene nanosheets." J. Am. Chem. Soc., **133**: 10878, 2011.
51. SRIDHARAN, K.; JANG, E. & PARK, T. J. "Novel visible light active graphitic C_3N_4-TiO_2 composite photocatalyst: Synergistic synthesis, growth and photocatalytic treatment of hazardous pollutants." Appl. Catal. B Environ., **142-143**: 718, 2013.
52. WU, G.; THIND, S. S.; WEN, J.; YAN, K. & CHEN, A. "A novel nanoporous α-C_3N_4 photocatalyst with superior high visible light activity." Appl. Catal. B Environ., **142-143**: 590, 2013.
53. SAYAMA, K.; MUKASA, K.; ABE, R.; ABE, Y. & ARAKAWA, H. "A new photocatalytic water splitting system under visible light irradiation mimicking a Z-scheme mechanism in photosynthesis." J. Photochem. Photobiol. A Chem., **148**: 71, 2002.
54. ZOU, Z.; YE, J.; SAYAMA, K. & ARAKAWA, H. "Direct splitting of water under visible light irradiation with an oxide semiconductor photocatalyst." Nature, 414 (2000): 625, 2001.
55. HOU, W.; HUNG, W. H.; PAVASKAR, P.; GOEPPERT, A.; AYKOL, M. & CRONIN, S. B. "Photocatalytic conversion of CO_2 to hydrocarbon fuels via plasmon-enhanced absorption and metallic interband transitions." ACS Catal., **1**: 929, 2011.
56. OBREGÓN, S. & COLÓN, G. "On the different photocatalytic performance of $BiVO_4$ catalysts for Methylene Blue and Rhodamine B degradation." J. Mol. Catal. A Chem., **376**: 40, 2013.
57. WANG, W.; HUANG, X.; WU, S.; ZHOU, Y.; WANG, L.; SHI, H.; LIANG, Y. & ZOU, B. "Preparation of p–n junction $Cu_2O/BiVO_4$ heterogeneous nanostructures with enhanced visible-light photocatalytic activity." Appl. Catal. B Environ., **134-135**: 293, 2013.
58. SUN, S.; WANG, W.; LI, D.; ZHANG, L. & JIANG, D. "Solar light driven pure water splitting on quantum sized $BiVO_4$ without any cocatalyst." ACS Catal., **4**: 3498, 2014.
59. LI, G.; BAI, Y. & ZHANG, W. F. "Difference in valence band top of $BiVO_4$ with different crystal structure." Mater. Chem. Phys., 136 (2-3): 930, 2012.
60. KUDO, A.; OMORI, K. & KATO, H. "A novel aqueous process for preparation of crystal form-controlled and highly crystalline $BiVO_4$ powder from layered vanadates at room temperature and its photocatalytic and photophysical properties." J. Am. Chem. Soc., 121 (14): 11459, 1999.
61. TOKUNAGA, S.; KATO, H. & KUDO, A. "Selective preparation of monoclinic and tetragonal $BiVO_4$ with scheelite structure and their photocatalytic properties." Chem. Mater., 13 (19): 4624, 2001.
62. XI, G. & YE, J. "Synthesis of bismuth vanadate nanoplates with exposed {001} facets

and enhanced visible-light photocatalytic properties." Chem. Commun., 46 (11): 1893, 2010.
63. LIU, W.; YU, Y.; CAO, L.; SU, G.; LIU, X.; ZHANG, L. & WANG, Y. "Synthesis of monoclinic structured $BiVO_4$ spindly microtubes in deep eutectic solvent and their application for dye degradation." J. Hazard. Mater., 181 (1-3): 1102, 2010.
64. KE, D.; PENG, T.; MA, L.; CAI, P. & JIANG, P. "Photocatalytic water splitting for O_2 production under visible-light irradiation on $BiVO_4$ nanoparticles in different sacrificial reagent solutions." Appl. Catal. A Gen., 350 (1): 111, 2008.
65. Chatchai, P.; Murakami, Y.; Kishioka, S.; Nosaka, A. Y. & Nosaka, Y. "Efficient photocatalytic activity of water oxidation over $WO_3/BiVO_4$ composite under visible light irradiation." Electrochim. Acta, 54 (3): 1147, 2009.
66. ALFEROV, Z. I. "Nobel lecture: The double heterostructure concept and its applications in physics, electronics, and technology." Rev. Mod. Phys., 73 (3): 767, 2001.
67. MOURÃO, H. A. J. L.; AVANSI, W. & RIBEIRO, C. "Hydrothermal synthesis of Ti oxide nanostructures and TiO_2:SnO_2 heterostructures applied to the photodegradation of rhodamine B." Mater. Chem. Phys., 135 (2-3): 524, 2012.
68. ZHANG, J.; XU, Q.; FENG, Z.; LI, M. & LI, C. "Importance of the relationship between surface phases and photocatalytic activity of TiO_2." Angew. Chem. Int. Ed. Engl., 47 (9): 1766, 2008.
69. KONG, L.; JIANG, Z.; LAI, H. H.; NICHOLLS, R. J.; XIAO, T.; JONES, M. O. & EDWARDS, P. P. "Unusual reactivity of visible-light-responsive AgBr–BiOBr heterojunction photocatalysts." J. Catal., **293**: 116–125, 2012.
70. WANG, Y.; WANG, Q.; ZHAN, X.; WANG, F.; SAFDAR, M. & HE, J. "Visible light driven type II heterostructures and their enhanced photocatalysis properties: a review." Nanoscale, 5 (18): 8326, 2013.
71. SHI, X.; HERRAIZ-CARDONA, I.; BERTOLUZZI, L.; LOPEZ-VARO, P.; BISQUERT, J.; PARK, J. H. & GIMENEZ, S. "Understanding the synergistic effect of WO_3 –$BiVO_4$ heterostructures by impedance spectroscopy." Phys. Chem. Chem. Phys., 18 (13): 9255, 2016.
72. ZHANG, J.; REN, F.; DENG, M. & WANG, Y. "Enhanced visible-light photocatalytic activity of a g-$C_3N_4/BiVO_4$ nanocomposite: a first-principles study." Phys. Chem. Chem. Phys., **17**: 10218, 2015.
73. TIAN, Y.; CHANG, B.; YANG, Z.; ZHOU, B.; XI, F. & DONG, X. "Graphitic carbon nitride–$BiVO_4$ heterojunctions: simple hydrothermal synthesis and high photocatalytic performances." RSC Adv., 4 (8): 4187, 2014.
74. RESASCO, J.; ZHANG, H.; KORNIENKO, N.; BECKNELL, N.; LEE, H.; GUO, J.; BRISENO, A. L. & YANG, P. "$TiO_2/BiVO_4$ nanowire heterostructure photoanodes based on type II band alignment." ACS Cent. Sci., 2 (2): 80, 2016.
75. HU, Y.; LI, D.; ZHENG, Y.; CHEN, W.; HE, Y.; SHAO, Y.; FU, X. & XIAO, G. "$BiVO_4/TiO_2$ nanocrystalline heterostructure: A wide spectrum responsive photocatalyst towards the highly efficient decomposition of gaseous benzene." Appl. Catal. B Environ., 104 (1-2): 30, 2011.
76. YAN, L.; ZHAO, W. & LIU, Z. "1D ZnO/$BiVO_4$ heterojunction photoanodes for efficient photoelectrochemical water splitting." Dalt. Trans., 45 (28): 11346, 2016.

77. LONG, M.; CAI, W. & KISCH, H. "Visible light induced photoelectrochemical properties of *n*-$BiVO_4$ and *n*-$BiVO_4$/p-Co_3O_4." J. Phys. Chem. C, 112 (3): 548, 2008.
78. LOPES, O. F.; CARVALHO, K. T. G.; MACEDO, G. K.; DE MENDONÇA, V. R.; AVANSI, W. & RIBEIRO, C. "Synthesis of $BiVO_4$ via oxidant peroxo-method: insights into the photocatalytic performance and degradation mechanism of pollutants." New J. Chem., 39 (8): 6231, 2015.
79. ZHANG, L.; WANG, W.; YANG, J.; CHEN, Z.; ZHANG, W.; ZHOU, L. & LIU, S. "Sonochemical synthesis of nanocrystallite Bi_2O_3 as a visible-light-driven photocatalyst." Appl. Catal. A Gen., **308**: 105, 2006.
80. HU, R.; XIAO, X.; TU, S.; ZUO, X. & NAN, J. "Synthesis of flower-like heterostructured β-Bi_2O_3/$Bi_2O_2CO_3$ microspheres using $Bi_2O_2CO_3$ self-sacrifice precursor and its visible-light-induced photocatalytic degradation of o-phenylphenol." Appl. Catal. B Environ., **163**: 510, 2015.
81. OHTANI, B.; PRIETO-MAHANEY, O. O.; LI, D. & ABE, R. "What is Degussa (Evonic) P25? Crystalline composition analysis, reconstruction from isolated pure particles and photocatalytic activity test." J. Photochem. Photobiol. A Chem., **216**: 179, 2010.
82. TAN, G.; ZHANG, L.; REN, H.; WEI, S.; HUANG, J. & XIA, A. "Effects of pH on the hierarchical structures and photocatalytic performance of $BiVO_4$ powders prepared via the microwave hydrothermal method." ACS Appl. Mater. Interfaces, **5**: 5186–5193, 2013.
83. OBREGON, S.; LEE, S. W. & COLON, G. "Exalted photocatalytic activity of tetragonal $BiVO_4$ by Er^{3+} doping through a luminescence cooperative mechanism." Dalt. Trans., **43**: 311, 2014.
84. USAI, S.; OBREGON, S.; BECERRO, A. I. & COLON, G. "Monoclinic − tetragonal heterostructured $BiVO_4$ by Yttrium doping with improved photocatalytic activity". J. Phys. Chem. C, 117 (46): 24479, 2013.
85. XUE, Y. & WANG, X. "The effects of Ag doping on crystalline structure and photocatalytic properties of $BiVO_4$." Int. J. Hydrogen Energy, 40 (17): 5878, 2015.
86. MADHUSUDAN, P.; RAN, J.; ZHANG, J.; YU, J. & LIU, G. "Novel urea assisted hydrothermal synthesis of hierarchical $BiVO_4$/$Bi_2O_2CO_3$ nanocomposites with enhanced visible-light photocatalytic activity." Appl. Catal. B Environ., **110**: 286, 2011.
87. LI, K.; XU, Y.; HE, Y.; YANG, C.; WANG, Y. & JIA, J. "Photocatalytic fuel cell (PFC) and dye self-photosensitization photocatalytic fuel cell (DSPFC) with BiOCl/Ti photoanode under UV and visible light irradiation." Environ. Sci. Technol., 47 (7): 3490, 2013.
88. JIANG, H.-Y.; LI, P.; LIU, G.; YE, J. & LIN, J. "Synthesis and photocatalytic properties of metastable β-Bi_2O_3 stabilized by surface-coordination effects." J. Mater. Chem. A, 3 (9): 5119, 2015.
89. LIANG, N.; ZAI, J.; XU, M.; ZHU, Q.; WEI, X. & QIAN, X. "Novel Bi_2S_3/$Bi_2O_2CO_3$ heterojunction photocatalysts with enhanced visible light responsive activity and wastewater treatment." J. Mater. Chem. A, **2**: 4208, 2014.
90. HAMROUNI, A.; MOUSSA, N.; DI PAOLA, A.; PALMISANO, L.; HOUAS, A. & PARRINO, F. "Photocatalytic activity of binary and ternary SnO_2–ZnO–$ZnWO_4$

nanocomposites." J. Photochem. Photobiol. A Chem., **309**: 47, 2015.
91. DE CASTRO, I. A.; AVANSI, W. & RIBEIRO, C. "WO_3/TiO_2 heterostructures tailored by the oriented attachment mechanism: insights from their photocatalytic properties." CrystEngComm., 16 (8): 1514, 2014.
92. CHEN, L.; ZHANG, Q.; HUANG, R.; YIN, S. F.; LUO, S. L. & AU, C. T. "Porous peanut-like Bi_2O_3-$BiVO_4$ composites with heterojunctions: one-step synthesis and their photocatalytic properties." Dalton Trans., 41 (31): 9513, 2012.
93. MOURÃO, H. A. J. L.; DE MENDONÇA, V. R.; MALAGUTTI, A. R. & RIBEIRO, C. "Nanoestruturas em fotocatálise: uma revisão sobre estratégias de síntese de fotocatalisadores em escala nanométrica." Quim. Nova, 32 (8): 2181, 2009.
94. PIQUEMAL, J. Y.; BRIOT, E. & BRÉGEAULT, J. M. "Preparation of materials in the presence of hydrogen peroxide: from discrete or "zero-dimensional" objects to bulk materials." Dalt. Trans., 42 (1): 29, 2013.
95. LOPES, O. F.; PARIS, E. C. & RIBEIRO, C. "Synthesis of Nb_2O_5 nanoparticles through the oxidant peroxide method applied to organic pollutant photodegradation: A mechanistic study." Appl. Catal. B Environ., **144**: 800, 2014.
96. YOSHIMURA, M. & BYRAPPA, K. "Hydrothermal processing of materials: past, present and future." J. Mater. Sci., 43 (7): 2085, 2008.
97. YE, K. H.; YU, X.; QIU, Z.; ZHU, Y.; LU, X. & ZHANG, Y. "Facile synthesis of bismuth oxide/bismuth vanadate heterostructures for efficient photoelectrochemical cells." RSC Adv., 5 (43): 34152, 2015.
98. CHENG, Y.; WANG, H.; ZHU, Y.; LIAO, F.; LI, Z. & LI, J. "One-step hydrothermal synthesis of $BiVO_4$–Bi_2O_3 p–n heterojunction composites and their enhanced photocatalysis properties." J. Mater. Sci. Mater. Electron., 26 (2): 1268, 2015.
99. DE-KUN, M.; GUAN, M.; LIU, S.; ZHANG, Y.; ZHANG, C.; HE, Y. & HUANG, S. "Controlled synthesis of olive-shaped $Bi_2S_3/BiVO_4$ microspheres through a limited chemical conversion route and enhanced visible-light-responding photocatalytic activity." Dalt. Trans., **41**: 5581, 2012.
100. MOURÃO, H. A. J. L.; LOPES, O. F.; RIBEIRO, C. & MASTELARO, V. R. Rapid hydrothermal synthesis and pH-dependent photocatalysis of strontium titanate microspheres. Mater. Sci. Semicond. Process., **30**: 651, 2015.
101. CAVALCANTE, L. S.; SCZANCOSKI, J. C.; BATISTA, N. C.; LONGO, E.; VARELA, J. A. & ORLANDI, M. O. "Growth mechanism and photocatalytic properties of $SrWO_4$ microcrystals synthesized by injection of ions into a hot aqueous solution." Adv. Powder Technol., 24 (1): 344, 2013.
102. CHENG, H.; HUANG, B.; LU, J.; WANG, Z.; XU, B.; QIN, X.; ZHANG, X. & DAI, Y. "Synergistic effect of crystal and electronic structures on the visible-light-driven photocatalytic performances of Bi_2O_3 polymorphs." Phys. Chem. Chem. Phys., **12**: 15468, 2010.
103. LI, Y.; WANG, J.; YAO, H.; DANG, L. & LI, Z. "Efficient decomposition of organic compounds and reaction mechanism with BiOI photocatalyst under visible light irradiation." J. Mol. Catal. A Chem., 334 (1-2): 116, 2011.
104. ISHIBASHI, K. & FUJISHIMA, A. "Quantum yields of active oxidative species formed on TiO_2 photocatalyst." J. Photochem. Photobiol. A Chem., **134**: 139, 2000.

105. ISHIBASHI, K. & FUJISHIMA, A. "Detection of active oxidative species in TiO_2 photocatalysis using the fluorescence technique." Electrochem. Comun., **2**: 207, 2000.
106. AVANSI, W.; RIBEIRO, C.; LEITE, E. R. & MASTELARO, V. R. "Vanadium pentoxide nanostructures: an effective control of morphology and crystal structure in hydrothermal conditions." Cryst. Growth Design, 9 (8): 3626, 2009.
107. MURPHY, A. B. "Band-gap determination from diffuse reflectance measurements of semiconductor films, and application to photoelectrochemical water-splitting." Sol. Energy Mater. Sol. Cells, **91**: 1326, 2007.
108. LIN, X.; LI, H.; YU, L.; ZHAO, H.; YAN, Y.; LIU, C. & ZHAI, H. "Efficient removal rhodamine B over hydrothermally synthesized fishbone like $BiVO_4$." Mater. Res. Bull., 48 (10): 4424, 2013.
109. ZHANG, X.; AI, Z.; JIA, F.; ZHANG, L.; FAN, X. & ZOU, Z. "Selective synthesis and visible-light photocatalytic activities of $BiVO_4$ with different crystalline phases." Mater. Chem. Phys., 103 (1): 162, 2007.
110. PRADO, A. G. S.; BOLZON, L. B.; PEDROSO, C. P.; MOURA, A. O. & COSTA, L. L. "Nb_2O_5 as efficient and recyclable photocatalyst for indigo carmine degradation." Appl. Catal. B Environ., 82 (3-4): 219, 2008.
111. CAVALCANTE, L. S.; BATISTA, F. M. C.; ALMEIDA, M. A. P.; RABELO, A. C.; NOGUEIRA, I. C.; BATISTA, N. C.; VARELA, J. A.; SANTOS, M. R. M. C.; LONGO, E. & SIU LI, M. "Structural refinement, growth process, photoluminescence and photocatalytic properties of $(Ba_{1-x}Pr_{2x/3})WO_4$ crystals synthesized by the coprecipitation method." RSC Adv., **2**: 6438, 2012.
112. LOPES, O.F; DE MENDONÇA, V. R.; SILVA, F.; PARIS, E. & RIBEIRO, C. "Óxidos de nióbio: uma visão sobre a síntese do Nb_2O_5 e sua aplicação em fotocatálise heterogênea." Quim. Nova, 38 (1): 106, 2015.
113. LEE, W. W.; LU, C. S.; CHUANG, C. W.; CHEN, Y. J.; FU, J. Y.; SIAO, C. W. & CHEN, C. C. "Synthesis of bismuth oxyiodides and their composites: characterization, photocatalytic activity, and degradation mechanisms." RSC Adv., **5**: 23450, 2015.
114. JIANG, Y. R.; CHOU, S. Y.; CHANG, J. L.; HUANG, S. T.; LIN, H. P. & CHEN, C. C. "Hydrothermal synthesis of bismuth oxybromide–bismuth oxyiodide composites with high visible light photocatalytic performance for the degradation of CV and phenol." RSC Adv., **5**: 30851, 2015.
115. HUANG, S. T.; JIANG, Y. R.; CHOU, S. Y.; DAI, Y.M. & CHEN, C. C. "Synthesis, characterization, photocatalytic activity of visible-light-responsive photocatalysts BiO_xCl_y/BiO_mBr_n by controlled hydrothermal method." J. Mol. Catal. A Chem., **391**: 105, 2014.
116. JIANG, Y. R.; LIN, H. P.; CHUNG, W. H.; DAI, Y. M.; LIN, W. Y. & CHEN, C. C. "Controlled hydrothermal synthesis of BiO_xCl_y/BiO_mI_n composites exhibiting visible-light photocatalytic degradation of crystal violet." J. Hazard. Mater., **283**: 787, 2015.
117. YIN, M.; LI, Z.; KOU, J. & ZOU, Z. "Mechanism investigation of visible light-induced degradation in a heterogeneous TiO_2/Eosin Y/Rhodamine B system." Environ. Sci. Technol., 43 (21): 8361, 2009.
118. ZHAO, Y.; ELEY, C.; HU, J.; FOORD, J. S.; YE, L.; HE, H. & TSANG, S. C. E. "Shape-dependent acidity and photocatalytic activity of Nb_2O_5 nanocrystals with an

active TT (001) surface." Angew. Chemie Int. Ed., 51 (16): 3846, 2012.
119. WEI, W.; YUE, X.; CUI, H.; LÜ, X. & XIE, J. "Hydrothermal synthesis and properties of $BiVO_4$ photocatalysts." J. Mater. Res., 28 (24): 3408, 2013.
120. LEI, B.-X.; ZHANG, P.; WANG, S.-N.; LI, Y.; HUANG, G.-L.; SUN, Z.-F. "Additive-free hydrothermal synthesis of novel bismuth vanadium oxide dendritic structures as highly efficient visible-light photocatalysts." Mater. Sci. Semicond. Process.**30**: 429, 2015.
121. LOPES, O. F.; CARVALHO, K. T. G.; MACEDO, G. K.; DE MENDONÇA, V. R.; AVANSI, W. & RIBEIRO, C. "Synthesis of $BiVO_4$ via oxidant peroxo-method: Insights into the photocatalytic performance and degradation mechanism of pollutants." New J. Chem., 39 (8): 6231, 2015.
122. YE, L.; LIU, J.; GONG, C.; TIAN, L.; PENG, T. & ZAN, L. "Two different roles of metallic Ag on Ag/AgX/BiOX (X = Cl, Br) visible light photocatalysts: Surface plasmon resonance and Z-Scheme bridge." ACS Catal., **2**: 1677, 2012.
123. YANG, X.; CUI, H.; LI, Y.; QIN, J.; ZHANG, R. & TANG, H. "Fabrication of Ag_3PO_4-graphene composites with highly efficient and stable visible light photocatalytic performance." ACS Catal., **3**: 363, 2013.
124. PILLI, S. K.; FURTAK, T. E.; BROWN, L. D.; DEUTSCH, T. G.; TURNER, J. A. & HERRING, A. M. "Cobalt-phosphate (Co-Pi) catalyst modified Mo-doped $BiVO_4$ photoelectrodes for solar water oxidation." Energy Environ. Sci., **4**: 5028, 2011.
125. ZHANG, A. & ZHANG, J. "Effects of europium doping on the photocatalytic behavior of $BiVO_4$." J. Hazard. Mater., **173**: 265, 2010.
126. ZHOU, F.; MIN, Y.; FAN, J. & XU, Q. "Reduced graphene oxide-grafted cylindrical like W doped $BiVO_4$ hybrids with enhanced performances for photocatalytic applications." Chem. Eng. J., **266**: 48, 2015.
127. ZHANG, A. & ZHANG, J. "Synthesis and characterization of Ag/$BiVO_4$ composite photocatalyst." Appl. Surf. Sci., **256**: 3224, 2010.
128. LIN, F.; WANG, D.; JIANG, Z.; MA, Y.; LI, J.; LI, R. & LI, C. "Photocatalytic oxidation of thiophene on $BiVO_4$ with dual co-catalysts Pt and RuO_2 under visible light irradiation using molecular oxygen as oxidant." Energy Environ. Sci., **5**: 6400, 2012.
129. YANG, J.; WANG, D.; HAN, H. & LI, C. "Roles of cocatalysts in photocatalysis and photoelectrocatalysis." Acc. Chem. Res., 46 (8): 1900, 2013.
130. FAN, H.; JIANG, T.; LI, H.; WANG, D.; WANG, L.; ZHAI, J.; HE, D.; WANG, P. & XIE, T. "Effect of $BiVO_4$ crystalline phases on the photoinduced carriers behavior and photocatalytic activity." J. Phys. Chem. C, **116**: 2425, 2012.
131. AVANSI, W.; DE MENDONÇA, V. R.; LOPES, O. F. & RIBEIRO, C. "Vanadium pentoxide 1-D nanostructures applied to dye removal from aqueous systems by coupling adsorption and visible-light photodegradation." RSC Adv., **5**: 12000, 2015.
132. CAMARGO, E. R.; DANCINI, M. G. & KAKIHANA, M. "The oxidant peroxo method (OPM) as a new alternative for the synthesis of lead-based and bismuth-based oxides." J. Mater. Res., **29**: 131, 2014.
133. MOURÃO, H. A. J. L.; LOPES, O. F; MALAGUTTI, A. R; PARIS, E. C. & RIBEIRO, C. "Hydrothermal synthesis and photocatalytic properties of anatase TiO_2 nanocrystals obtained from peroxytitanium complex precursor." Mater. Sci. Semicond.

Process., **25**: 320, 2014.
134. AVANSI, W.; ARENAL, R.; DE MENDONÇA, V. R.; RIBEIRO, C. & LONGO, E. "Vanadium-doped TiO_2 anatase nanostructures: the role of V in solid solution formation and its effect on the optical properties." CrystEngComm., **16**: 5021, 2014.
135. AVANSI, W.; RIBEIRO, C.; LEITE, E. R. & MASTELARO, V. R. "An efficient synthesis route of $Na_2V_6O_{16}nH_2O$ nanowires in hydrothermal conditions." Mater. Chem. Phys., 127 (1-2): 56, 2011.
136. NAG, M.; GHOSH, S.; RANA, R. K. & MANORAMA, S. V. "Controlling phase, crystallinity, and morphology of titania nanoparticles with peroxotitanium complex: Experimental and theoretical insights." J. Phys. Chem. Lett., **1**: 2881, 2010.
137. YU, J.; KUDO, A. "Effects of Structural Variation on the Photocatalytic Performance of Hydrothermally Synthesized $BiVO_4$." Adv. Funct. Mater. 16 (16): 2163, 2006.
138. DE MENDONÇA, V. R.; MOURÃO, H. A. J. L.; MALAGUTTI, A. R. & RIBEIRO, C. "The role of the relative dye/photocatalyst concentration in TiO 2 assisted photodegradation process." Photochem. Photobiol., **90**: 66, 2014.
139. CAO, Y.; HE, T.; CHEN, Y. & CAO, Y. "Fabrication of rutile TiO_2-Sn/Anatase TiO_2-N heterostructure and its application in visible-light photocatalysis." J. Phys. Chem. C, **114**: 3627, 2010.
140. GUOHUI, T.; HONGGANG, F.; LIQIANG, J.; BAIFU, X. & KAI, P. "Preparation and characterization of stable biphase TiO_2 photocatalyst with high crystallinity, large surface area, and enhanced photoactivity." J. Phys. Chem. C, **112**: 3083, 2008.
141. DING, Z.; LU, G. Q. & GREENFIELD, P. F. "Role of the crystallite phase of TiO_2 in heterogeneous photocatalysis for phenol oxidation in water." J. Phys. Chem. B, **104**: 4815, 2000.
142. HURUM, D. C.; AGRIOS, A. G.; GRAY, K. A.; RAJH, T. & THURNAUER, M. C. "Explaining the enhanced photocatalytic activity of Degussa P25 mixed-phase TiO_2 using EPR." J. Phys. Chem. B, **107**: 4545, 2003.
143. DING, K.; CHEN, B.; FANG, Z. & ZHANG, Y. "Density functional theory study on the electronic and optical properties of three crystalline phases of $BiVO_4$." Theor. Chem. Acc., **132**: 1, 2013.
144. CAI, J.; ZHU, Y.; LIU, D.; MENG, M.; HU, Z. & JIANG, Z. "Synergistic effect of titanate-anatase heterostructure and hydrogenation-induced surface disorder on photocatalytic water splitting." ACS Catal., 5 (3): 1708, 2015.
145. MERUPO, V. I.; VELUMANI, S.; ORDON, K.; ERRIEN, N.; SZADE, J. & KASSIBA, A. H. "Structural and optical characterization of ball-milled copper-doped bismuth vanadium oxide ($BiVO_4$)." CrystEngComm., **17**: 3366, 2015.
146. WANG, M.; ZHENG, H.; LIU, J.; DONG, D.; CHE, Y. & YANG, C. "Enhanced visible-light-driven photocatalytic activity of B-doped $BiVO_4$ synthesized using a corn stem template." Mater. Sci. Semicond. Process., **30**: 307, 2015.
147. ZHANG, L.; LONG, J.; PAN, W.; ZHOU, S.; ZHU, J.; ZHAO, Y.; WANG, X. & CAO, G. "Efficient removal of methylene blue over composite-phase $BiVO_4$ fabricated by hydrothermal control synthesis." Mater. Chem. Phys., 136 (2-3): 897, 2012.
148. SUBRAMANIAN, V.; WOLF, E. & KAMAT, P. "Green emission to probe

photoinduced charging events in ZnO-Au nanoparticles. Charge distribution and Fermi-level equilibration." J. Phys. C, **107**: 7479, 2003.
149. KUDO, A. & MISEKI, Y. "Heterogeneous photocatalyst materials for water splitting." Chem. Soc. Rev., 38 (1): 253, 2009.
150. ABOU EL-NOUR, K. M. M.; EFTAIHA, A.; AL-WARTHAN, A. & AMMAR, R. A. A. "Synthesis and applications of silver nanoparticles." Arab. J. Chem., 3 (3): 135, 2010.
151. RAMALHO, T. C.; OLIVEIRA, L. C. A.; CARVALHO, K. T. G.; SOUZA, E. F.; CUNHA, E. F. F. & NAZZARO, M. "Catalytic behavior of niobia species on oxidation reactions: insights from experimental and theoretical models." J. Mater. Sci., 43 (17): 5982, 2008.
152. RAMALHO, T. C.; OLIVEIRA, L. C. A.; CARVALHO, K. T. G.; SOUZA, E. F.; DA CUNHA, E. F. F. & NAZZARO, M. "The molecular basis for the behaviour of niobia species in oxidation reaction probed by theoretical calculations and experimental techniques." Mol. Phys., 107 (2): 171, 2009.
153. CARVALHO, K. T. G.; SILVA, A. C.; OLIVEIRA, L. C. A.; GONCALVES, M. & MAGRIOTIS, Z. M. "Modified synthetic niobia as catalyst in the oxidation of organic dye: utilization of H_2O_2 and atmospheric O_2 as oxidants." Quim. Nova, 32 (6): 1373, 2009.
154. TIRELI, A. A.; GUIMARÃES, I. D. R.; TERRA, J. C. D. S.; DA SILVA, R. R. & GUERREIRO, M. C. "Fenton-like processes and adsorption using iron oxide-pillared clay with magnetic properties for organic compound mitigation." Environ. Sci. Pollut. Res. Int., 22 (2): 870, 2015.
155. ZHANG, T.; OYAMA, T.; AOSHIMA, A.; HIDAKA, H.; ZHAO, J. & SERPONE, N. "Photooxidative N-demethylation of methylene blue in aqueous TiO_2 dispersions under UV irradiation." J. Photochem. Photobiol. A Chem., **140**: 163, 2001.
156. ISHIBASHI, K.; FUJISHIMA, A.; WATANABE, T. & HASHIMOTO, K. "Detection of active oxidative species in TiO_2 photocatalysis using the fluorescence technique." Electrochem. Comun., **2**: 207, 2000.
157. DE CASTRO, I. A.; DE OLIVEIRA, J. A.; PARIS, E. C.; GIRALDI, T. R. & RIBEIRO, C. "Production of heterostructured TiO_2/WO_3 Nanoparticulated photocatalysts through a simple one pot method." Ceram. Int., 41 (3): 3502, 2015.
158. LIU, Y.; GU, Y.; YAN, X.; KANG, Z.; LU, S.; SUN, Y. & ZHANG, Y. "Design of sandwich-structured ZnO/ZnS/Au photoanode for enhanced efficiency of photoelectrochemical water splitting." Nano Res., 8 (9): 2891, 2015.
159. WU, M.; CHEN, W.; SHEN, Y.; HUANG, F.; LI, C. & LI, S. "In situ growth of matchlike ZnO/Au plasmonic heterostructure for enhanced photoelectrochemical water splitting." ACS Appl. Mater. Interfaces, **6**: 15052, 2014.
160. MALARA, F.; MINGUZZI, A.; MARELLI, M.; MORANDI, S.; PSARO, R.; DAL SANTO, V. & NALDONI, A. "α-Fe_2O_3/NiOOH: An effective heterostructure for photoelectrochemical water oxidation." ACS Catal., 5 (9): 5292, 2015.
161. LI, X.; LIU, H.; LUO, D.; LI, J.; HUANG, Y.; LI, H.; FANG, Y.; XU, Y. & ZHU, L. "Adsorption of CO_2 on heterostructure $CdS(Bi_2S_3)/TiO_2$ nanotube photocatalysts and their photocatalytic activities in the reduction of CO_2 to methanol under visible light

irradiation." Chem. Eng. J., **180**: 151, 2012.
162. EHSAN, M. F. & HE, T. "In situ synthesis of ZnO/ZnTe common cation heterostructure and its visible-light photocatalytic reduction of CO_2 into CH_4." Appl. Catal. B Environ., **166-167**: 345, 2015.
163. TAN, L. L.; ONG, W. J.; CHAI, S. P.; GOH, B. T. & MOHAMED, A. R. "Visible-light-active oxygen-rich TiO_2 decorated 2D graphene oxide with enhanced photocatalytic activity toward carbon dioxide reduction." Appl. Catal. B Environ., **179**: 160, 2015.
164. WANG, J.; JI, G.; LIU, Y.; GONDAL, M. A. & CHANG, X. "Cu_2O/TiO_2 heterostructure nanotube arrays prepared by an electrodeposition method exhibiting enhanced photocatalytic activity for CO_2 reduction to methanol." Catal. Commun., **46**: 17, 2014.
165. DENISOV, V. N.; IVLEV, A. N.; LIPIN, A. S.; MAVRIN, B. N. & ORLOV, V. G. "Raman spectra and lattice dynamics of single-crystal alpha-Bi_2O_3." J. Phys. Condens. Matter., **9**: 4967, 1997.
166. HO, C.; CHAN, C.; HUANG, Y. & TIEN, L. "The study of optical band edge property of bismuth oxide nanowires α-Bi_2O_3." Opt. Express, 21 (10): 9658, 2013.
167. MADHUSUDAN, P.; ZHANG, J.; CHENG, B. & LIU, G. "Photocatalytic degradation of organic dyes with hierarchical $Bi_2O_2CO_3$ microstructures under visible-light." CrystEngComm., 15 (2): 231, 2013.
168. TIAN, J.; ZHAO, Z.; KUMAR, A.; BOUGHTON, R. I. & LIU, H. "Recent progress in design, synthesis, and applications of one-dimensional TiO_2 nanostructured surface heterostructures: a review." Chem. Soc. Rev., 43 (20): 6920, 2014.
169. HE, Y.; WANG, Y.; ZHANG, L.; TENG, B. & FAN, M. "High-efficiency conversion of CO_2 to fuel over ZnO/g-C_3N_4 photocatalyst." Appl. Catal. B Environ., **168**: 1, 2015.
170. LEI, J.; CHEN, Y.; SHEN, F.; WANG, L.; LIU, Y. & ZHANG, J. "Surface modification of TiO_2 with g-C_3N_4 for enhanced {UV} and visible photocatalytic activity." J. Alloys Compd., **631**: 328, 2015.
171. ZHU, S.; LIANG, S.; GU, Q.; XIE, L.; WANG, J.; DING, Z. & LIU, P. "Effect of Au supported TiO_2 with dominant exposed {001} facets on the visible-light photocatalytic activity." Applied Catal. B, Environ., **119-120**: 146, 2012.
172. ZHENG, X.; LI, D.; LI, X.; CHEN, J.; CAO, C.; FANG, J.; WANG, J.; HE, Y. & ZHENG, Y. "Construction of ZnO/TiO_2 photonic crystal heterostructures for enhanced photocatalytic properties." Appl. Catal. B Environ., **168–169**: 408, 2015.
173. DE MENDONÇA, V. R.; LOPES, O. F.; FREGONESI, R. P.; GIRALDI, T. R. & RIBEIRO, C. "TiO_2-SnO_2 heterostructures applied to dye photodegradation: The relationship between variables of synthesis and photocatalytic performance." Appl. Surf. Sci., **298**: 182, 2014.
174. LOPES, O. F.; CARVALHO, K. T. G.; NOGUEIRA, A. E.; AVANSI, W. & RIBEIRO, C. "Controlled synthesis of $BiVO_4$ photocatalysts: Evidence of the role of heterojunctions in their catalytic performance driven by visible-light." Appl. Catal. B Environ., **188**: 87, 2016.
175. CARVALHO, K. T. G.; NOGUEIRA, A. E.; LOPES, O. F.; BYZYNSKI, G. & RIBEIRO, C. "Enhanced photocatalytic activity of g-C_3N_4/Nb_2O_5 heterostructures on

degradation of organic pollutants under visible and ultraviolet irradiation." Appl. Catal. A Gen., 2016, Submitted.

176. XIAO, X.; XING, C.; HE, G.; ZUO, X.; NAN, J. & WANG, L. "Solvothermal synthesis of novel hierarchical $Bi_4O_5I_2$ nanoflakes with highly visible light photocatalytic performance for the degradation of 4-tert-butylphenol." Appl. Catal. B Environ., **148-149**: 154, 2014.

177. COOPER, J. K.; GUL, S.; TOMA, F. M.; CHEN, L.; GLANS, P.-A.; GUO, J.; AGER, J. W.; YANO, J. & SHARP, I. D. Electronic structure of monoclinic $BiVO_4$. Phys Chem Chem Phys., 14 (10): 4746, 2011.

178. LIANG, N.; WANG, M.; JIN, L.; HUANG, S.; CHEN, W.; XU, M.; HE, Q.; ZAI, J.; FANG, N. & QIAN, X. "Highly efficient $Ag_2O/Bi_2O_2CO_3$ p-n heterojunction photocatalysts with improved visible-light responsive activity." ACS Appl. Mater. Interfaces, 6 (14): 11698, 2014.

179. LIU, C. & CHAI, B. "Facile ion-exchange synthesis of $BiOI/Bi_2O_2CO_3$ heterostructure for efficient photocatalytic activity under visible light irradiation." J. Mater. Sci. Mater. Electron., 26 (4): 2296, 2015.

180. ZHU, G.; LIU, Y.; HOJAMBERDIEV, M.; HAN, J.; RODRÍGUEZ, J.; BILMES, S. A. & LIU, P. "Thermodecomposition synthesis of porous β-$Bi_2O_3/Bi_2O_2CO_3$ heterostructured photocatalysts with improved visible light photocatalytic activity." New J. Chem., 39 (12): 9557, 2015.

Appendix A

Supporting Information of Chapter I

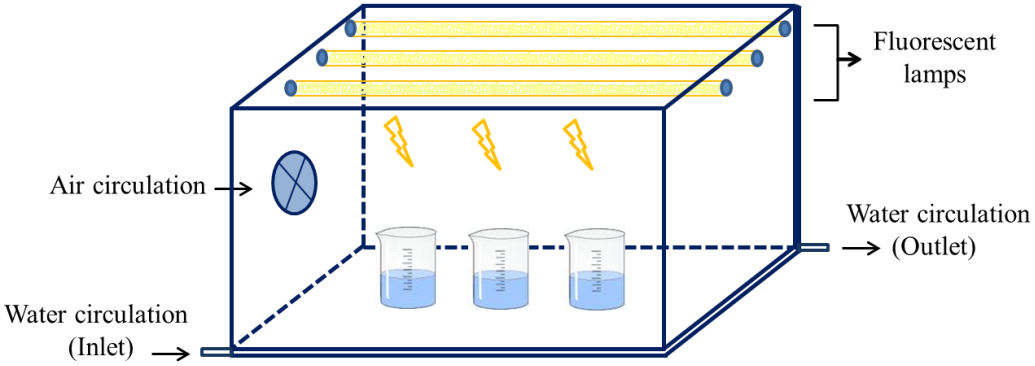

FIGURE A1. Schematic diagram of homemade photo-reactor used in photocatalytic experiments.

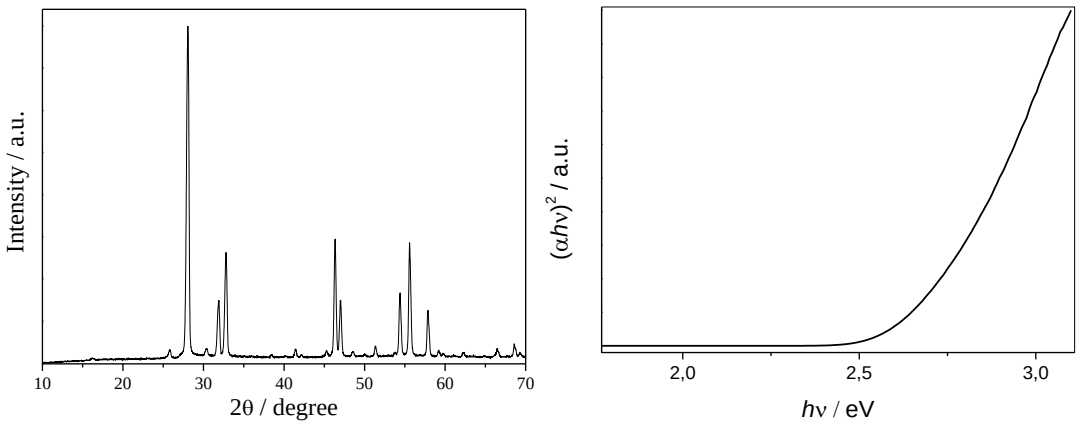

FIGURE A2. Typical XRD pattern of tetragonal Bi_2O_3 commercial nanopowder. Plots of $(\alpha h\upsilon)^2$ vs. photon energy ($h\upsilon$) obtained by Tauc equation from DRS spectra to tetragonal Bi_2O_3 commercial.

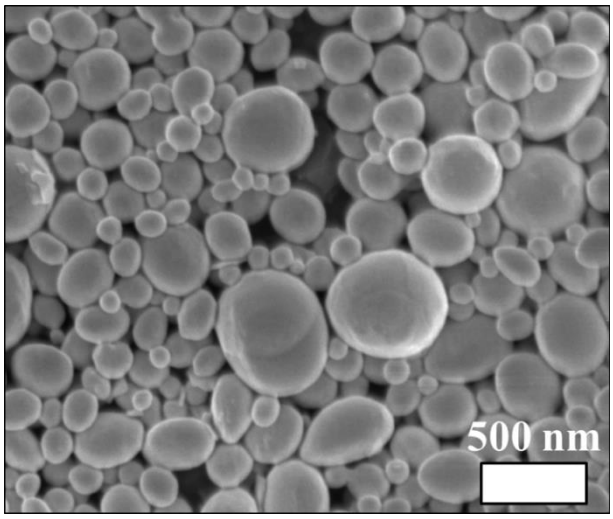

FIGURE A3. SEM images of tetragonal Bi_2O_3 commercial nanopowder.

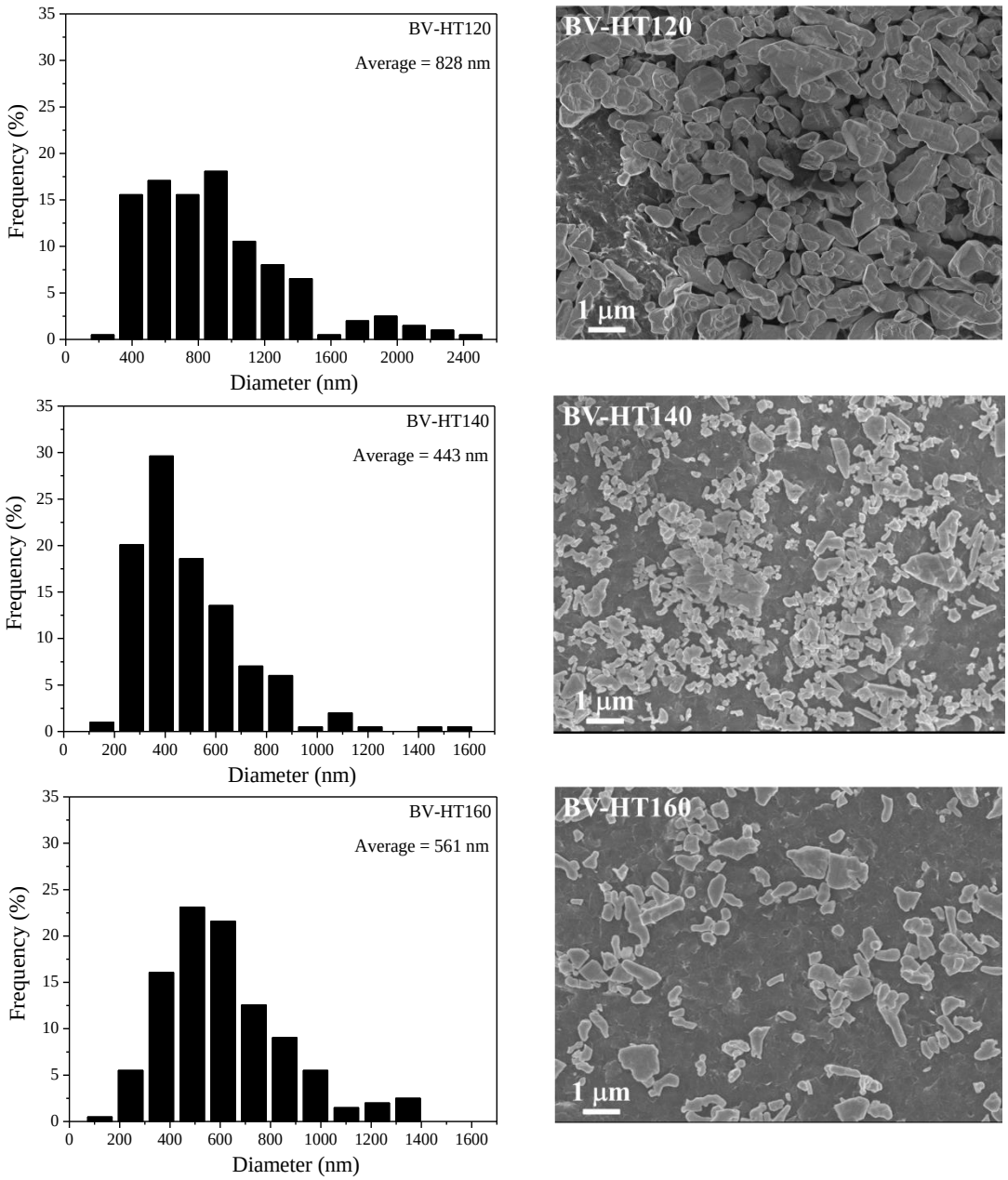

FIGURE A4. The size distribution of the particles and their respectively SEM images of as-synthesized samples of $BiVO_4$.

Appendix B

Supporting Information of Chapter II

TABLE B1 - First-order rate constants for the MB photodegradation tests performed under visible light irradiation.

Samples	***k* x 100 (h^{-1})**	**R^2**
V1-5	5.9 ±0.3	0.96
V1-10	5.6 ± 0.2	0.99
V2-5	6.6 ± 0.1	0.97
V2-10	7.4 ± 0.3	0.96

TABLE B2 - Binding energies of Bi $4f_{7/2}$, Bi $4f_{5/2}$,V $2p_{3/2}$, and V $2p_{1/2}$ for the V1-5-24 and V2-5-24 samples.

Samples	Bi $4f_{7/2}$	Bi $4f_{5/2}$	V $2p_{3/2}$	V $2p_{1/2}$	O 1s
V1-5-24	159.1	164.4	516.6	524.3	529.7 and 530.6[b]
V2-5-24	159.6 and 158.4[a]	165.0 and 163.8[a]	517.2 and 515.8[a]	524.5	530.3 and 532.0[b]

[a] Second satellite signal related to monoclinic $BiVO_4$phase present in the heterostructure.
[b] Signal might be relatedto hydroxyl oxygen and adsorbed oxygen at the surface of $BiVO_4$.

TABLE B3 - First-order rate constants for the MB photodegradation tests performed under visible light irradiation.

Samples	***k* x 100 (h^{-1})**	**R^2**
V1-5	5.9 ± 0.3	0.96
V2-5	6.6 ± 0.1	0.97
V1-5-24	6.1 ± 0.2	0.95
V2-5-24	27.4 ± 4.6	0.98

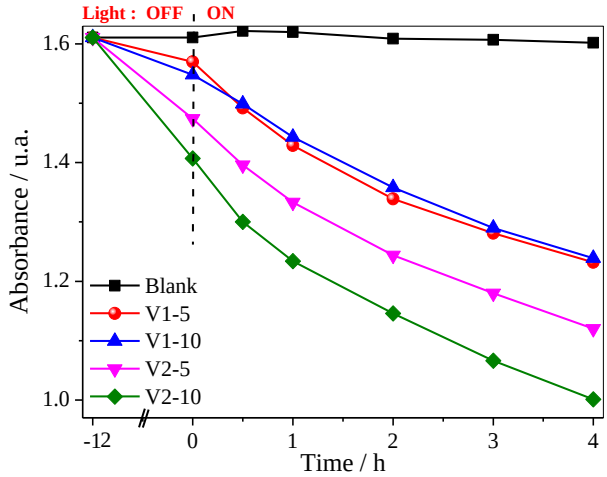

FIGURE B1. Photodegradation kinetics determination from the plots of MB dye concentration as a function of time before and after turn on the light (visible-light).

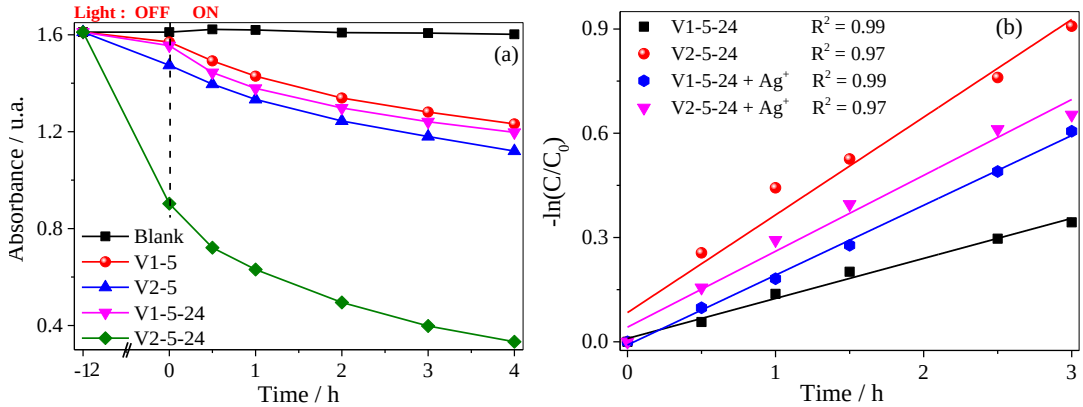

FIGURE B2. (a) Photodegradation kinetics determination from the plots of MB dye concentration as a function of time before and after turn on the light (visible-light). (b) Kinetic of pseudo first-orderfor MB dye photodegradation catalyzed by V1-5-24 and V2-5-24 with and without Ag^+ ($AgNO_3$, 20 mM).

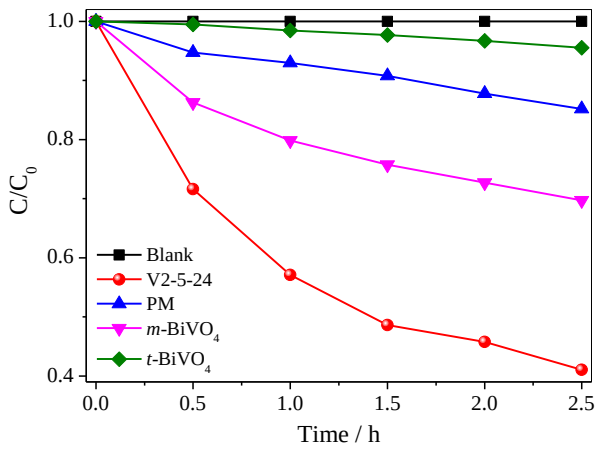

FIGURE B3. MB dye photodegradation curves comparison between heterostructure, physical mixture and isolated phases.

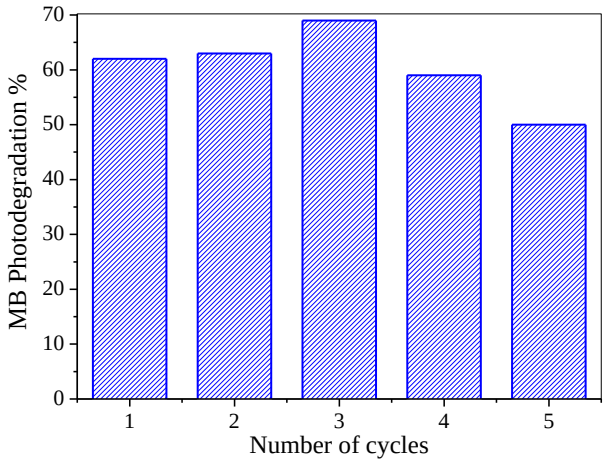

FIGURE B4. Cyclic stability of the *m*-$BiVO_4$/*t*-$BiVO_4$ heterostructure for the MB photodegradation.

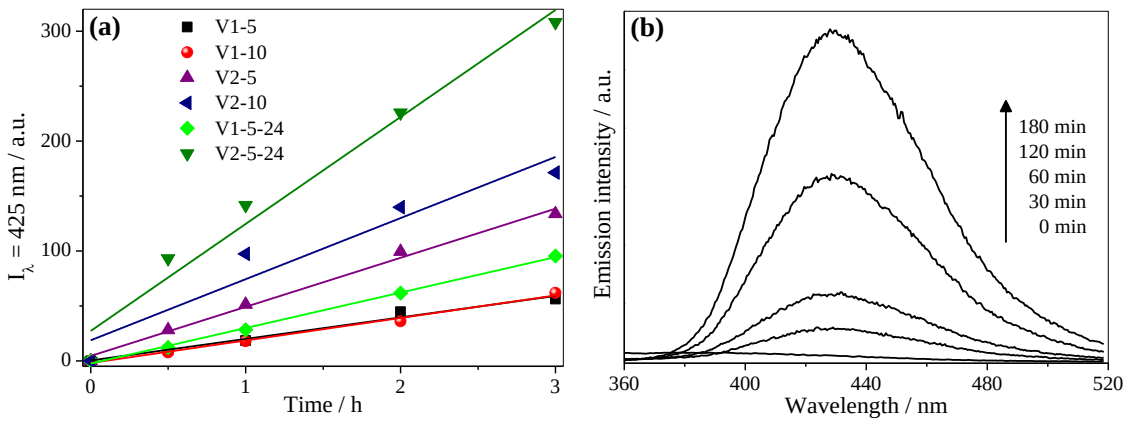

FIGURE B5. (a) Formation of hydroxyl radical by zero-order kinetics by the $BiVO_4$ as-synthesized samples. (b) The spectra profile of 2-hydroxyterephthalic acid formation using representative sample.

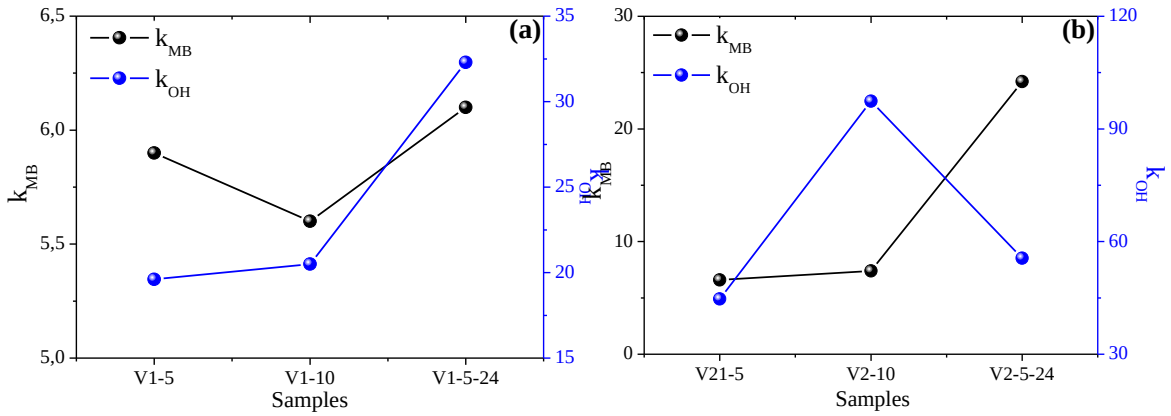

FIGURE B6. Rate constant for MB photodegradation and $^{\bullet}OH$ radical formation catalyzed by (a) V1 samples and (b) V2 samples.

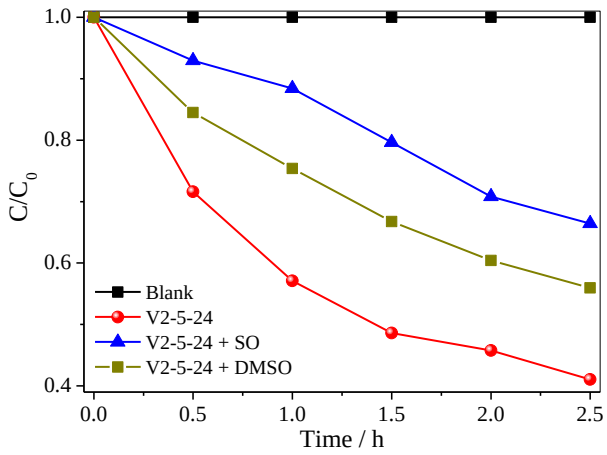

FIGURE B7. Photodegradation kinetic of MB dye (10 mg L^{-1}) catalyzed by V2-5-24 in the presence of sodium oxalate (h^+ scavenger) and DMSO ($^{\bullet}OH$ scavenger).

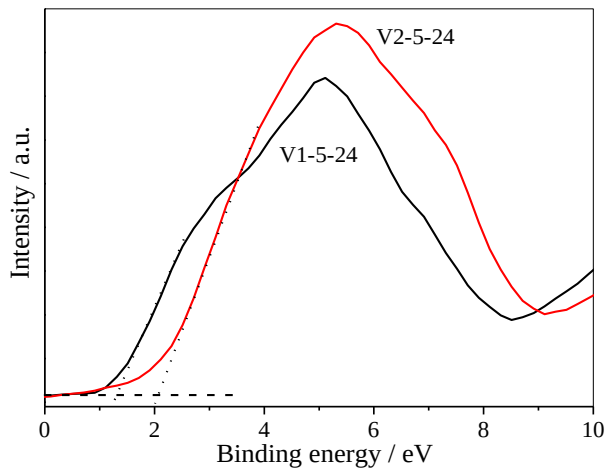

FIGURE B8. The VB-XPS spectra of V1-5-24 and V2-5-24 samples.

Appendix C

Supporting Information of Chapter III

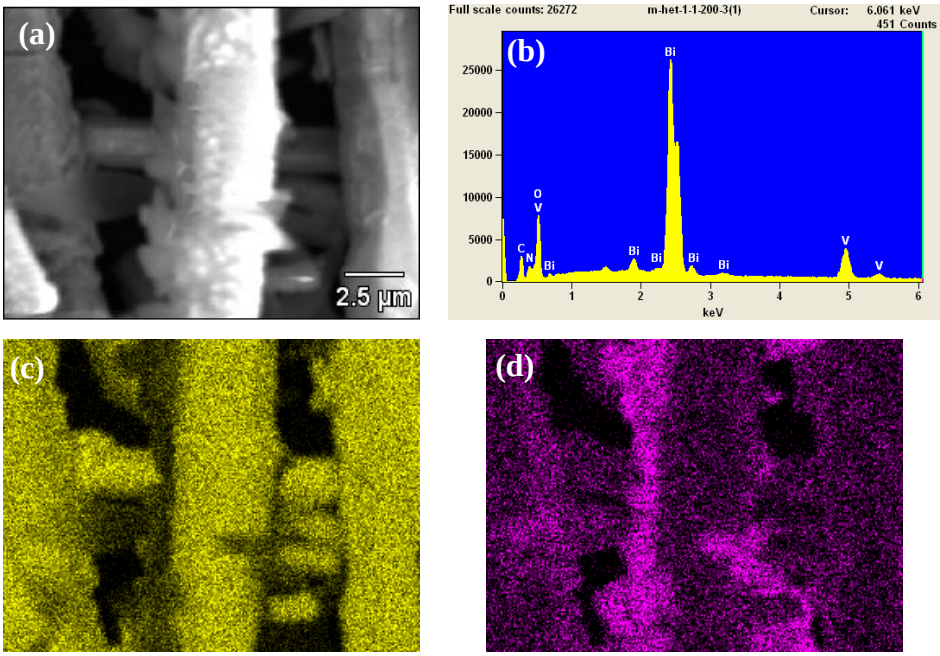

FIGURE C1 – (a) Representative SEM images of *m*-Het-1:1 200ºC samples, (b) EDX spectrum and elemental mapping for the (c) Bi and (d) V.

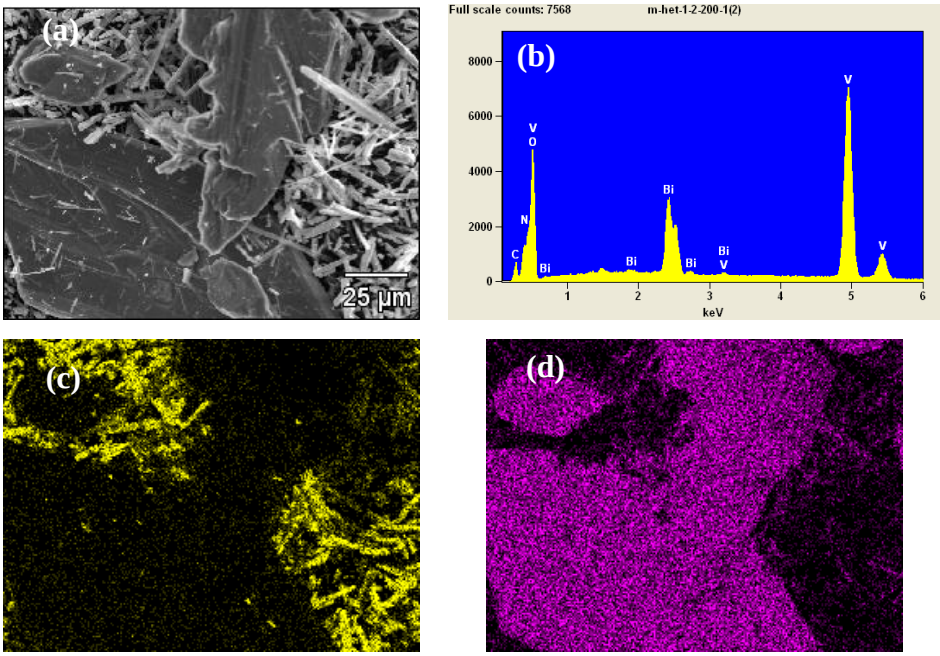

FIGURE C2 - (a) Representative SEM images of *m*-Het-1:2 200ºC samples, (b) EDX spectrum and elemental mapping for the (c) Bi and (d) V.

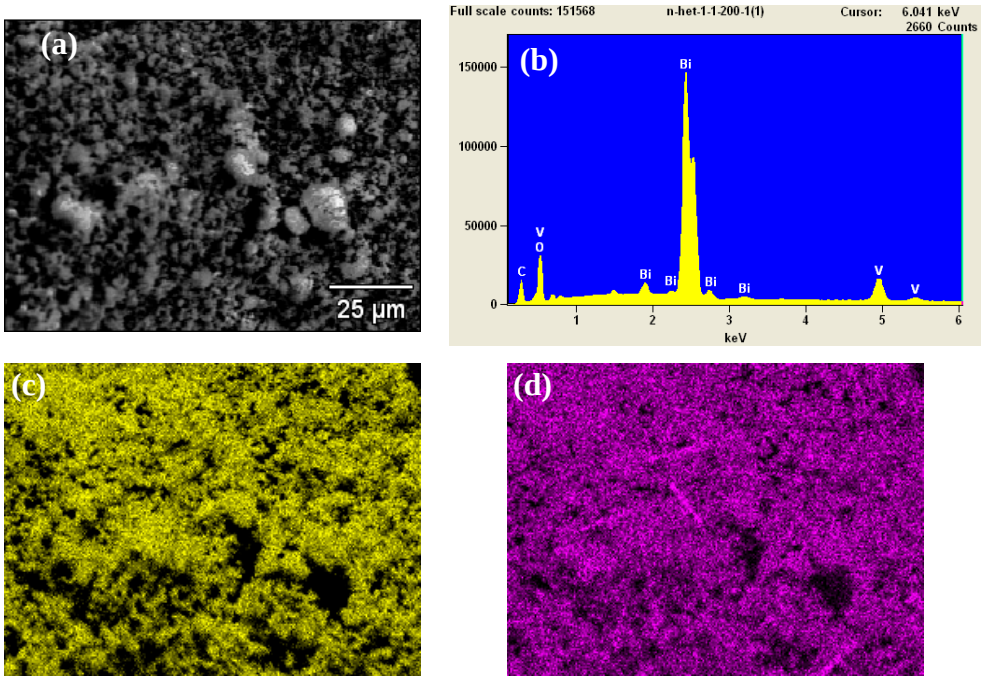

FIGURE C3 - (a) Representative SEM images of *n*-Het-1:1 200ºC samples, (b) EDX spectrum and elemental mapping for the (c) Bi and (d) V.

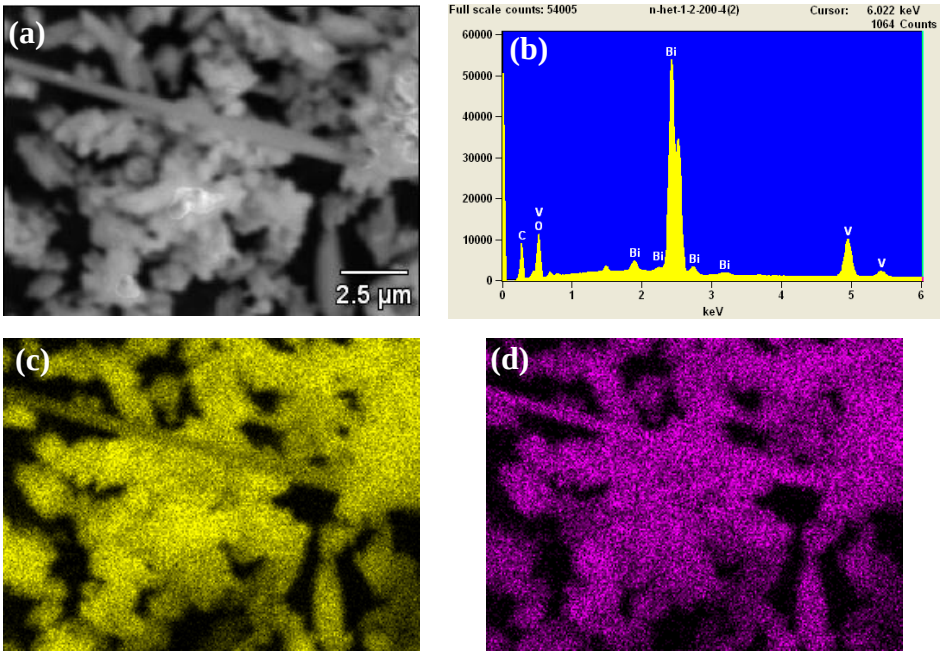

FIGURE C4 - (a) Representative SEM images of *n*-Het-1:2 200ºC samples, (b) EDX spectrum and elemental mapping for the (c) Bi and (d) V.